Wave Energy Converter Array Optimization in Irregular Waves

Shilu Liu
5526795

A thesis submitted for the degree of Master of Science

Delft University of Technology

Offshore & Dredging Engineering

Chairman & Daily Supervisor	George Lavidas
Daily Supervisor	Vaibhav Raghavan
Institution	Delft University of Technology
Place	Faculty of Civil Engineering and Geosciences
Project Duration	1 November, 2022 - 31 July, 2023

Contents

Abstract

Ocean waves being considered to have huge potential on providing renewable energy resources, allows for various water-based technology emerge as promising options for harnessing energy. While significant research and application of wave energy converters have been conducted in many seas, exploration on low-energy seas is still an ongoing endeavour. In this study, a point absorber array is being studied in the scenario of implementation at low-energy site within Caspian Sea.

The primary objective of this study is to give an optimal layout for a point absorber array with five devices. The research begins by evaluating many aspects of the computation tools namely NEMOH 3.0 and WEC-Sim. Subsequently, based on potential flow theory, hydrodynamic analysis is conducted by Boundary Element Method using a frequency domain model in NEMOH. Layouts with different spacing factors are examined to obtain the power matrices for each case. The q-factor, a measure that quantifies the WEC array's power absorption efficiency, and annual power production are readily calculated. Furthermore, given the annual energy production, an economic model is built to assess the CapEx, the Capital Expense, OpEx, the Operation Expense and LCOE, the Levelized Cost of Energy of the WEC array with different layout cases.

The final optimization phase finds a solution that simultaneously maximizes the q-factor and minimizes the LCOE by executing a multi-objective algorithm. Through this process, the best layout configuration for the five selected point absorbers in the Caspian Sea site is determined, taking into account both high energy output and economic viability. These findings expect to contribute to wave energy systems design by offering a reasonable optimization and economic evaluation methodology.

List of Figures

List of Tables

Nomenclature

Chapter 3

$\bar{P}$	Average Power Absorbed
$\bar{P}_w$	Power in Waves
$\bar{X}_j$	Acceleration of the System
$\Delta\omega$	Frequency Interval
γ	Peakness Factor
ν	Kinematic Viscosity of Water
ω	System Frequency
ω_p	Peak Wave Frequency
$\Phi^{(1)}$	Velocity Potential
$\Phi_0^{(1)}$	Incident Incoming Wave Potential
$\Phi_7^{(1)}$	Diffracted Wave Potential
$\Phi_D^{(1)}$	Diffraction Potential
$\Phi_I^{(1)}$	Incident Potential
$\Phi_j^{(1)}$	Potential Component from jth Degree of Freedom
$\Phi_R^{(1)}$	Radiation Potential
ρ	Water Density
$\vec{u}$	Velocity of Water Particle in x Direction
ξ_j	Amplitude of Motions
$\zeta(x,t)$	Free Surface Elevation
ζ_a	Amplitude of Free Surface Elevation
B^{PTO}	PTO Damping Coefficient
B_{add}	Additional Damping Matrix
B_{ij}	Damping Coefficient Matrix
$c(ij$	Restoring Coefficients
c	Wave Propagation Speed
C_g	Group Speed of Wave Propagation
$E_{kinetic}$	Kinetic Energy per Surface Area in Waves

$E_{potential}$ Potential Energy per Surface Area in Waves

E_{total} Total Energy per Surface Area in Waves

E_{total} Total Energy per Unit Surface Area

$F_{exc}^{(1)}$ Excitation Force

F_i^{ex} Excitation Force

F^{PTO} PTO Force

F_i^R Radiation Force

F_i Force Acting on the Structure

$G(x, x')$ Green Function

h Water Depth

k Wave Number

K_M Stiffness Matrix

L Wave Length

M_{ij}^a Added Mass Matrix

p Point Pressure

S_B Hull Surface

$S_\zeta(\omega_n)$ Energy Density at Frequency ω_n

T Wave Period

V_j Velocity of the System

Chapter 4

R Radius of Point Absorber

Chapter 5

d Spacing Factor

N Number of WECs in the WEC Array

P_0 Power Absorption for One WEC

P_{total} Total Power Absorption of WEC Array

Chapter 6

$C_{excable}$ Cost of Cable Lines Connected to Onshore Station per m

$C_{incable}$ Cost of Inter-array Cable Lines per m

$C_{installation}$ Cost of Hiring Installation Vessels for One Day

C_{PA} Cost of Point Absorber per kg

C_{repair} Cost of Yearly Repair

D Total Days of Installation

E_{annual} Annual Power Production

f Failure Rate of the Devices

$l_{excable}$ Length of Cable Lines Connected to Onshore Station per m

$l_{incable}$ Length of Inter-array Cable Lines per m

r Discount Rate

Y Total Years of Commissioning

Glossary

$IRF(t)$ Impulse Response Function. 24

BEM Boundary Element Method. 15, 20
BEMIO Boundary Element Method Input/Output. 41
BIE Boundary Integral Equation. 23

CapEx Capital Expenditure. 19
CFD Computational Fluid Dynamics. 14

DE Differential Evolution. 17

GA Genetic Algorithm. 16

LCOE Levelized Cost of Energy. 18

NSGA-II Multi-objective Evolutionary Algorithm. 18

OpEx Operating Expense. 19
OWC Oscillating Water Column. 12

PA Point ABsorber. 12, 13
PI Parabolic Intersection. 17
PTO Power Take-off. 14

QTF Quadratic Transfer Function. 20

RAO Response Amplitude Operator. 31
RCW Relative Capture Width. 17

SPH Smoothed Particle Hydrodynamics. 14

WECs Wave Energy Converters. 12

1

Introduction

1.1. Background

1.1.1. Wave energy

During the oil crisis of the 1970s[1], the decline in petroleum supply prompted major industries to seek alternative energy sources. Renewable energy options such as wind, solar, geothermal, hydroelectric, and biomass emerged are promising alternatives. Among these, wave energy stood out as an underdeveloped yet highly promising resource and gained attention for its immense potential to contribute to the global energy mix.

Wave energy is generated by the pressure differentiations created by the wind on the surface of the sea. The theoretical resource potential of ocean energy is incredibly vast, see in figure1.1 [2], to the extent that it has the capability to meet both current and projected global electricity demands for the foreseeable future. As a result, it is being recognized as a crucial component in the transition toward decarbonizing our energy systems. One of the key advantages of ocean energy is its predictability and consistent generation[3], making it an attractive option for integration with other renewable energy sources, like wind and solar power. By combining these renewable sources, there is potential for a more stable and reliable electrical grid. Ocean energy has the ability to contribute to grid stabilization and smoothing of power output, thus enhancing the overall reliability and efficiency of the energy system.

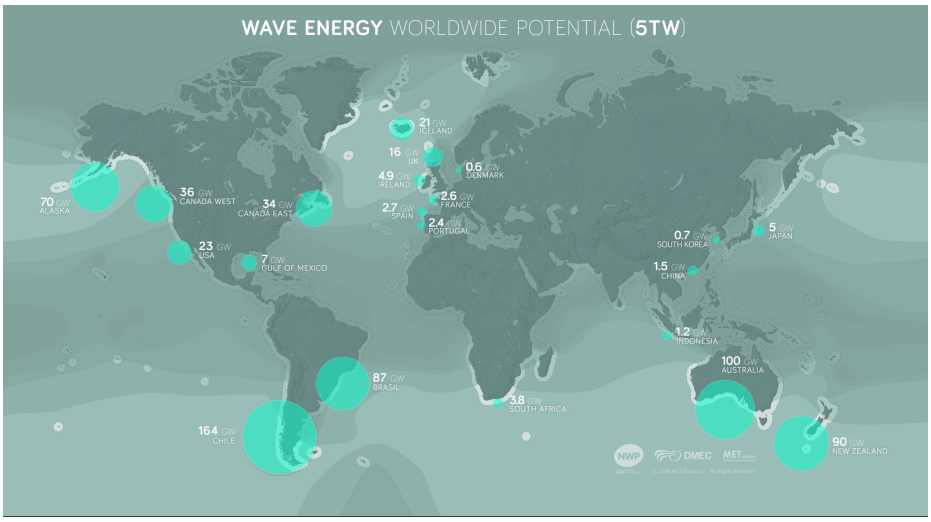

Figure 1.1: Worldwide wave energy potential

One significant advantage of wave energy is its potential for integration with solar and wind power plants, acting as a complementary resource[4]. For example, in[5], Kougias et al. studied the implementation of small hydropower plants as a complementary for solar power stations. This integration offers the opportunity to smooth out power output fluctuations and enhance the overall reliability of the energy system. Additionally, wave energy technologies can have reduced environmental and visual impacts compared to wind turbines[6], making them a more appealing option in certain locations.

Overall, wave energy holds great promise as a renewable energy source, and its utilization has the potential to contribute to meeting energy demands while reducing carbon emissions and minimizing environmental impacts.

1.1.2. Wave energy converters

Wave energy converters (WECs) are devices used to convert electricity from captured wave energy. Apart from acting as renewable energy generators, WECs exhibit versatility by serving other functions. For example, WECs can provide coastal protection against wave-induced erosion and the creation of a calmer water sheet with reduced wave motion[7]. Additionally, unlike some large floating devices that cause a negative impact on the landscape, the small size of WECs usually gives minimal visual impact, which will minimize the potential negative effects on tourism and preserve the aesthetic appeal of coastal regions.

Although the energy resource that exists in ocean waves is more energy-dense than other types of resources, some aspects of relevant technology are still considered to be immature, with improvable efficiencies. For example, bringing up the efficiency and developing more commercially attractive WECs remain worth studying nowadays. WECs are commonly classified into the following categories: Attenuators, overtopping converter devices, oscillating water columns (OWC), and point absorbers (PA).

An attenuator is a long floating device typically consisting of multiple floating bodies connected by hinged joints aligned with the direction of wave propagation. By utilizing the hinged joints, the attenuator is able to flex and respond to the incoming waves, which makes it capture wave energy by constraining the movements along its length. This device is designed to dampen the wave motion and convert the kinetic energy in waves' oscillations into usable power.

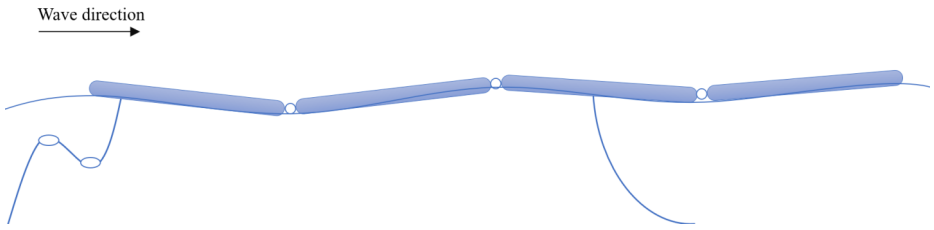

Figure 1.2: Attenuator device

An overtopping device operates in a manner similar to a hydroelectric dam, utilizing the energy of ocean waves to generate power. This type of device consists of a floating arm that directs waves toward a sloping surface, where the waves overtop into a reservoir. The difference in water elevation between the reservoir and the mean sea level creates a driving force that is used to power low-head hydro turbines.

The overtopping device can be installed near the shoreline, either in front of or as part of caisson breakwaters. These breakwaters act as barriers, collecting and channelling the ocean waves toward the reservoirs. The reservoirs can be strategically placed above each other to maximize hydraulic efficiency, allowing for effective energy capture from the waves.

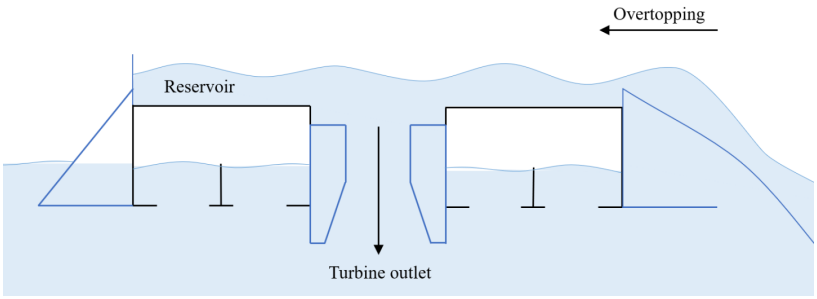

Figure 1.3: Example for overtopping converter, the "Dragon"

An oscillating water column is a wave energy converter that utilizes a collector chamber to extract power from ocean waves and transfer it to trapped air within the chamber. The OWC system consists of a hollow column, typically situated above the water level, which captures and contains air. As waves pass by, the rising and falling motion of the water column causes the air within the chamber to undergo alternating pressurization and rarefaction. When the water column rises, it compresses the air, leading to an increase in pressure. Conversely, as the water column falls, the air inside the chamber expands, resulting in a decrease in pressure. This cyclical variation in air pressure is used to drive a power take-off system that converts the power into another usable form of energy.

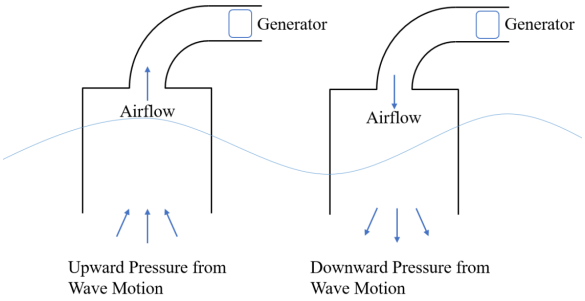

Figure 1.4: Oscillating water column device

Point absorbers(PA) are floating structures designed to absorb energy from waves coming from all directions. Basically, the principle of a point absorber is to convert energy from the relative motion between the floating device and the seabed. They are typically buoy-shaped and have a relatively simple design and relatively small size, allowing for easy installation and operation. Due to their compact size, point absorbers can be deployed in various locations, including near-shore or offshore environments. They are also cost-effective due to being less prone to malfunction since their operational principles are relatively straightforward.

Point absorber devices take various geometric forms, including spherical, ellipsoidal, cylindrical, or conical shapes. Various types of point absorbers have been studied in relation to different wave characteristics. For instance, conical point absorbers have a range of parameters that can influence their energy absorption efficiencies, such as the conical angle, diameter, and draft ratio[8]. Study[8] has also revealed a correlation between these parameters and the maximum absorbed power. Among the various types of PAs, spherical-shaped devices with a constant diameter have been identified as the most efficient in terms of energy conversion.

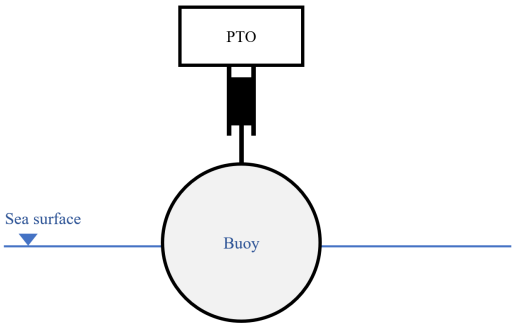

Figure 1.5: Point absorber

The power take-off (PTO) system of a wave energy converter is a crucial component and a vital mechanism designed to absorb energy from the primary converter and efficiently transfer it into usable electricity. The PTO system plays a critical role in WECs, not only facilitating the direct and efficient transfer of energy but also significantly impacting the overall mass and dynamics of the WEC.

In the case of an OWC wave energy converter, the power take-off PTO system primarily consists of an air turbine. For other types of WECs, the PTO system may involve a combination of hydraulic components and an electric generator.

1.2. Literature review

This thesis adopts a numerical method to address the hydrodynamic analysis, primarily motivated by the complexity of the three-dimensional fluid environment, which involves the presence of complex differential equations. By employing a numerical approach, significantly faster computations can be achieved compared to using analytical methods. Following this, an optimization process will be conducted to enhance the layout of the WEC array. Given the background of this topic, a comprehensive literature review on diverse numerical methods for resolving hydrodynamic problems and various optimization strategies has been conducted. The aim is to identify an appropriate approach to employ in this research.

1.2.1. Review on numerical modelling approaches

There are different ways to model WECs using computational modelling methods, which can be divided into frequency domain methods and time domain methods.

OpenFOAM, SPH, and WEC-Sim are widely recognized time domain methods that are commonly employed in hydrodynamic calculations.

OpenFOAM is a CFD (Computational fluid dynamics) based open-source solver. CFD is one kind of fluid mechanics that solves problems with fluid by numerical analysis. The basis is performing a spatial discretization of the Navier-Stokes equations. The CFD models are employed to simulate the dynamic interaction of liquids and gases, where surface conditions are defined as boundary conditions. Additionally, CFD simulations can be a viable alternative to costly experiments, provided the results are validated. Research on hydrodynamic coefficients of a two-body point absorber by utilizing OpenFOAM was reported by Amir et al. 2022 [9]. The study compared the hydrodynamic coefficients and the power absorption of WEC obtained from numerical and experimental methods, which concluded that the coefficients obtained from OpenFOAM are much larger because of including the viscous damping that occurs due to the resistance to motion caused by the fluid viscosity within the PTO.

Smoothed Particle Hydrodynamics (SPH) is a Lagrangian, mesh-free computational method that is particularly advantageous when conventional mesh-based approaches encounter challenges in solving complicated geometries or scenarios. Soleimani et al. performed simulation based on two kinds of

SPH (SPH-W and SPH-C) methods on a point absorber to evaluate the motion response in 2022[10]. In this research, the motion decay of the WEC in calm water was modelled to obtain the added mass and damping coefficients to evaluate the hydrodynamic performance of the WEC. Francesco et al. [11] performed a study on wave forces on horizontal circular cylinders and compared results from SPH simulation and experiments in 2017, which were found to have a good agreement. The study aimed at presenting the correlation between the coefficients and geometrical dimensions by SPH simulation in a solitary wave field. In study of Yeylaghi et al.[12], hydrodynamic forces were computed by SPH method and multiple advantages emerged, such as the capability of dealing with extreme wave conditions.

WEC-Sim is an open-source numerical solver for WEC devices based on time-domain method, simulating the devices by using the boundary element data from other software. Ruehl et al. [13] studies how to calculate Froud-Krylov forces of a heaving-based two-body point absorber in WEC-Sim by using linear hydrodynamic coefficients drawn from WAMIT in 2014. Lawson et al. [14] applied WEC-Sim modelling on different WEC designs and validated the model by comparing the response to experimental studies.

NEMOH, HAMS, WAMIT, and Capytaine are utilized to perform hydrodynamic calculations by solving the corresponding models in the frequency domain.

NEMOH,and WAMIT are both commonly used frequency-domain based BEM(Boundary Element Method) solvers for excitation force, added mass and radiation damping estimation from the radiation problem, with HAMS and Capytaine emerging as open source alternatives. Penalba et al. [15] discussed the ability of NEMOH solver and validated NEMOH code in MATLAB by investigating different types of WECs. In this study, added-mass, radiation damping and excitation force coefficients were calculated through NEMOH simulation, which showed good agreement with WAMIT. Moreover, the MATLAB wrapper ensured NEMOH a more user-friendly pre-processor to generate meshes.

Capytaine, another open-source frequency-domain-based BEM solver, adopts codes in Python rewritten from NEMOH. Austin Berrier[16] utilized Capytaine software as BEM solver to find hydrodynamic coefficients in an optimization of WEC design. HAMS is an open-source software proposed by Liu et al.[17] in 2019. The outstanding feature is that the software uses the least squares method and partially extends the boundary integral equation so that to remove the irregular frequencies caused by sloshing. W. Sheng et al. [18] studied hydrodynamic performances on three types of floating structures, including a truncated cylinder, a truncated cylinder with a heave plate and a point absorber in 2021. The research aimed at testing the potential of HAMS, another open source solver based on potential flow theory, and NEMOH codes by implementing the models and comparing the coefficients and responses to WAMIT results. The study found that NEMOH had limitations in predicting the coefficients for structures with overlapped and thin panels, while HAMS handled the problems differently, which results in good accuracy. However, HAMS is limited at dealing with multi-bodies targets. NEMOH, on the other hand is available in modelling multi-body problems.

Features of the investigated methods are summarized in table1.1.

Table 1.1: Summary of WEC computational modelling tools and methods

	Limitations	Advantages	Method
OpenFOAM	More computational time, especially with high mesh resolution[19]	• Open source • Validated in studies	Time domain
SPH	Inaccuracy of handling problem with shocks in wave[20]	• Good at modelling free surfaces • Good at dealing with moving boundaries • Suitable for extreme wave conditions	Time domain
WEC-Sim	More computational time when involving non-linearities	• Open source • Validated in studies[13] • Capable for multi-body interaction	Time domain
NEMOH	• One-core simulation • fails in OWC[18]	• Open-source • Capable for multi-body interaction • Validated in studies[21]	BEM based on Frequency domain
HAMS	Cannot deal with multi-body interaction	• Open source • Fast running speed by parallelization	BEM based on Frequency domain
WAMIT	Only available for commercial purpose	Fast speed due to parallelization[22]	BEM based on Frequency domain
Capytaine	Requires more maintenance[23]	• Open source • Able to use 3rd party meshed models • Fast running speed by parallelization	BEM based on Frequency domain

1.2.2. Review on optimization methods

Various methods have been applied to deal with WEC array optimization problems in studies. So far, three categories of methods are mainly used in literature, which are Parabolic Intersection, meta-heuristic methods, for example, Genetic Algorithm, mathematical methods, for example, and machine learning methods.

Genetic Algorithm (GA) has been the most commonly used meta-heuristic method in WECs array optimization problems. Marianna Giassi et al. developed an economical model of a point-absorber wave farm and found the optimal array layout in terms of LCOE values in 2020. The optimization was proceeded by GA evaluation, coupled with economical model[24].

Giassi et al.[25] also optimized wave energy array by two versions of GA code, using discrete and continuous variables respectively, with different WEC spatial coordinates. This study also aimed

to test the reliability of the newly developed GA codes in solving WEC layout array optimizations. The combination of code A and B can give a fast convergence and capability in finding the best separate distance in optimizations. Differential evolution (DE) algorithm is another preferred meta-heuristic method in relevant research so far. Hong-Wei Fang et al. (2018)[26] made an amelioration to traditional DE methods on WEC array optimization problem by introducing an adaptive mutation operator to the model, which aims to improve the convergence precision and speed of DE method. By comparing the yielded results, the improved method was confirmed to be superior to the traditional DE method. Zhenqing Liu et al. [27] proposed an analytical wave model and energy output model, which were optimized by DE method to reach a layout with maximum total energy output in 2021.

Junhua Wu et al.[28] performed a simple self-developed evolutionary algorithm to get the optimal layout of a submerged WEC array in 2016. This method generates 100 random layouts and evolves the layout with single frequency approximation, which reduces computational time effectively. A non-dimensional index, relative capture width (RCW) was chosen as the optimization objective in this study. M Mohsen Moarefdoost et al. presented wave farm layout optimization study to maximize wave farm performance and proposed an iterative heuristic algorithm (Two-phase heuristic) to obtain an optimal configuration in 2017[29]. Child et al. applied two different heuristic searching methods, Parabolic Intersection (PI) and Genetic Algorithm to investigate the optimal layout of a wave farm. By comparing the two methods, the researchers concluded that GA method tends to give more optimised results considering total energy output, while PI method has a faster computing speed and a more comprehensible procedure[30].

Dripta Sarkar used active learning, a kind of machine learning approach, to predict the optimal layout of a 40-WEC array[31]. Machine learning algorithm is a preferable way to deal with arrays with a large number of WECs. Additionally, machine learning method was found to be competitive in its scalability, which means when facing a larger problem, it is not required to modify the existing formulation once it is trained. Also, the prediction of the active learning method shows accuracy even with a limited number of data in complicated problems[32].

1.2.3. Review on wave energy potential in Caspian Sea

In this thesis research, the Caspian Sea has been selected as the site for implementing the WEC array. A review of the energy potential within this particular sea region helps to assess its suitability for WECs as a low-energy sea area[33]. The finding helps to decide a more appropriate WEC category.

The Caspian Sea is known as the largest lake as well as a closed basin located in the northern hemisphere. The sea area spans latitudes 47.130° N to 36.340° N and longitudes 46.430° E to 54.510° E with a 7000 km coastline, sharing borders with Iran to the south, Turkmenistan and Kazakhstan to the east and northeast, Russia to the northwest and west, and Azerbaijan to the west geographically[34]. Despite being a closed lake, the Caspian Sea is known to experience frequent storms[35], which leads to a relatively promising energy yield potential in comparison with other low-energy seas. Study[36] by Rakisheva et al. in 2019 shows the Caspian Sea exhibits seasonal variability, resulting in variations in the energy regime across different regions. This means that certain WEC that may be suitable candidates for one region may not be optimal choices for other regions within the Caspian Sea[37]. And study by Rezvan et al. revealed that the neighbourhood site of two cities: Noshahr and Babolsar are the most suitable sites for the installation of WECs[34] based on the analysed data that indicates a small variation on average annual energy. A thorough evaluation of different existing WEC technologies' feasibility in the Caspian Sea was conducted by Alamian et al. in 2014[38]. Point absorber was found to be the most promising WEC technology specific for the Caspian Sea environment.

Based on the findings from the literature review, it is reasonable to select Babolsar as the implementing site for the studied WEC array.

1.2.4. Review on WEC application in low energy sea and the choices on point absorber layout

Existing investigations and studies justify the selection of point absorber devices as the WEC to be introduced in Babolsar site[38]. Currently, it is notable that the technology is focusing on developing

WECs for high-energy ocean waves, resulting in large-sized WECs capable of operating even in extreme wave conditions. While the potential for harnessing high power levels in dense energy areas seems promising, the occurrence of severe storms lowers the normal power generation of these large WECs. As a result, their potential is not fully utilized, and the substantial maintenance costs due to extreme weather conditions compromise their commercial attractiveness.

Conversely, in low-energy seas, the demand for survivability is not a major concern, as extreme events occur infrequently. Consequently, WECs deployed in low-energy seas can have a longer commissioning period, leading to a significant reduction in costs[39]. Also, in these less energetic environments, the existing large devices may not capture the waves readily or be easily driven[40]. These all suggest that the optimal size of WECs should be reduced to match the power level of the waves.

In this study, the layout of 5 WECs is going be optimized with different spacing, therefore, a relevant topic is studied. Regarding the literature on layout optimization for 5 WEC point absorbers, Child et al. conducted a study that presented two converged solutions[30] in 2010: The first solution involved arranging three WECs in a single line, while the remaining two WECs were placed in another line. The second solution proposed a scattered layout of the five WECs. McGuinness et al.[41] optimized the layout of 5 point absorbers placed in a straight line with different spacing. Giassi et al. found the optimal layout for a wave energy park with the spacing between the WECs being 10m, is when the WECs are aligned towards the incident wave's incoming direction.[25]

1.3. Survey on research gaps

As in the previous section, an overview of research regarding WEC and WEC array optimization has been presented. Although so far, numerous methods have been adopted to solve optimization problems, there are clear research gaps in existing studies, which are highlighted as follows:

Smaller WECs in low-energy sea

Current studies tend to design WEC arrays that are applied to high-energy seas, which requires the devices to be large-sized to capture and withstand extreme weather. However, it is noticed that insufficient literature has focused on the potential of wave energy in low-energy seas[33], where the annual mean wave power ranges from 2 to 14 kW. Therefore, the research gap exists in designing an optimal WEC array in low-energy sea environments. In this research, a WEC array in a low-energy sea, the Caspian Sea is studied, to develop a practicable and commercially attractive array for the promising site.

Combination of Energy Conversion Goal and Economic Goal

Most of the previous studies intended to get an optimal array layout by evaluating q-factor, the factor that is commonly used to measure the power extraction capability of a WEC array, or the total energy output. Also, some studies focus on optimizing LCOE of the WEC system. However, few studies have investigated on how to achieve an optimum between q-factor and economic objectives. In order to improve this, this master research will adopt a multi-objective optimization methodology, NSGA-II(Multi-objective genetic algorithm), to set up multiple objective functions involving both q-factor and LCOE. This algorithm allows for solving problem with multiple objectives very fast based on an evolutionary computation. The evaluation will be finalized in MATLAB by finding Pareto-front sets, which is a front that consists of the points implying a set of solutions in a multi-objective problem, for solutions to each objective function.

1.4. Research objectives

1.4.1. Objective 1: Verifying hydrodynamic analysis in NEMOH associated with WEC-Sim on a test model, and finalized the WEC model used in optimization

The initial step of this study should be performing a verification of the tools to be used in the following hydrodynamic calculations. Therefore, a test model will be established to assess the following aspects:

the computational capabilities NEMOH 3.0, which was updated in December, and NEMOH 2.8; the computational outcomes obtained through WEC-Sim simulation; and the interdependence and coherence between NEMOH and WEC-Sim.

1.4.2. Objective 2: Performing hydrodynamic analysis to find the wave power at the selected site

Since one of the optimization objectives, q-factor has the total wave power absorption by isolated WECs as an essential component, the first stage work will be computation of the power absorption by the WECs acting in isolation. This will be done by performing hydrodynamic analysis on the WECs, given estimated constant PTO coefficients and wave spectrum defined from real sea states. The analysis will be done by using WEC-Sim in combination with NEMOH as preferable hydrodynamic analysis tools due to their affordable running cost (open source), sufficient documentation, and capability of dealing with multi-body interaction. The hydrodynamic coefficients will be estimated by BEM modeling in NEMOH, which will be used in WEC-Sim modelling to obtain the power matrix subsequently.

1.4.3. Objective 3: Developing mathematical formulations for the optimization problems and form the objective functions

Objective functions about both q-factor, which is power production related, and LCOE, which is economical objective related, will be formulated at this stage. q-factor, the relation between total wave energy absorption by the wave farm and the wave energy absorption by N isolated WECs, is written as a function of the position of WECs in the wave farm, dimensions of WECs, and multiple irregular wave condition parameters. LCOE is written as a function of CapEx, OpEx, discount rate and operation years of the wave farm.

1.4.4. Objective 4: Optimization considering power production and economical goal by NSGA-II (Multi-objective evolutionary algorithm)

The final objective of this research is to find the optimized solution to the WEC array layout problem and achieve an optimal balance between power production and costs. After setting up two objective functions in the previous stage, the optimization will be finalized by NSGA-II in MATLAB by searching for the Pareto-front sets.

2

Theoretical background

Boundary element method (BEM) is one kind of numerical computational method that can be employed for various engineering problems where Green's functions can be found. Most BEM codes are based on Green's function approach, which utilizes free surface Green's functions for computation. The basis is the computation of the Green's function, by looking up for approximations to the surface of Green functions. Different from commercial software like WAMIT, which uses Newman's approximation to solve the Green function, NEMOH codes give the prediction for free surface by utilizing an interpolation from 5^{th} order Lagrange formula. This chapter presents the theoretical background of the numerical methodology used in the research.

NEMOH has two modules that deal with linear diffraction and radiation problems and Quadratic Transfer Functions (QTF) respectively. The frequency domain-based BEM solver NEMOH1 modules are used to perform hydrodynamic analysis.

The subsequent step involves utilizing the hydrodynamic data obtained from NEMOH, along with the boundary element method data, as inputs for WEC-Sim. By integrating the data, a time-domain simulation will be performed by solving some essential governing equations. This simulation enables the evaluation of the wave energy converter's performance under real-world operating conditions, taking into account the dynamic interactions between the device and the waves.

The fundamental principles and concepts that form the basis of the numerical simulations will be presented in this chapter.

2.1. Navier-Stokes equation

The Navier-Stokes equations are widely accepted as the governing equations for describing the dynamics of fluid motion. In the case of an incompressible fluid, such as water, and under the assumption of the continuum hypothesis, the Navier-Stokes equations consist of the following equations:

- Conservation of Mass

$$\vec{\nabla} \cdot \vec{u} = 0 \tag{2.1}$$

This equation states that in case of an incompressible fluid, the mass and volume of fluid stay constant.

- Conservation of momentum

where $\vec{u}$ is the velocity of water particles in x direction.

$$\frac{\partial \vec{u}}{\partial t} + (\vec{u} \cdot \vec{\nabla})\vec{u} = -\frac{1}{\rho}\vec{\nabla}p + \nu\vec{\nabla}^2\vec{u} + F_b \tag{2.2}$$

where $\vec{u}$ is the velocity of water particles in x direction, p is the point pressure, ν is the kinematic viscosity of water. This equation is equivalent to Newton's Second Law, and the terms represent the

acceleration of water particles, the normal force acting on the fluid surface, the pressure acting on the fluid, the shear force on the fluid, and the external forces acting on the fluid respectively.

Here, the fluid is assumed to be ideal, neglecting the diffusive component in the Navier-Stokes equations, which is applicable for sinusoidal waveforms. This assumption is justified by the relatively small kinematic viscosity of water within the context of wwave energy. Additionally, it is essential to assume that the wave height H is much smaller than the wavelength L and the water depth$h$, s necessary to ensure the validity of linearizing the Bernoulli equation and to consider the gradients of the diffusive part of the Navier-Stokes Equation as small enough to be neglected. Consequently, the water particles' motions are considered to be irrotational, enabling the introduction of a velocity potential, as given by:

$$\frac{\partial \Phi}{\partial x} = u, \quad \frac{\partial \Phi}{\partial y} = v, \quad \frac{\partial \Phi}{\partial z} = w \tag{2.3}$$

where Φ is the velocity potential, the sum of the incident potential, the diffraction potential, and the radiation potential. By implementing the potential theory, the equation of wave can be written as:

$$\zeta(x,t) = \zeta_a \cdot \cos(kx - \omega t) \tag{2.4}$$

where $\zeta(x,t)$ is the free surface elevation with respect to $z = 0$; k is the wave number. In the case of a 2-D flow (an example of a flow in Cartesian coordinate is given in figure2.1, the analytical formulas can be given after substituting equation 2.3 into the Navier-Stokes equation and applying appropriate boundary conditions:

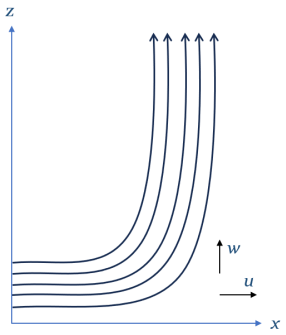

Figure 2.1: An example of flow in Cartesian coordinate

$$\begin{aligned} u(x,z,t) &= \frac{\partial \Phi^{(1)}}{\partial x} = \omega \zeta_a \frac{\cosh k(h+z)}{\sinh kh} \cos(kx - \omega t) \\ w(x,z,t) &= \frac{\partial \Phi^{(1)}}{\partial z} = \omega \zeta_a \frac{\sinh k(h+z)}{\sinh kh} \sin(kx - \omega t) \\ p(x,z,t) &= -\rho g z + \rho g \zeta_a \frac{\cosh k(h+z)}{\cosh kh} \cos(kx - \omega t) \end{aligned} \tag{2.5}$$

2.2. Potential flow theory

The potential flow theory follows assumptions that characterize the flow to be irrotational, inviscid, and incompressible. The irrotationality has its significance in the regions that is vorticity-free. Though NEMOH modeling seeks solutions in near field approach, the effects of flow regions such as boundary layers are not suitable for potential flow theory and are neglected. The potential function in the time domain can be written as:

$$\Phi(x,t) = Re\left\{\Phi^{(1)}(x) e^{-i\omega t}\right\}. \tag{2.6}$$

where Φ is the velocity potential; $\Phi^{(1)}$ is the complex amplitude of the total potential; (x) is a space-dependent vector; ω is system frequency.

Because the flow is irrotational, inciscid and incompressible, it follows the Laplace's equation:

$$\nabla^2\Phi^{(1)} = 0; \nabla^2\Phi^{(1)} = 0; \tag{2.7}$$

In addition, the equation set of potential functions can be decomposed to governing equations satisfying impermeable conditions on the sea floor and hull, diffraction, and radiation conditions on the hull surface, which form the key boundary conditions required to solve the Laplace equation.

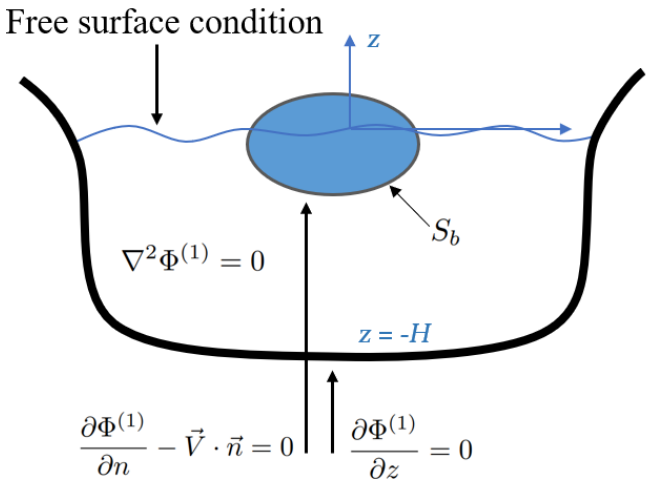

Figure 2.2: Deriving of potential flow theory

- Impermeable condition on the hull

$$\frac{\partial\Phi^{(1)}}{\partial n} - \vec{V}\cdot\vec{n} = 0, \text{ on the hull surface} \tag{2.8}$$

- Impermeable condition at the seabed

$$\frac{\partial\Phi^{(1)}}{\partial z} = 0, \text{ at the seabed, } z = -H \tag{2.9}$$

- Free surface boundary condition

$$\frac{\partial\Phi^{(1)}}{\partial z} - k\Phi^{(1)} = 0, \text{ at } z = 0 \tag{2.10}$$

- The total potential can be decomposed into two parts, namely the wave radiation potential function, $\Phi_R^{(1)}$, and the wave diffraction, $\Phi_D^{(1)}$.

$$\Phi^{(1)} = \Phi_R^{(1)} + \Phi_D^{(1)} \tag{2.11}$$

- The radiation potential is generated from the first-order motions of the body in a fluid. For rigid bodies which have 6 degrees of freedom motions, the radiation potential consists of 6 modes of motion during wave structure interactions, which corresponds to surge, sway, heave, roll, pitch and yaw. Therefore, the radiation potential can be written as the summation of 6 components with respect to each degree of freedom.

$$\Phi_R^{(1)} = i\omega \sum_{j=1}^{6} \xi_j \Phi_j^{(1)}, j = 1, 2, ..., 6 \tag{2.12}$$

where ξ_j is the amplitude of motions, $\Phi_j^{(1)}$ is potential components from one degree of freedom, or one unit of amplitude motion in the jth degree of freedom.

By superposing the radiation potential equation to the surface boundary condition, the surface boundary condition can be simplified as:

$$\frac{\partial \Phi_j^{(1)}}{\partial n} = n_j, \text{ on the body surface } S_b \tag{2.13}$$

- The diffraction potential is generated by the incoming wave's diffracting on the existing structure, while considering the structure to be stationary. Thus the total diffraction potential can be written as:

$$\Phi_D^{(1)} = \Phi_0^{(1)} + \Phi_7^{(1)} \tag{2.14}$$

where $\Phi_0^{(1)}$ is the incident potential of incoming wave, $\Phi_7^{(1)}$ is the potential function of scattered wave.

The incident potential can be written as:

$$\Phi_I^{(1)}(x) = \frac{iga}{\omega} e^{Kz} e^{-iKx\cos\beta - iKy\sin\beta}, \text{ in deep water} \tag{2.15}$$

$$\Phi_I^{(1)}(x) = -i\frac{ag}{\omega}\frac{\cosh(k(D+z))}{\cosh(kD)} e^{i\vec{k}\cdot\vec{x}}, \text{ in shallow water} \tag{2.16}$$

where k is wave number; β is wave direction and a is the wave amplitude.

2.3. Boundary integral equation

By implementing the Green function, $G(x, x')$ to the hull surface in a linear potential flow problem, a three-dimensional problem within the wave field can be transferred to the two-dimensional problem on the hull's surface S_B. This yields the boundary integral equation (BIE) with respect to the source distribution σ and the hull surface.

With the flow points x and source points x', the boundary integral equation for $x \in S_B$, can be written as:

$$\frac{1}{2}\sigma_{D,R_j}(x) - \frac{1}{4\pi}\int_{S_B} \partial_n G(x, x')\sigma_{D,R_j}(x')dS' = \mathcal{N}_{D,R_j}(x). \tag{2.17}$$

The diffraction normal condition of the body can be written as:

$$\mathcal{N}_{D,R_j}(x) = -\partial_n \Phi_I^{(1)}(x) \tag{2.18}$$

The radiation normal condition can be written as:

$$\mathcal{N}_R(x) = \partial_n \Phi^(1)_{R_j}(x) \tag{2.19}$$

where $\Phi_{R_j}(x)$ is the jth component of the radiation normal potential ψ.

By implementing the BIE to total potential function, the radiation potential function and wave diffraction function can be further calculated as:

$$\Phi_{D,R_j}^{(1)}(x) = -\frac{1}{4\pi}\int_{S_B} G(x, x')\sigma_{D,R_j}(x')dS' \tag{2.20}$$

$$\partial_x \Phi_{D,R_j}^{(1)}(x) = \frac{1}{2}\sigma_{D,R_j}(x)n\delta_{xx'} - \frac{1}{4\pi}\int_{S_B} \partial_x G(zx, x')\sigma_{D,R_j}(x')dS' \tag{2.21}$$

where $\delta_{xx'}$ is the Kronecker delta. $\delta_{xx'} = 1$ for $x = x'$, and $\delta_{xx'} = 0$ otherwise.

2.4. Response amplitude operators and impulse frequency function

Diffraction potential is a combination of incident and scattered potentials. For calculating the exciting forces, diffraction potential is used:

$$F_{exc}^{(1)} = \rho \iint_{S_B} -i\omega \left[\Phi_I^{(1)} + \Phi_S^{(1)}\right] \nu dS \tag{2.22}$$

Then we have:

$$M_{ij}^a = -\rho \iint_{S_B} \nu_i Re\left\{\psi_{R_j}\right\} dS \tag{2.23}$$

$$B_{ij} = -\rho\omega \iint_{S_B} \nu_i Im\left\{\psi_{R_j}\right\} dS \tag{2.24}$$

where M_{ij}^a is added mass matrix and B_{ij} is damping coefficient matrix. These two terms correspond to the components that are in phase with the acceleration and velocity of the structure[42]. Added mass is a virtual mass that is associated with accelerated waves due to the presence of the structure. The damping coefficient[43] is a dimensionless measurement of how the system's oscillation decays.

A unit impulse is commonly used as a standard input for linear systems in the time domain, which produces an "impulse response" with a Fourier transform that is equivalent to the frequency response function. Impulse response function ($IRF(t)$) is utilized to describe the reaction of the system as a function of time mathematically, which allows the radiation potential to be solved from the impulse signal[44].

Then we can have the ($IRF(t)$) for damping and for excitation force ($IRF_{ex}(t)$) respectively, which is given as:

$$IRF(t) \approx \frac{2}{\pi} \int_0^{\omega_{max}} [B](\omega)\cos(\omega t) d\omega \tag{2.25}$$

$$IRF_{exc}(t) \approx \frac{1}{2\pi} \int_{-\omega_{max}}^{\omega_{max}} F_{exc}(\omega) e^{-i\omega t} d\omega \tag{2.26}$$

And we also have the infinite frequency added mass matrix which gives the body's instantaneous response to acceleration ($[M^a](\infty)$) as:

$$[M^a](\infty) \approx \frac{1}{N_\omega} \sum_{i=1}^{N_\omega} [M^a](\omega_i) + \int_0^{t_{max}} IRF(t)\sin(\omega_i t) dt \tag{2.27}$$

$$\tag{2.28}$$

Response Amplitude Operators (RAO) therefore can be calculated as follows:

$$\left[-[M + M_a(\omega)]\omega^2 - i\omega[B(\omega) + B_{add}] + [K_h + K_M]\right] \xi(\omega) = F_{exc}(\omega) \tag{2.29}$$

where $[B_{add}]$ and $[K_M]$ are additional damping and stiffness matrices defined by users.

2.5. Wave energy transfer

Wave propagation induced by oscillations in water particles is always accompanied by energy transfer, which facilitates the transmission of energy in sea waves. After the wave energy is captured from the sea waves, it undergoes a process of energy conversion that involves transforming the mechanical energy of the waves into electrical energy, which can be used for a range of applications. Potential theory can be employed to quantify the potential energy that can be captured from sea waves.

When considering energy transfer under regular waves, a sinusoidal waveform is often utilized. Applying potential theory, the resulting expression for the total energy, averaged over one wave

cycle, per unit surface area within the water column, can be formulated as:

$$E_{total} = E_{kinetic} + E_{potential} = \frac{1}{4}\rho g\zeta_a^2 + \frac{1}{4}\rho g\zeta_a^2 = \frac{1}{2}\rho g\zeta_a^2 = \frac{1}{8}\rho g H^2 \tag{2.30}$$

where E_{total} is the total energy per unit surface area in waves, $E_{kinetic}$ is the kinetic energy per unit surface area in waves, $E_{potential}$ is the potential energy per unit surface area in waves.

For any wave frequency and water depth, the wave number k can be calculated from the dispersion relation:

$$\omega^2 = gk\tanh(kh) \tag{2.31}$$

where h is the water depth, ω is the wave frequency.

By implementing the dispersion relation, for any wave number k, frequency ω and water depth h, the wave propagation speed c can be calculated as:

$$c = \frac{L}{T} = \frac{\omega}{k} \tag{2.32}$$

$$L = \frac{2\pi}{k} \tag{2.33}$$

$$T = \frac{2\pi}{\omega} \tag{2.34}$$

To calculate the energy transfer over one wave cycle per wave crest, which is the power, group speed of the waves is needed:

$$c_g = cn \tag{2.35}$$

$$n = \frac{1}{2}(1 + \frac{2kh}{cosh2kh}) \tag{2.36}$$

where c_g is the group speed of propagating waves in shallow water conditions. Hence, we can have the power $\bar{P}_w$ as:

$$\bar{P}_w = E_{total}c_g \tag{2.37}$$

When dealing with the cases in reality, the open sea contains a wide range of frequencies, which makes it rare to observe monochromatic waves. Therefore, to estimate energy transfer accurately in sea states that are composed of multiple wave frequencies, wave energy spectra were developed. Offshore measurements of surface elevation performed at different locations gives elevation signals, and by employing Fourier Transformation, the elevation signals can associate each discrete frequency within the frequency range with a specific energy contribution to the total energy. The crucial part is to characterize the statistical properties of the sea state rather than focusing on instantaneous elevation or energy transfer. By utilizing the superposition principle, linear way theory allows the total energy and average energy transfer to be obtained.

Therefore, when considering irregular waves, the frequency-dependent energy density, $S_\zeta(\omega)$ shows the properties of the sea states. The wave amplitude of the irregular waves can be obtained from the energy spectrum according to:

$$S_\zeta(\omega_n)\Delta\omega = \frac{1}{2}\zeta_{a_n}^2 \tag{2.38}$$

where $S_\zeta(\omega_n)$ is the energy density at frequency ω_n, $\Delta\omega$ is the frequency interval, and ζ_{a_n} is the wave amplitude.

The resulting total energy for irregular waves per unit surface area E_{total} can be therefore calculated as:

$$E_{total} = \rho g \int_0^\infty S_\zeta(\omega)\, d\omega \tag{2.39}$$

The average power transfer over a sea state that consists of N frequencies, therefore, can be written as:

$$\bar{P}_w = \sum_{n=1}^{N} E_{total_n} c_g \tag{2.40}$$

It is important to acknowledge that the selection of an appropriate frequency resolution significantly impacts the accuracy of the aforementioned computations. It is recommended to choose a frequency resolution that ensures the convergence of total energy and power. In the field of offshore engineering, various wave energy spectra have been employed. JONSWAP spectrum[45], which originated from the Joint North Sea Wave Project and was founded and developed in 1973, is one of the widest-used spectrums in studies. Developed through non-linear, wave-wave interactions, JONSWAP spectrum was derived and is widely acknowledged as the representative wave energy spectrum for the North Sea and other fetch-limited seas worldwide.

The formula of JONSWAP spectrum is written as:

$$S(\omega) = \frac{\alpha g^2}{\omega^5} \exp\left[-\beta \frac{\omega_p^4}{\omega^4}\right] \gamma^a \tag{2.41}$$

where

$$a = \exp\left[-\frac{(\omega - \omega_p)^2}{2 w_p^2 \sigma^2}\right] \tag{2.42}$$

$$\sigma = \begin{cases} 0.07 & \text{if } \omega \leq \omega_p \\ 0.09 & \text{if } \omega > \omega_p \end{cases} \tag{2.43}$$

a is the Phillips constant that derived from experimental data, $\gamma = 3.3$, which is the peakness factor, ω is the wave frequency, ω_p is the peak wave-frequency.

Hydrostatic and Hydrodynamic Forces

In the context of wave energy conversion and power extraction, once the potentials of the diffracted wave, radiated wave, and incoming wave are determined, the fluid pressure can be calculated by applying Bernoulli's equation, a reduced form of the Navier stokes equation:

$$p = -\rho \frac{\partial \Phi^{(1)}}{\partial t} - \frac{1}{2}\rho \nabla \Phi^{(1)} \cdot \nabla \Phi - \rho g z \tag{2.44}$$

where Φ is the time-dependent total velocity potential. For interaction between wave and structure, the higher order fluid pressure can be calculated as:

$$-\frac{1}{2}\rho \nabla \Phi \cdot \nabla \Phi = -\frac{1}{2}\rho |\vec{V}|^2 \tag{2.45}$$

In practice, the fluid velocity is relatively small, hence the second-order fluid pressure can be neglected, which gives the linearized pressure:

$$p = -\rho \frac{\partial \Phi}{\partial t} - \rho g z \tag{2.46}$$

Therefore, in frequency domain, the fluid pressure can be given as:

$$p = -i\omega\rho\Phi^{(1)} - \rho g z \tag{2.47}$$

By employing the potential decomposition, which is given as:

$$\Phi^{(1)} = \Phi_0^{(1)} + \Phi_7^{(1)} + i\omega \sum_{j=1}^{6} \xi_j \Phi_j^{(1)} \tag{2.48}$$

the pressure can further be written as:

$$p = -i\omega\rho \left(\Phi_0^{(1)} + \Phi_7^{(1)} + i\omega \sum_{j=1}^{6} \xi_j \Phi_j^{(1)} \right) - \rho g z \tag{2.49}$$

Figure 2.3 shows a floating structure's interaction with fluid in global coordinates, which depicts the vectors used in the following calculation to get hydrostatic force.

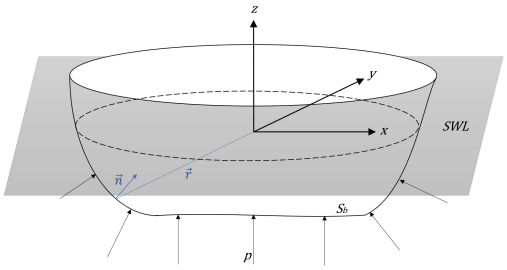

Figure 2.3: Floating structure in global coordinate system

The forces acting on the structure are:

$$F_i = \iint_{S_b} p n_i dS \tag{2.50}$$

where n_i is the extended normal vector component, $n_i = (\vec{n}, \vec{r} \times \vec{n})$. And $\vec{r}$ is the vector from the origin to the small surface on the hull. By substituting the fluid pressure into the integral for the force components, the force is given as:

$$F_i = \iint_{S_b} \left[-i\omega\rho \left(\Phi_0^{(1)} + \Phi_7^{(1)} + i\omega \sum_{j=1}^{6} \xi_j \Phi_j^{(1)} \right) - \rho g z \right] n_i dS, i = 1, 2, ..., 6 \tag{2.51}$$

This expression can be further written as a combination of the wave diffraction force, wave radiation force and the hydrostatic force as:

$$F_i = -i\omega\rho \iint_{S_b} \left(\Phi_0^{(1)} + \Phi_7^{(1)} \right) n_i dS + \rho\omega^2 \iint_{S_b} \left(\sum_{j=1}^{6} \xi_j \Phi_j^{(1)} \right) n_i dS - \rho g \iint_{S_b} z n_i dS \tag{2.52}$$

2.5.1. Hydrostatic force

According to Archimedes' law, as the floater oscillates through the water's surface, it encounters a buoyancy force that is directly proportional to the volume of water displaced by the buoy. This force, named hydrostatic force, oscillates as the displaced volume varies with the floater's motion, which results in restoring the buoy to its equilibrium position, where the buoyancy force equals the force of gravity.

The hydrostatic force is formulated by 6 components, and the expression is given as:

$$F_i^S = -\rho g \iint_{S_b} z n_i dS \quad \text{with } i = 1, 2, \ldots, 6 \tag{2.53}$$

In principle, when calculating hydrostatic forces using this formula directly, the resulting forces will be of zero order. These zero-order forces tend to be the largest in wave-structure interaction scenarios. However, these forces are balanced by the weight of the structure in equilibrium. In the analysis of wave-structure interaction, there are net hydrostatic forces that arise from the structure's motion, representing the deviation of the structure from its equilibrium position. These net hydrostatic forces can be considered restoring forces, which are first-order hydrostatic forces that are proportional to the structure's motion. The expression for this first-order hydrostatic force is given as:

$$F_i^S = -\sum_{j=1}^{6} c_{ij}\xi_j \quad \text{with } i = 1, 2, \ldots, 6 \tag{2.54}$$

where ξ_j is the motion of the structure in six degrees of freedom, c_{ij} are the restoring coefficients. The non-zero restoring coefficients can be calculated by:

$$\begin{aligned}
c_{33} &= \rho g \iint_{S_b} n_3 dS \\
c_{34} &= \rho g \iint_{S_b} y n_3 dS \\
c_{35} &= -\rho g \iint_{S_b} x n_3 dS \\
c_{44} &= \rho g \iint_{S_b} y^2 n_3 dS + mgz_b - mgz_g \\
c_{45} &= -\rho g \iint_{S_b} xy n_3 dS \\
c_{46} &= -mgx_b + mgx_g \\
c_{55} &= \rho g \iint_{S_b} x^2 n_3 dS + mgz_b - mgz_g \\
c_{56} &= -mgy_b + mgy_g
\end{aligned} \tag{2.55}$$

The center of buoyancy of the structure can be calculated by:

$$\begin{aligned}
x_b &= -\frac{1}{2\nabla} \iint_{S_b} x^2 n_1 dS \\
y_b &= -\frac{1}{2\nabla} \iint_{S_b} y^2 n_2 dS \\
z_b &= -\frac{1}{2\nabla} \iint_{S_b} z^2 n_3 dS
\end{aligned} \tag{2.56}$$

where ∇ is the volume of the fluid displaced by the structure, S_b is the surface on the structure.

2.5.2. Radiation forces

The floating object experiences a radiation force due to its oscillatory motion through the water's surface. This motion generates waves that radiate outward from the floater. While the wave radiates away from the floating body, the energy dissipates through the waves, and the amount of energy loss of this behaviour (damping) equals the wave energy dissipates. Consequently, a damping force produced by the dissipation of wave energy acts on the body to oppose its motion, specifically in the vertical direction (z-direction) for the heave case[46].

Furthermore, as the floater's oscillatory motion causes a portion of its volume to move in and out of the water mass, the water particles surrounding its solid surface will have an acceleration. This acceleration results in a net force on the buoy, known as the added mass force. Together with the damping force, the two force components contribute to radiation force.

Based on the expression for radiation potential given in 2.12, the corresponding pressure can be calculated in the frequency domain as:

$$p^R = \rho\omega^2 \sum_{j=1}^{6} \xi_j \Phi_j^{(1)} \tag{2.57}$$

By substituting the pressure into the surface integral, the radiation force can be calculated as:

$$F_i^R = \iint_{S_b} p^R n_i dS = \rho\omega^2 \iint_{S_b} \left(\sum_{j=1}^{6} \xi_j \Phi_j^{(1)} \right) n_i dS = \omega^2 \sum_{j=1}^{6} \left[\xi_j \left(\rho \iint_{S_b} \Phi_j^{(1)} \; n_i dS \right) \right] \tag{2.58}$$

The expression can be further be written as:

$$F_i^R = \omega^2 \sum_{j=1}^{6} \xi_j f_{ij} = \sum_{j=1}^{6} \left(\omega^2 a_{ij} - i\omega b_{ij} \right) \xi_j \tag{2.59}$$

where f_{ij} is the complex force in i direction due to the velocity of the structure in j direction. Therefore this complex form can be decomposed into a real part and an imaginary part as:

$$f_{ij} = \rho \iint_{S_b} \Phi_j^{(1)} n_i dS = \rho \iint_{S_b} \Phi_j^{(1)} \frac{\partial \Phi_i^{(1)}}{\partial n} dS = a_{ij} - \frac{i}{\omega} b_{ij} \tag{2.60}$$

where a_{ij} is the added mass coefficient given as: $a_{ij} = \mathrm{R}\,e\,(f_{ij})$, and b_{ij} is the damping coefficient, given as: $b_{ij} = -\,\mathrm{I}\,m\,(f_{ij}) \times \omega$.

In time domain, the radiation force is written as:

$$F_i^R = -\sum_{j=1}^{6} \left(a_{ij} \ddot{\xi}_j + b_{ij} \dot{\xi}_j \right) \tag{2.61}$$

2.5.3. Excitation forces

The waves induce disturbances in the pressure field around the rigid body when they approach the floating structure. This causes the pressure around the body to deviate from the hydrostatic state. According to potential theory, these disturbances are represented by the non-hydrostatic part on the right-hand side of Equation 2.2. The hydrostatic part (first term) of the pressure is accounted for as in F_i^R. Integrating the non-hydrostatic part of the pressure field gives rise to the Froude-Krylov force, which accounts for the effects of the wave disturbances. Additionally, the presence of the buoy further disrupts the pressure field, resulting in the diffraction force. These two components constitute the excitation force F_i^e.

As per the definition, the wave excitation on the floating structure results from the effects of the incoming and diffracted waves. The expression is given as:

$$p^{ex} = -\rho \frac{\partial \left(\Phi_0^{(1)} + \Phi_7^{(1)} \right)}{\partial t} = -i\omega\rho \left(\Phi_0^{(1)} + \Phi_7^{(1)} \right) \tag{2.62}$$

By adding up the two components of wave excitation force consists of two parts, which are part from the incoming wave, named Froude-Krylov force, and the part from the diffracted wave due to the existence of the structure, the force can be written as:

$$F_i^{ex} = -i\omega\rho \iint_{S_b} \left(\Phi_0^{(1)} + \Phi_7^{(1)} \right) n_i dS \tag{2.63}$$

The excitation force can be calculated by the formula if the diffraction potential $\Phi_7^{(1)}$ is solved, and the incoming wave potential $\Phi_0^{(1)}$ is known from the wave amplitude and frequency.

Because the motion of the structure is already taken into account in the radiation problem through the application of the superposition principle, wave excitation, defined as the wave-induced force acting on the assumed stationary structure, is independent of the structure's motion.

2.6. Dynamic equation in frequency domain

In offshore engineering, accurately predicting the response of a floating object to waves is crucial. During the design phase, a widely utilized model for describing the motion of floating objects is known as the mass-spring-damper model, whose derivation is based on analyzing the forces or moments exerted on the floating object.

For the point absorber in the context of this thesis, the heave motion is deemed the most significant among the six degrees of freedom. a translational constraint is imposed on the third degree of freedom, which restricts the floater's motion to solely vertical displacement. The derivation commences by analyzing the forces acting on the floating body, which are: excitation force F_i^{ex}, radiation force F_i^R, hydrostatic force F_i^S and PTO force F_i^{pto}. The term PTO force refers to the force exerted by the PTO system on the WEC. The force is generated as they convert the mechanical motion of the waves into usable electricity.

Considering the analysis of a rigid body's motion in waves, the dynamic equation can be determined by implementing Newton's Second Law, which states the total force acting on the floating structure equals the mass times the acceleration of the system. Consequently, the form of the equation is given by;

$$\sum_{j=1}^{6} M_{ij}\ddot{X}_j = F_i^{ex} + F_i^R + F_i^S \quad \text{with } i = 1, 2, \ldots, 6 \tag{2.64}$$

where M_{ij} is the mass of the system, given in a matrix form; $\ddot{X}_j$ is the acceleration of the system. The mass matrix is defined as:

$$M_{ij} = \begin{bmatrix} m & 0 & 0 & 0 & mz_G & -my_G \\ 0 & m & 0 & -mz_G & 0 & mx_G \\ 0 & 0 & m & my_G & -mx_G & 0 \\ 0 & -mz_G & my_G & I_{11} & I_{12} & I_{13} \\ mz_G & 0 & -mx_G & I_{21} & I_{22} & I_{23} \\ -my_G & mx_G & 0 & I_{31} & I_{32} & I_{33} \end{bmatrix} \tag{2.65}$$

where m is the mass of the floating body; $I_{ij}$when $i = j$ is the moment of inertia of the system, and $I_{ij}$when $i \neq j$ is the product of inertia of the system.

In reality, the dynamic equation needs to be represented in the time domain, as shown in Equation 2.64. However, in the case of a linear problem using frequency domain analysis will be much easier and faster. To transfer the time domain problem into the frequency domain, the following steps can be adopted.

The motion of the body can be written as:

$$X_j = \xi_j e^{i\omega t} \tag{2.66}$$

where ξ_j is the amplitude of motion noted in a complex form. The velocity V_j and the acceleration A_j can be further obtained in this frequency domain as:

$$\begin{aligned} V_j &= i\omega\xi_j \\ A_j &= -\omega^2\xi_j \end{aligned} \tag{2.67}$$

As we have had known the hydrostatic force, radiation force, and excitation force in the frequency domain from equation 2.54, 2.61 and 2.63, by substituting these expressions into the dynamic equation in the frequency domain, the dynamic equation for six degrees of freedom is obtained as:

$$\sum_{j=1}^{6}\left[-\omega^2\left(M_{ij}+M_{ij}^{a}\right)+i\omega B_{ij}+c_{ij}\right]\xi_j=F_i^{ex}\quad\text{with } i=1,2,\ldots,6 \tag{2.68}$$

Note that $\left(M_{ij}+M_{ij}^{a}\right)$ is the total mass matrix, B_{ij} is the damping coefficient matrix, c_{ij} is the restoring coefficient matrix. This expression can be further simplified as:

$$\sum_{j=1}^{6}C_{ij}\xi_j=F_i^{ex}\quad\text{with}\quad C_{ij}=-\omega^2\left(M_{ij}+a_{ij}\right)+i\omega b_{ij}+c_{ij} \tag{2.69}$$

In this report, the excitation force, added mass, and damping coefficient are calculated using the Boundary Element Method implemented in NEMOH. Additionally, the mass matrix and restoring coefficients are obtained based on the geometric properties of the rigid body. By combining these computed values, the dynamic equation is expressed in the frequency domain, which makes the calculation of motion amplitudes straightforward.

$$\xi_j=\sum_{i=1}^{6}\left[C_{ij}\right]^{-1}F_i^{ex}\quad\text{with } j=1,2,\ldots,6 \tag{2.70}$$

Thus, the non-dimensional response amplitude operator (RAO) is obtained:

$$Z_j(\omega,\beta)=\frac{\xi_j}{A} \tag{2.71}$$

here, Z_j represents the RAO, β is the incident angle with respect to the positive x-axis and A is the wave amplitude.

For a wave energy converter, the next step is to integrate a Power Take-Off system with the dynamic system of the floating structure. The PTO system is used for extracting the wave energy and converting it into electrical power. It is designed to efficiently capture the mechanical motion or hydraulic pressure generated by the floating structure's response to waves. In the context of this article, the point absorber uses a linear translational PTO for wave power extraction. As an example of using linear PTO to convert the energy from heave motion, the PTO force is given as:

$$F_3^{pto}=-M_{33}^{pto}\ddot{X}_3-B_{33}^{pto}\dot{X}_3-C_{33}^{pto}X_3 \tag{2.72}$$

where F_3^{pto} is the PTO force in heave motion direction, M_{33}^{pto} and C_{33}^{pto} are PTO coefficients are the characteristic parameters of the dynamic system in the control of improving energy conversion. B_{33}^{pto} is the PTO damping coefficient in heave motion direction. $\ddot{X}$ and $\dot{X}_3$ are the acceleration and velocity of heave motion. They can easily be obtained by:

$$\begin{aligned}\dot{X}_3&=i\omega\xi_3e^{i\omega t}\\ \ddot{X}_3&=-\omega^2\xi_3e^{i\omega t}\end{aligned} \tag{2.73}$$

Therefore, the frequency domain expression can be obtained by substituting the velocity and acceleration as:

$$F_3^{pto}=\omega^2M_{33}^{pto}\xi_3-i\omega B_{33}^{pto}\xi_3-C_{33}^{pto}\xi_3 \tag{2.74}$$

Taking the PTO force into account, the full expression for the dynamic system is written as:

$$\left[-\omega^2\left(M_{33}+a_{33}+M_{33}^{pto}\right)+i\omega\left(b_{33}+B_{33}^{pto}\right)+\left(c_{33}+C_{33}^{pto}\right)\right]\xi_3=F_3^{ex} \tag{2.75}$$

The amplitude of the heave motion then can be solved as:

$$\xi_3=\frac{F_3^{\mathrm{ex}}}{-\omega^2\left(M_{33}+a_{33}+M_{33}^{\mathrm{pto}}\right)+i\omega\left(b_{33}+B_{33}^{\mathrm{pto}}\right)+\left(c_{33}+C_{33}^{\mathrm{pto}}\right)} \tag{2.76}$$

The average power absorption can be calculated by[47]:

$$\bar{P} = -\frac{1}{2}\,\mathrm{Re}\left(F_3^{pto} \cdot V_3^*\right) \tag{2.77}$$

here, $V_3 = i\omega\xi_3$, and V_3^* is the conjugate of V_3.

By analyzing each term of Equation 2.1 and calculating the average power absorption from the force term, it can be observed that the resulting values from the first and third terms are both 0. This implies that, although the added mass and restoring coefficients of PTO system change the characteristics of the dynamic system and improve the conversion, the terms involving them give an average overall power absorption of 0 in the system[48]. Therefore, the only term that influences the final power absorption is the one involving the Power Take-Off damping coefficient. This highlights the significance of the PTO damping coefficient in determining the efficiency and effectiveness of a linear PTO system in absorbing and extracting power from the wave energy. And the average power absorbed is calculated as:

$$\bar{P} = -\frac{1}{2}\,\mathrm{Re}\left(-i\omega B_{33}^{pto}\xi_3 \cdot V_3^*\right) = -\frac{1}{2}\,\mathrm{Re}\left(-i\omega B_{33}^{pto}\xi_3 \cdot -i\omega\xi_3^*\right) = \frac{1}{2}\omega^2 B_{33}^{pto}\left|\xi_3\right|^2 \tag{2.78}$$

3

Numerical model set up

3.1. Investigation on computational capability of NEMOH

The original version of Nemoh was an open-source software designed for solving first-order hydrodynamic coefficients in the frequency domain. In this research it is chosen for being able to solve hydrodynamic problems on an array with multiple bodies, being open-source, and being verified in previous studies for its 2.8 version. In its latest update, NEMOH introduced version 3.0 on December 2nd, 2022. This new release incorporates several additional modules, including the ability to post-process hydrodynamic results, compute Quadratic Transfer Functions, implement an irregular frequency removal method, and enhance Green's function with finer integration points.

In this article, NEMOH 3.0 was chosen to perform hydrodynamic analysis for the reasons of being faster in dealing with large amounts of frequencies in calculation, and the capability of computing the cases with multi-directional waves. The following comparison between NEMOH 3.0, the newly updated version, and its predecessor, NEMOH 2.8 demonstrates the endeavour for finding out the aforementioned two reasons. The purpose of this comparison is to assess the capabilities of the two versions and identify any unexpected outcomes or unresolved dependencies that may have been introduced in the latest release. Also, as the accuracy of NEMOH 2.8 has been verified in [15], a closeness of the result produced by NEMOH 3.0 to NEMOH 2.8 can be used to verify NEMOH 3.0.

The methodology employed in this stage can be summarized as follows:

- Test WEC Model Establishment: developing a test WEC model in ANSYS SpaceClaim.
- Hydrodynamic Analysis in NEMOH 2.8: calculation of hydrodynamic coefficients associated with the WEC.
- RAO calculation by using results from NEMOH 2.8.
- Hydrodynamic Analysis in NEMOH 3.0: calculation of hydrodynamic coefficients for the WEC. Obtaining RAO by using the post-process module.
- Comparison of the results calculated by NEMOH 2.8 and NEMOH 3.0.

3.1.1. Point absorber test model

The geometry model of the test point absorber is built using solid modeling CAD software ANSYS SpaceClaim[49]. Once the geometry model is established, it is exported as a .stl file. Subsequently, the .stl file will be imported into BEMRosetta software[50], which converts the geometry files to the format used in BEM solvers. This mesh file serves as the computational grid for further analysis and simulations related to the test point absorber.

In both NEMOH 2.8 and 3.0, it has been observed that using an entire geometry model built in ANSYS SpaceClaim and then being meshed for analysis can lead to abnormal outcomes. Therefore, it is necessary to modify the model to only include the part of the geometry below the waterplane in ANSYS SpaceClaim before meshing it. However, for future computation in WEC-Sim, the complete

geometry model should be preserved in a separate .stl file, which is used for visualizing and presenting simulation animations of the PA's motions.

The geometry below waterplane in Space Claim is shown in figure 3.1. The meshed geometry is shown in figure 3.2

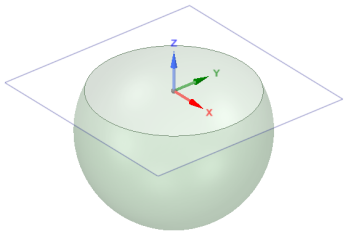

Figure 3.1: Test point absorber geometry, in Space Claim

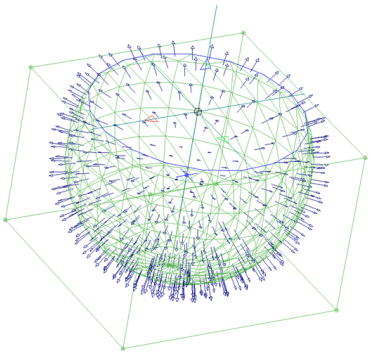

Figure 3.2: Test point absorber meshed in BEMRosetta

The information of this test geometry can be obtained after processing in BEMRosetta, which is summarized in table 3.1.

Table 3.1: Summary of test PA model

Features	Unit	Value
Wetted surface	m^2	508.59
Immersed volume	m^3	1411.48
G_z	m	4.07e-16
Mass of Device	kg	1411482.32
R	m	7.5
Number of nodes	-	125
Number of panels	-	218

3.1.2. Running speed evaluation of NEMOH 2.8 and 3.0

NEMOH 2.8 and 3.0 versions have different code structures to run, therefore, to accurately compare the running speed between NEMOH 2.8 and 3.0, it is important to ensure that the inputs used by both versions are identical. Here are the steps involved in comparing the running speed while maintaining the same outcomes:

- Getting results in NEMOH 3.0: Run the "*getstarted.m*" file provided in the software, which refers to the different cases located in separate folders. This initiates the calculation process in NEMOH 3.0. And the outcomes should involve added mass coefficient, damping coefficient, excitation force, a plot of the aforementioned results and an RAO plot.
- Getting results in NEMOH 2.8: Create a "*nemoh_run.m*" file and place it in the corresponding case folder to start NEMOH 2.8 and run this file. In this version, the results are not automatically plotted.
- Plotting Results in NEMOH 2.8: To ensure consistent outcome with NEMOH 3.0, write an additional .m file specifically to plot the same results as those automatically generated in NEMOH 3.0, including added mass coefficient, damping coefficient and excitation force. The script is attached in the appendix.
- Calculation of RAO in NEMOH 2.8: Unlike NEMOH 3.0, NEMOH 2.8 does not have a built-in function to compute the Response Amplitude Operator (RAO). So an additional code file is written to calculate the RAO from the results obtained in NEMOH 2.8.
- Comparing Computation Time: To compare the calculation time with NEMOH 3.0, the total time taken by each computation module in NEMOH 2.8 is added up.

Each run was performed five times with 20 frequencies, and the time for each run was recorded. The calculations were run on a computer with an 11th Generation Intel Core i7 processor running at 3.0 GHz using 16.0 GB of RAM, in Windows 11 operating system. Table3.2 presents the total running time comparison between NEMOH 2.8 and NEMOH 3.0 for the same case.

Table 3.2: Running time recording for 20 frequencies

	NEMOH 2.8					NEMOH 3.0
2-7		Coefficients	Plotting	RAO	Total time	Coefficients + Plotting + RAO
1	s	14.2	1.9	0.4	16.5	23.7
2	s	13.0	1.0	0.5	14.5	23.6
3	s	11.6	1.0	1.9	14.5	23.6
4	s	10.2	1.8	0.8	12.9	24.5
5	s	10.8	2.0	0.7	13.5	24.0
Average	s				14.4	23.9

From the comparison in the table, NEMOH 2.8 has shown faster computation speed in the case of 20 frequencies. However, it is important to consider the overall advantages of NEMOH 3.0. The mere computation time in NEMOH 3.0 plays a relatively minor part, while most of the time is spent on the initialization of the code due to the structure of the software. Therefore, when the number of frequencies is doubled to 40, only a small increase was observed in the total computation time, which results in about 26 seconds. This indicates that NEMOH 3.0 has an advantage in cases where a large number of frequencies is required.

After increasing the number of frequencies to 40, the time consumed is shown in table 3.3.

Table 3.3: Running time recording for 40 frequencies

		NEMOH 2.8				NEMOH 3.0
2-7		Coefficients	Plotting	RAO	Total time	Coefficients + Plotting + RAO
1	s	29.1	1.8	0.7	31.6	25.7
2	s	24.4	1.3	0.5	26.2	26.5
3	s	23.3	1.1	0.6	24.0	25.3
4	s	24.2	1.6	1.2	27.0	26.1
5	s	20.9	1.8	0.9	23.6	27.6
Average	s				26.5	26.3

Additionally, NEMOH 3.0 has benefits when it comes to calculations involving multiple wave directions. While in NEMOH 2.8, this is hard to achieve since the code auto-corrects the wave directions to a single direction (shown in figure 3.3), unless a manual modification of the code is performed. This is particularly relevant for WEC-Sim simulations, because in WEC-Sim, to perform a simulation considering irregular waves, a wave directionary should be added as a parameter. Here in figure 3.4, a sample set of irregular waves in WEC-Sim is presented.

```
if (n == 9+18*nBodies)
    textline(n)={sprintf('%g %f %f       ! Number of wave frequencies, Min, and Max (rad/s)',length(w),w(1),w(length(w)))};
end
 if (n == 10+18*nBodies)
    textline(n)={sprintf('%g %f %f      ! Number of wave directions, Min and Max (degrees)',1,dir,dir)};
end
n=n+1;
```

Figure 3.3: Code in NEMOH 2.8 that shows single wave direction calculation

```
% Irregular Waves using JS Spectrum with Directionality
waves = waveClass('irregular');
waves.height = 2:2:20; waves.period = [3 4 5 6 7 8 9 10 11 12 13]; % Initialize Wave Class and Specify Type
waves.spectrumType = 'JS';              % Specify Spectrum Type
waves.direction = [0,10,40];            % Wave Directionality [deg]
waves.spread = [0.1,0.2,0.7];           % Wave Directional Spreading [%}
```

Figure 3.4: Sample code for setting up irregular wave in WEC-Sim

Therefore, while NEMOH 2.8 may demonstrate faster computation speed in certain scenarios, the capabilities of NEMOH 3.0, including its efficiency with increased frequencies and ability to handle multiple wave directions, make it a better choice for hydrodynamic calculations, especially in the context of collaboration with WEC-Sim simulations.

3.1.3. Results visualization in NEMOH 2.8 and NEMOH 3.0

After initiating the calculation in NEMOH 3.0, a figure displaying the hydrodynamic characteristics against 20 frequencies will be plotted. The components include added mass coefficients and damping coefficients in surge, heave, and pitch direction, as well as the excitation force in surge, heave, and pitch direction. The plot is attached in the appendix. And by running an additional code composed manually that reads results from NEMOH 2.8, the same set of components of hydrodynamic characteristics is attached in the appendix.

From the two separated figures, close similarity can be identified through the shape of each curve. A figure3.5 that combines both results is presented to highlight the consistency and similarity between the hydrodynamic characteristics obtained from both versions.

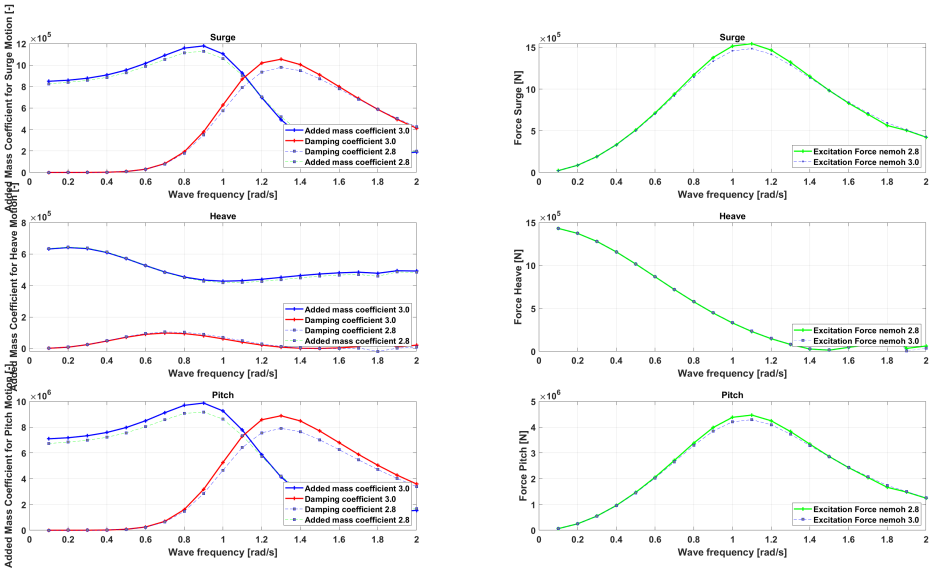

Figure 3.5: Hydrodynamic characteristics obtained from NEMOH 2.8 and 3.0 co-plot

Figure 3.5 shows evidence that the hydrodynamic coefficient curves obtained from NEMOH 2.8 and NEMOH 3.0 exhibit a high degree of similarity. Only minor differences are observed at each peak of the curves, which can be attributed to the variations in code structures or numerical techniques employed in the two versions.

By examining the overall resemblance and consistency between the results for the test PA, the hydrodynamic computation module in NEMOH 3.0 can be considered reliable and trustworthy.

3.1.4. Post-processing verification: RAO computation in NEMOH 3.0

A new module introduced in NEMOH 3.0 allows for the Response Amplitude Operator to be calculated by using hydrodynamic calculation results obtained from NEMOH Module 1. This is achieved by switching the index in the "*nemoh.cal*" file from 0 to 1. In this section, a manual calculation of the Response Amplitude Operator using the hydrodynamic results obtained from NEMOH 2.8 is performed. This aims to provide a comparison with the RAO calculation module in the updated version of NEMOH 3.0.

The following equation was used in computing RAO.

$$\boldsymbol{RAO}(\omega, \mathrm{dir}) = \left\{-\omega^2 \cdot (\mathbf{M} + \mathbf{A}(\omega)) + i\omega \cdot \mathbf{B}(\omega) + \mathbf{C}\right\}^{-1} \cdot \mathbf{F}(\omega,\ \mathrm{dir}\ ) \tag{3.1}$$

where $\mathbf{M}$ is the mass matrix that can be calculated from the geometry of the model, $\mathbf{A}$,$\mathbf{B}$ and $\mathbf{F}(\omega,\ \mathrm{dir}\ )$ are the added mass coefficient, damping coefficient ad excitation force matrices that obtained from result files in NEMOH, $\mathbf{C}$ is the restoring coefficient matrix that can be obtained from BEMRosetta.

As for the point absorber involved in this study, heave motion is the most identical in power generation, the following figure 3.6 presents a comparison between the RAOs in heave motion direction. Note that the results from NEMOH 3.0 shows multiple lines, which indicates that multiple wave directions were calculated in NEMOH 3.0.

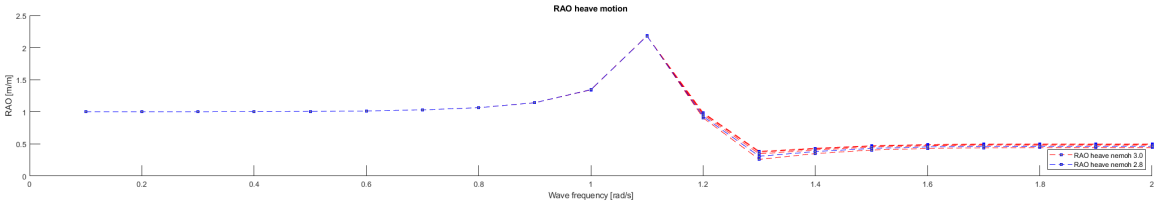

Figure 3.6: RAO in heave motion obtained from NEMOH 2.8 and 3.0

As seen in the comparison above, the RAO results obtained from mentioned 2 NEMOH versions also show a resemblance, which gains trustworthiness for NEMOH 3.0 version's newly updated module.

3.1.5. Investigation on the Consistency of NEMOH 3.0 and WEC-Sim

In WEC-Sim, some files obtained from NEMOH are used for generating hydrodata files via BEMIO so as to conduct the simulations. These files include the "*nemoh.cal*" file, which contains essential parameters in the calculation, the ID.dat file, the hydrodynamic calculation results in the .tec file format, and the mesh.cal file.

It is important to note that the latest update to WEC-Sim [51] was released in September 2022, while NEMOH 3.0 was updated in December 2022. Also, NEMOH 3.0 was observed to have adopted some changes in file structures in comparison to its previous version, NEMOH 2.8. Hence, some files that could be read by WEC-Sim in the previous version of NEMOH are not read in the latest version of NEMOH. This makes it essential to perform a consistency checks between NEMOH 3.0 and WEC-Sim if we intend to undertake research utilizing NEMOH 3.0.

During the consistency check, several issues were encountered during the running the BEMIO calculator in WEC-Sim when using the results file from NEMOH 3.0. The first issue was due to an evident modification in the code line for "Load cases to be solved", in which in NEMOH 2.8, three inputs are required to specify the number of wave frequencies, the minimum frequency, and the maximum frequency(shown in figure 3.7). However, in NEMOH 3.0, an additional input indicating the frequency unit was added to the front of this line, resulting in four inputs(shown in figure3.8). Therefore while using the files from NEMOH 3.0, to ensure compatibility with WEC-Sim, the first input in the "Load cases to be solved" line needed to be removed from the "*nemoh.cal*" file.

```
--- Load cases to be solved ---------------------------------------------------
20 0.100000 2.000000       ! Number of wave frequencies, Min, and Max (rad/s)
1 0.000000 0.000000     ! Number of wave directions, Min and Max (degrees)
```

Figure 3.7: Load case line in NEMOH 2.8

```
--- Load cases to be solved ---------------------------------------------------------------------
1  20   0.1 2.0     ! Freq type 1,2,3=[rad/s,Hz,s], Number of wave frequencies/periods, Min, and Max
10  0.  90      ! Number of wave directions, Min and Max (degrees)
```

Figure 3.8: Load case line in NEMOH 3.0

Following this adjustment, errors persisted when BEMIO attempted to read the files from NEMOH. Further examination of the BEMIO source code revealed another discrepancy in the NEMOH 3.0 results files. The source code of BEMIO shows that it searches for a text line reading "Diffraction force" to retrieve the excitation force matrix(seen in figure3.9). However, it was found that, while the "ExcitationForce.tec" output file in NEMOH 2.8 contained the text line "Diffraction force" (figure 3.10) for each frequency case, NEMOH 3.0's output file used the text line "Excitation force" instead (figure 3.11). This alteration in NEMOH 3.0 prevented BEMIO from successfully reading the result file and retrieving the necessary data.

```
%% Excitation Force file
fileID = fopen(fullfile(resultsdir,'ExcitationForce.tec'));
raw = textscan(fileID,'%[^\n\r]');
raw = raw{:};
fclose(fileID);
N = length(raw);
i = 0;
for n = 1:N
    if isempty(strfind(raw{n},'Diffraction force'))==0
        i = i+1;
        for k = 1:hydro(F).Nf
            tmp = textscan(raw{n+k},'%f');
            hydro(F).ex_ma(:,i,k) = tmp{1,1}(2:2:end);  % Magnitude of exciting force
            hydro(F).ex_ph(:,i,k) = -tmp{1,1}(3:2:end);  % Phase of exciting force (-ph, since NEMOH's x-dir is flipped)
        end
    end
end
hydro(F).ex_re = hydro(F).ex_ma.*cos(hydro(F).ex_ph);  % Real part of exciting force
hydro(F).ex_im = hydro(F).ex_ma.*sin(hydro(F).ex_ph);  % Imaginary part of exciting force
waitbar(5/8);
```

Figure 3.9: Source code indicating BEMIO read “Diffraction force” text line

```
Zone t="Diffraction force - beta =   0.000 deg",I=    20,F=POINT
  0.1000000E+00  0.1075695E+04 -0.1570706E+01  0.2566910E-01 -0.1747334E-03  0.5626042E+06 -0.1967120E-03  0.1382141E+00  0.3141367E+01
  0.2000000E+00  0.4270163E+04 -0.1570694E+01  0.2422821E-01  0.5030503E-02  0.5513049E+06 -0.3043680E-02  0.8050698E-02  0.6254662E-02
  0.3000000E+00  0.9475181E+04 -0.1570766E+01  0.8798808E-02 -0.3102585E+01  0.5327586E+06 -0.1451750E-01  0.8936274E-01 -0.3136466E+01
  0.4000000E+00  0.1646581E+05 -0.1571952E+01  0.5423030E-02  0.2906168E+01  0.5104094E+06 -0.4124574E-01  0.8983709E-01  0.1988220E-01
```

Figure 3.10: Concerning part of “ExcitationForce.tec” file in NEMOH 2.8

```
Zone t="Excitation force - beta =   0.000 deg",I=    20,F=POINT
  0.1000000E+00  0.1077030E+04 -0.1570708E+01  0.2572480E-01  0.6224650E-03  0.5628169E+06 -0.1967088E-03  0.1389496E+00  0.3141237E+01
  0.2000000E+00  0.4277626E+04 -0.1570700E+01  0.2341318E-01 -0.2843122E-02  0.5522163E+06 -0.3037912E-02  0.1026322E-01 -0.2497992E-01
  0.3000000E+00  0.9497635E+04 -0.1570886E+01  0.9806128E-02  0.3103986E+01  0.5351155E+06 -0.1433504E-01  0.8995656E-01  0.3127399E+01
  0.4000000E+00  0.1651507E+05 -0.1573013E+01  0.1371719E-02  0.2022006E+01  0.5155032E+06 -0.3947799E-01  0.8563889E-01 -0.3973478E-01
```

Figure 3.11: Concerning part of “ExcitationForce.tec” file in NEMOH 3.0

Consequently, in order to use NEMOH 3.0 for simulations in WEC-Sim, a code file was written to replace every instance of “Excitation force” with “Diffraction force” in the NEMOH 3.0 result file. This modification ensured seamless execution of BEMIO with the NEMOH 3.0 files, resolving the issues of inconsistency between NEMOH 3.0 and WEC-Sim that were previously encountered.

3.2. Final PA model dimensioning

To downscale the empirical large WEC models that have been proposed, for this optimization, a relatively small-sized point absorber is chosen. This PA model adopts a spherical geometry, with a radius of 5 m. The draft to radius ratios is set as $\frac{1}{2}$. As the downscaling should also take the constraints and other configurations like PTO system into account. Also as this research has a main focus on the hydrodynamic interactions rather than the role that PTO system plays. Therefore a linear PTO with a PTO damping coefficient of 8 $kN/-s/m$ is selected to match this device, which is close to the radiation damping, to make the effects of damping play less role. Finally, the geometry model of the PA is set up as in figure 3.12, and the meshed model as in figure 3.13. The properties of this PA model are summarized in table 3.4.

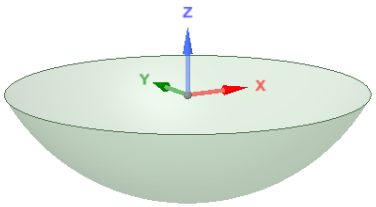

Figure 3.12: Point absorber geometry model

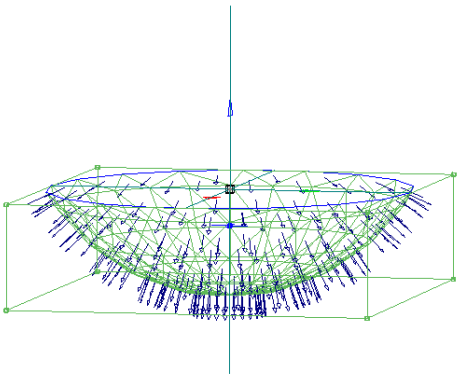

Figure 3.13: Point absorber meshed model

It is noted that this model was established before the dimensioning of the final PA model used in the array optimization. Therefore this model does not imply a serious concern about the properties, for example, the mass and the draft.

Table 3.4: Summary of final PA model

Features	Unit	Value
Wetted surface	m^2	77.22
Immersed volume	m^3	79.31
Initial draft	m	2.5
Draft-radius ratio	-	1/2
G_z	m	1.25e-16
Mass	kg	79306.9
Radius	m	5
Number of nodes	-	678
Number of panels	-	226
PTO damping coefficient	$kN/-s/m$	8

3.3. Verification of WEC-Sim simulation

After the determination of the PA model, a verification of the WEC-Sim simulation is performed. This involves conducting a simulation in an irregular wave to generate a power matrix, which will then be compared to a manually calculated power matrix obtained through a semi-analytical method.

The manual calculation of the power matrix utilizes Equation 2.78, in which the PA's motion is obtained from the hydrodynamic analysis conducted in NEMOH 3.0. Since the way of obtaining RAO results for multibody cases in NEMOH 3.0 is not very straightforward, only one PA is involved during this stage of verification.

In WEC-Sim, the "*bemio.m*" file contains Boundary Element Method Input/Output (BEMIO) functions that are used to pre-process the BEM hydrodynamic data from other software in order to run WEC-Sim. As discussed before, while being associated with NEMOH, some results files and basic input files are utilized. The files needed are: results files including diffraction force file, excitation force file, Froude–Krylov force file and radiation coefficient file; model profile files including hydrostatic information file, model mesh file, restoring coefficient file; and additional files including "*ID.dat*", "*input.txt*, ", "*mesh.cal*" file and "*nemoh.cal*" files used in NEMOH.

3.3.1. Methodology

The methodology follows these steps to perform the verification:

- Running the BEMIO code: this requires importing the required files and configuring *bemio.m* file.
- Setting up WEC-Sim input file: this is done by filling in the "*wecSimInputFile.m*" provided in WEC-Sim. A single wave case can be defined to start with. If a power matrix is to be generated, a series of waves should be specified. In this study, a JONSWAP wave spectrum is used, with the peak period ranging from 3s to 13s, and the significant wave height ranges from 2m to 20m.
- Configuring constraints and PTO parameters: Constraints and PTO parameters are also set up in "*wecSimInputFile.m*". A translational constraint is used to restrict the motion to heave direction, which is the focus of this study. The PTO has been configured as a translational linear PTO accordingly.
- Setting up the Simulink model: A Simulink model is properly configured and connected to the "*wecSimInputFile.m*" to initiate the WEC-Sim simulation.
- Define the power calculation equations: the calculation of power generation for each round of simulation need to be manually coded. This is realized by defining the equations that obtain power generation for one wave case in "$userDefinedFunctions.m$" file, and defining the codes for collecting the power generation for all the wave cases and output a power matrix in "$userDefinedFunctionsMCR$" file. Here, MCR stands for Multiple-case-running.
- Starting simulation: for a wave series to be calculated, $wecSimMCR$ command is to be used instead of $wecSim$.

3.3.2. Configuring and results

After running BEMIO, the boundary element method output are plotted as in figure 3.14 to figure 3.18.

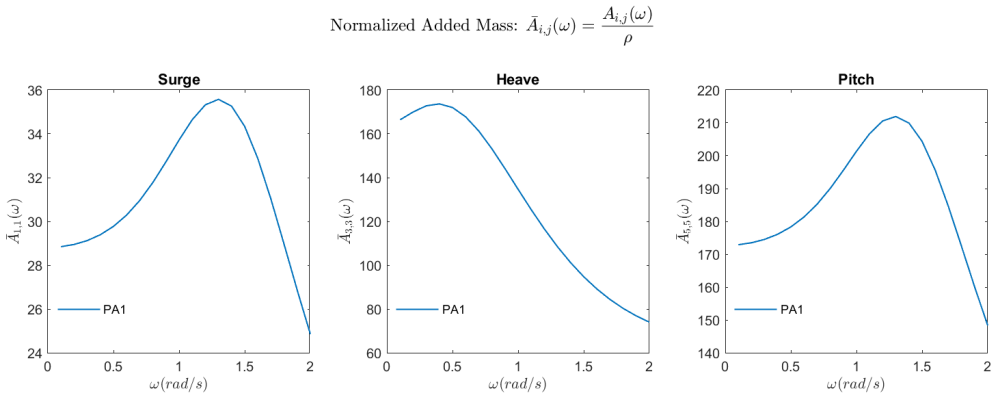

Notes:
• $\bar{A}_{i,j}(\omega)$ should tend towards a constant, A_∞, within the specified ω range.
• Only $\bar{A}_{i,j}(\omega)$ for the surge, heave, and pitch DOFs are plotted here. If another DOF is significant to the system, that $\bar{A}_{i,j}(\omega)$ should also be plotted and verified before proceeding.

Figure 3.14: Added mass plot

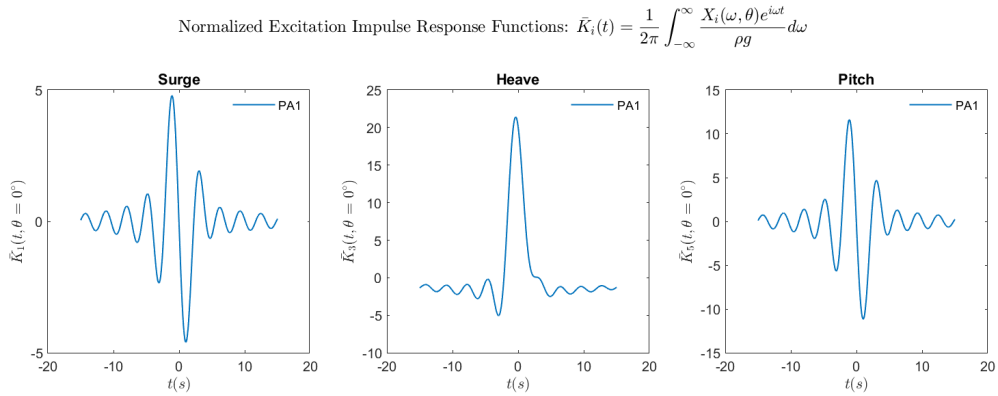

Notes:
• The IRF should tend towards zero within the specified timeframe. If it does not, attempt to correct this by adjusting the ω and t range and/or step size used in the IRF calculation.
• Only the IRFs for the first wave heading, surge, heave, and pitch DOFs are plotted here. If another wave heading or DOF is significant to the system, that IRF should also be plotted and verified before proceeding.

Figure 3.15: Excitation IRF plot

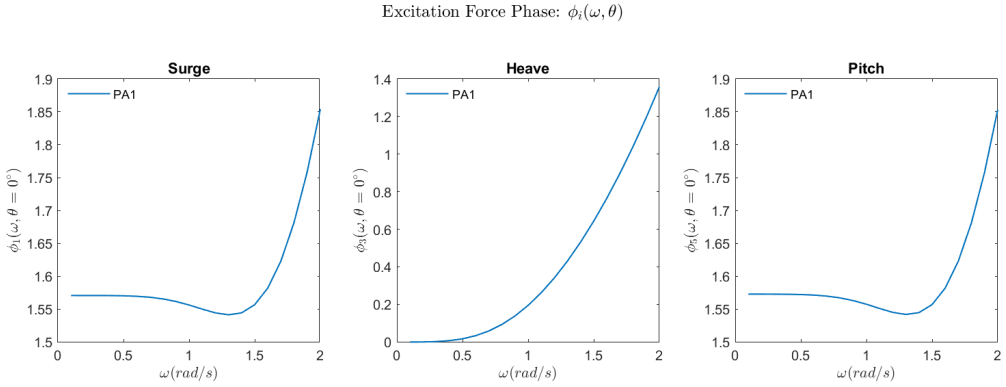

Figure 3.16: Excitation phase plot

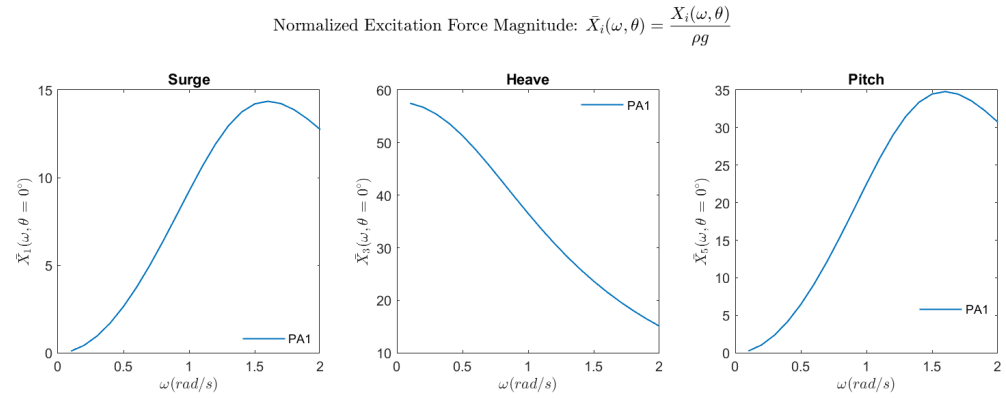

Figure 3.17: Excitation magnitude plot

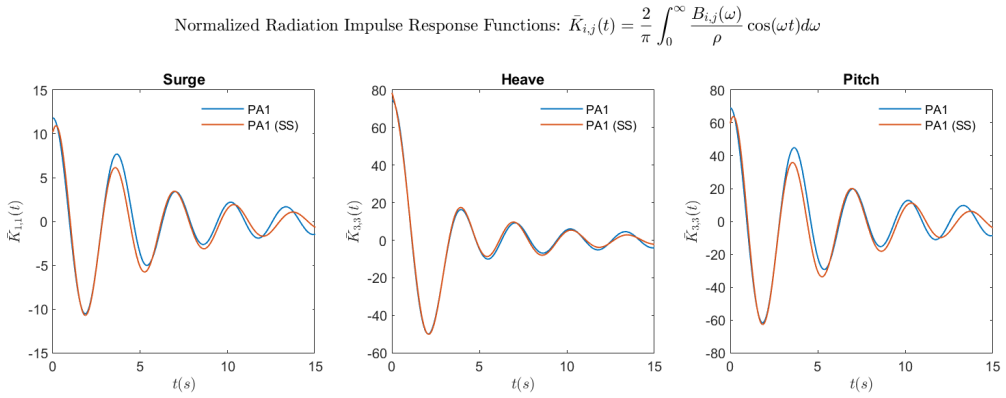

Figure 3.18: Radiation IRF plot

In WEC-Sim, when a constraint and a PTO are connected directly, the software will not be able to solve the forcing and motion between the two blocks. To solve this issue, an entity with a negligibly small mass is added to the model between the PTO and the constraint.

Two constraints are configured in the model. The first one is a translational constraint that ensures that the simulation focus only on vertical displacement and motion to align with the objective of this study. The second constraint is a floating constraint implemented to simulate the proper floating behaviour of the PA, which in reality a mooring line serves the same purpose as maintaining the PA's stability and floating.

The final Simulink model setting is shown in figure 3.19.

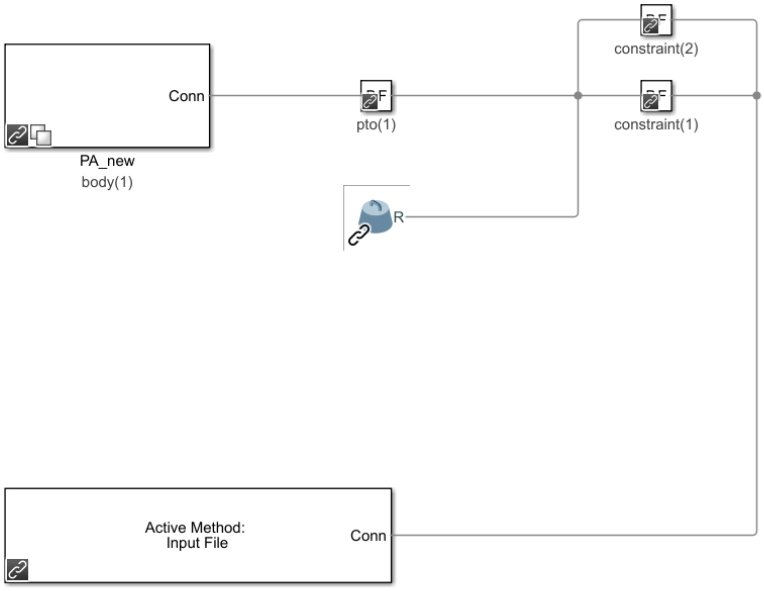

Figure 3.19: Simulink model

A manual-produced power matrix using the same series of JONSWAP waves is presented in figure 3.20.

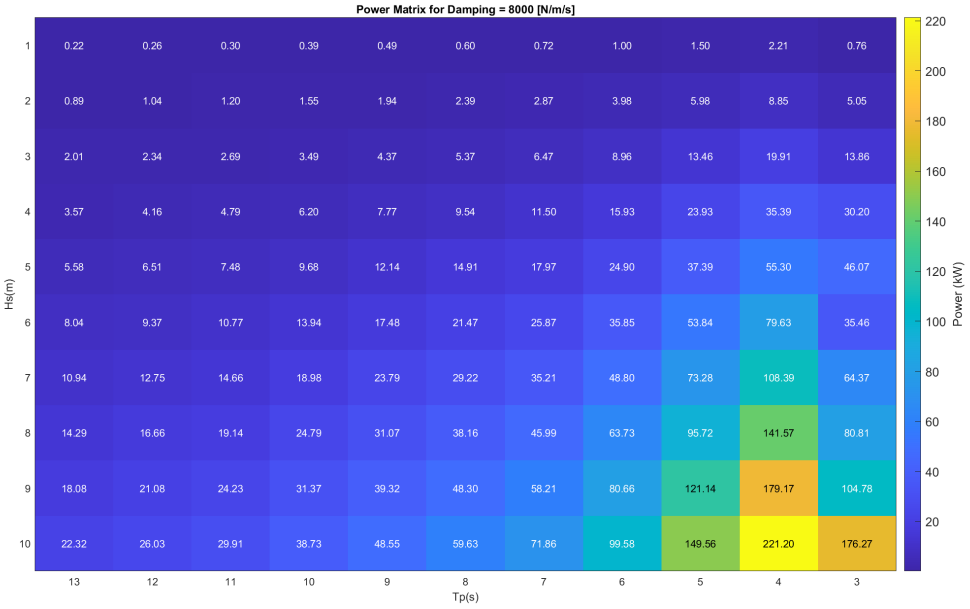

Figure 3.20: Manual calculated power matrix

The power matrix generated by simulation via WEC-Sim is presented in figure 3.21

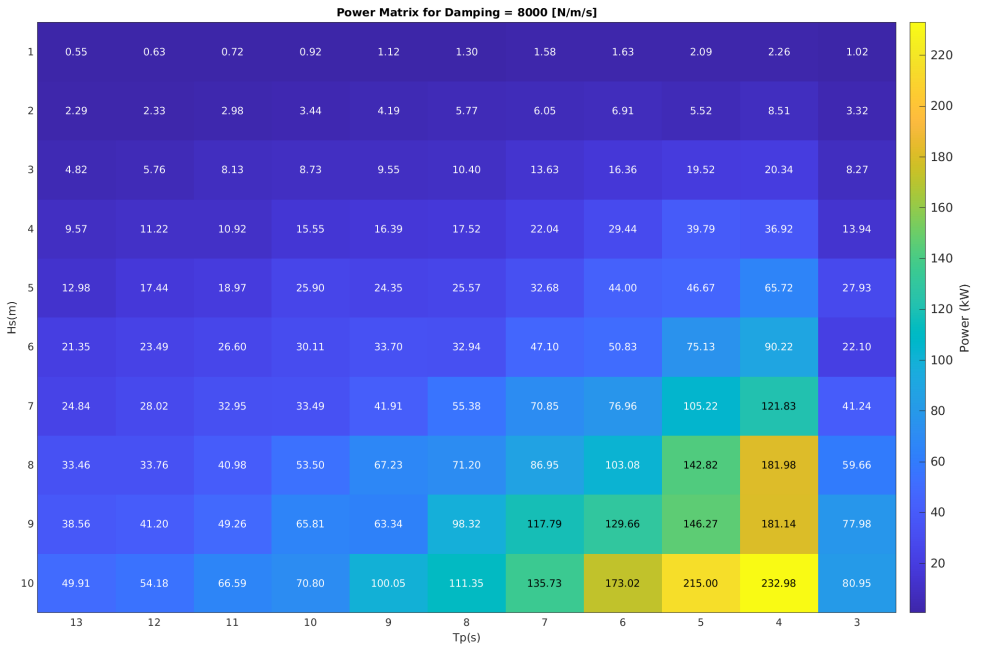

Figure 3.21: Power matrix obtained from simulation in WEC-Sim

3.3.3. Comments

Based on the two power matrices presented above, the following key points are given:

- The power matrix obtained by simulation does not show an exact uniform change in power absorption as the varying of the wave parameters, while the manually calculated one demonstrates an ideal and uniform increase in power as amplitude increases.
- Both power matrices show a peak power absorption at a wave period of 4 s, in accordance with the natural frequency of the PA model.
- Despite some difference in the extremely high power absorption value, which occurs at $T_p = 4$ s and $A = 10$ m, the overall values for each wave series exhibit minor deviation.

In conclusion, WEC-Sim simulation has been considered to be validated as a reliable tool for determining the power absorption of the PA model in this study.

4

Computational results in WEC-Sim

4.1. Determine the case to run for optimization

In this study, the spacing factor d will be introduced as a variable in optimization, expressing the distance between the WECs in each corner. As to show a variance from the layout configurations explored in existing literature, this study implements a scattered layout of 5 WECs, as shown in Figure 4.1 ($d = 4R$). 10 cases will be examined, with a range of d varies from $4r$ to $10r$, along with additional cases of $d = 12R$ and $d = 16R$. The long-distance spacing configurations are made to ensure that placing the WECs with a sufficient distance in between will result in the same energy absorption amount with placing 5 individual WECs. The overview of the WECs in simulation is shown in figure 4.3. Known from the result given by [25], this configuration allows more WECs to face the incident wave incoming direction or with a rather small angle, no matter in which direction the wave is coming from. Additionally, to show a comparison of this scattered layout, another configuration, where the WECs are not always facing the incoming wave direction, is set up as shown in figure 4.2. In this configuration, d is considered to be the spacing between 2 WECs in the neighbourhood.

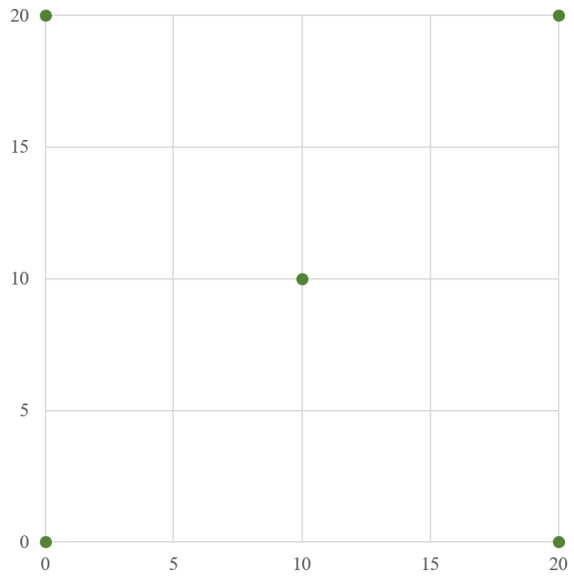

Figure 4.1: Layout 1 of 5 WECs

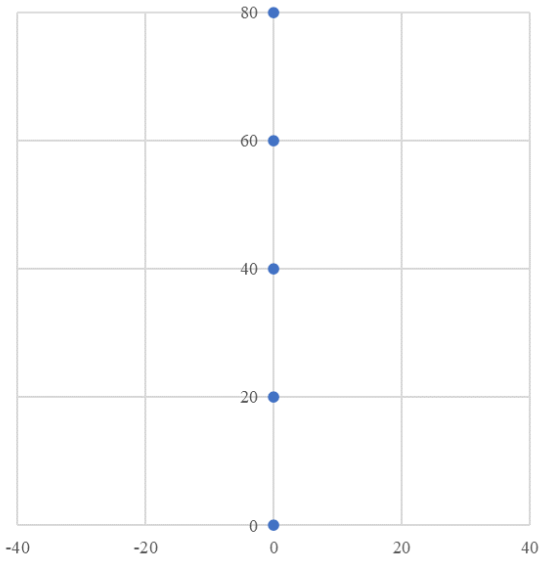

Figure 4.2: Layout 2 of 5 WECs

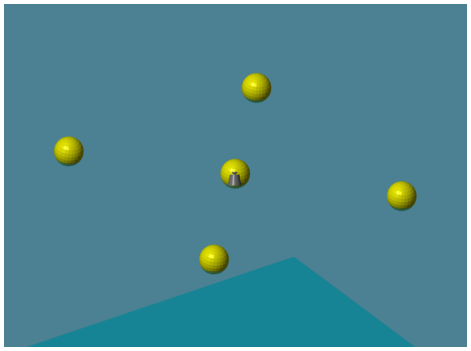

Figure 4.3: Layout overview in simulation

In the evaluation of the power extraction ability of a WEC array, the index $q-factor$ is commonly used[52], which is a ratio between the total power output of the entire WEC group considering their interaction and the total power output that should be expected by placing the same number of WECs individually. The expression is written as:

$$q = \frac{P_{total}}{N \cdot P_0} \tag{4.1}$$

where P_{total} is the total power output of the WEC array, P_0 is the power output for one point absorber.

The total power output at a certain site is estimated by overlaying the wave occurrence probability diagram (also referred to as the scattered diagram) with the power matrix. The wave scatter diagram over 15 years in the Babolsar area, Caspian Sea[36.75° N, 52.63° E] [34] is shown in figure 4.4.

H_s(m) \ T_p(s)	% of time	2	3	4	5	6	7	8	Sum
	0.5	0.0296	0.2567	0.1806	0.0645	0.0047	0.0002	0.0000	0.5361
	1	0.0000	0.0180	0.1065	0.1210	0.0532	0.0055	0.0000	0.3042
	1.5	0.0000	0.0000	0.0028	0.0193	0.0292	0.0135	0.0007	0.0655
	2	0.0000	0.0000	0.0000	0.0012	0.0074	0.0057	0.0011	0.0154
	2.5	0.0000	0.0000	0.0000	0.0000	0.0007	0.0016	0.0006	0.0030
	3	0.0000	0.0000	0.0000	0.0000	0.0000	0.0007	0.0007	0.0015
	Sum	0.0296	0.2746	0.2899	0.2059	0.0952	0.0272	0.0031	1.0000

Figure 4.4: Wave scatter diagram in Babolsar site, Caspian Sea

To match the range of the wave in Babolsar, T_p is set as 2 to 8 s and H_s is set as 0.5 to 3 m in the simulation.

4.2. Results

The calculations have been done with DelftBlue[53]. The power matrix for one WEC, the power matrices showing the best production case and the worst production case are shown here, while all the power matrices are presented in the appendix:

4.2.1. Power matrices and annual power output diagram

Configuration 1

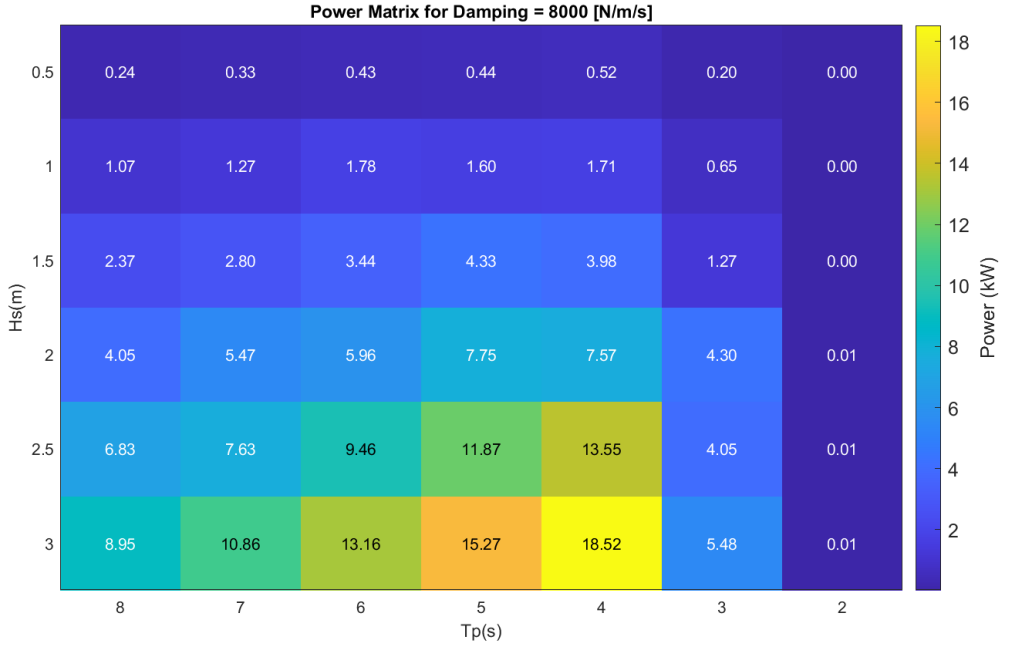

Figure 4.5: Power matrix, 1 WEC, $d_{PTO} = 8KN/-s/m$

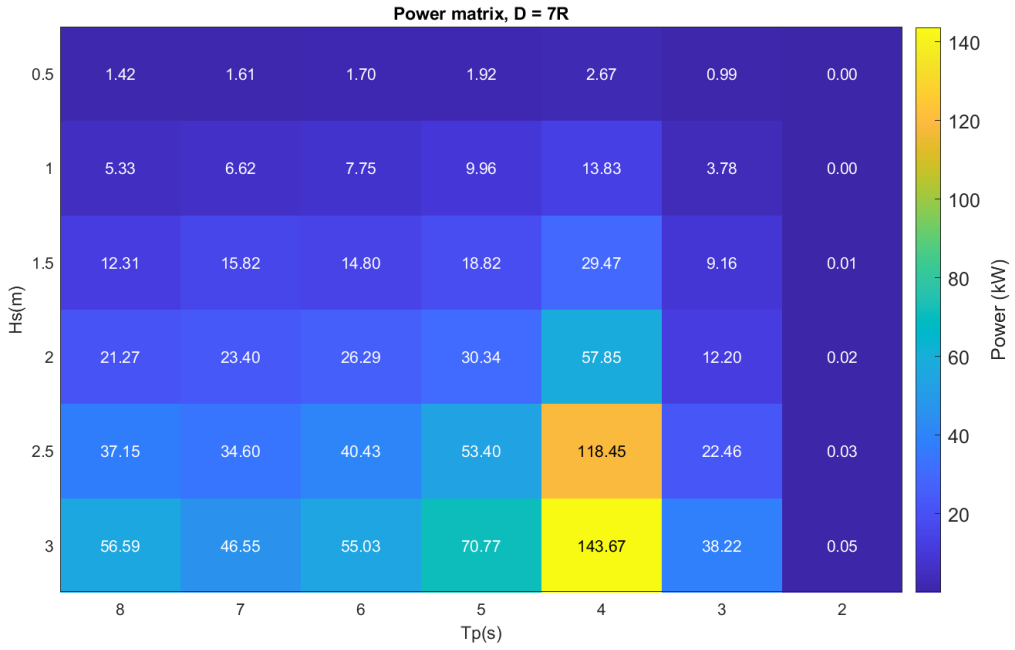

Figure 4.6: Power matrix, 5 WECs, best case, d = 7R, $d_{PTO} = 8KN/-s/m$

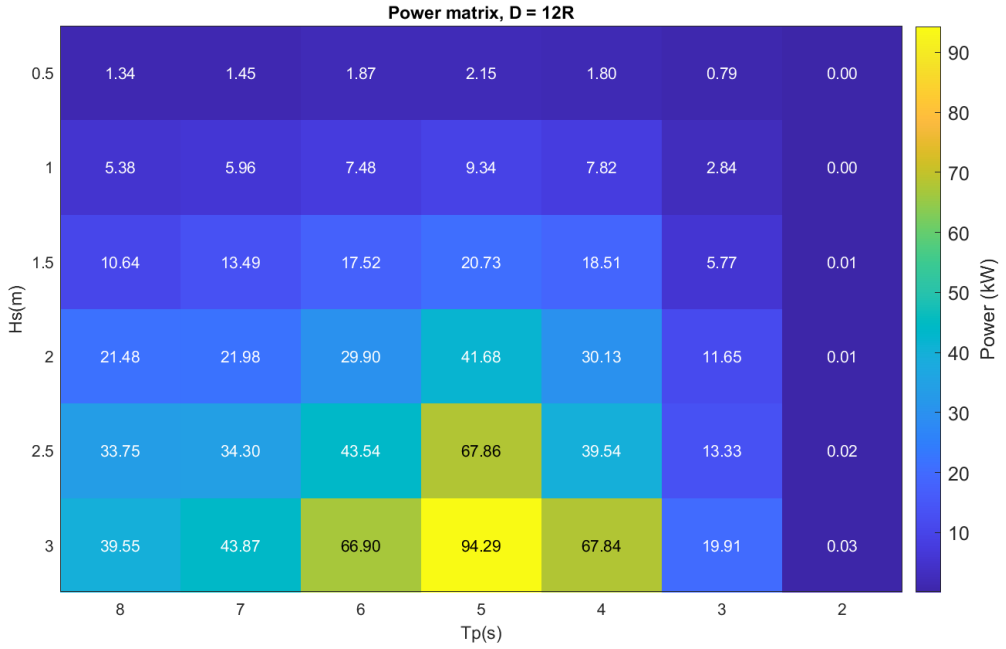

Figure 4.7: Power matrix, 5 WECs, worst case, d = 12R, $d_{PTO} = 8KN/-s/m$

After combining the power matrix with the wave occurrence diagram, the annual total power output are presented in figure 7.22 to figure 7.26 here respectively:

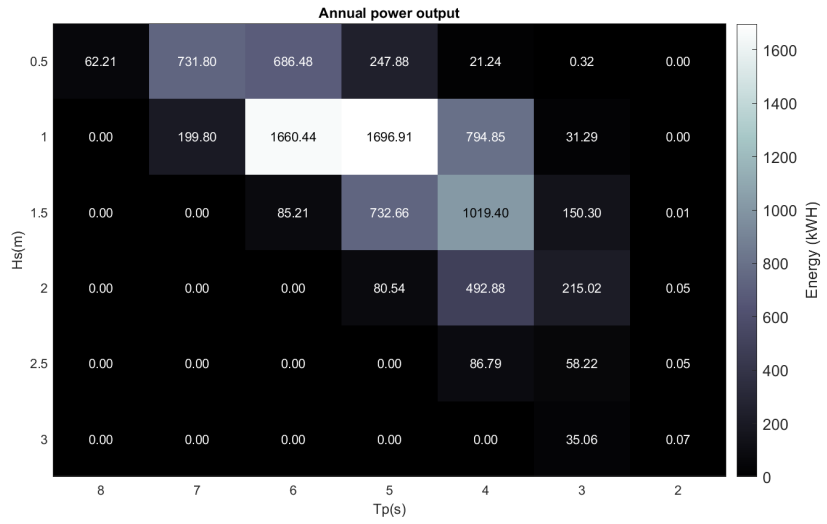

Figure 4.8: Annual power output, 1 WEC

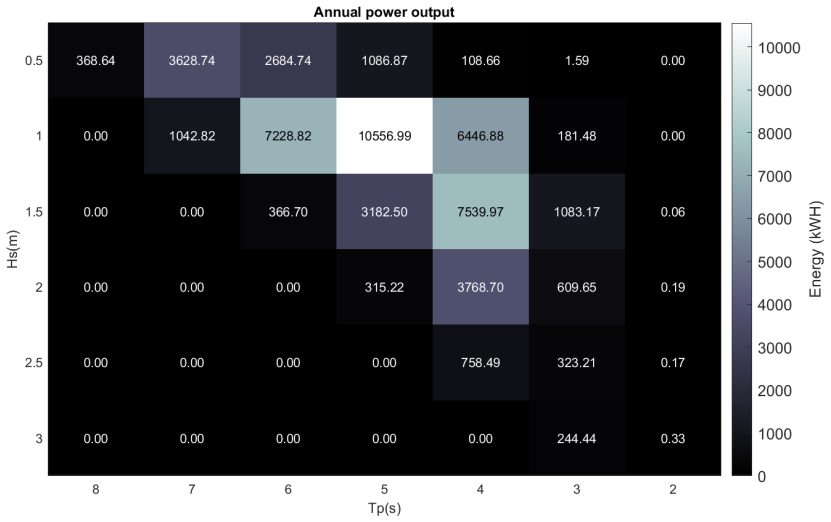

Figure 4.9: Annual power output, 5 WECs, best case, d = 7R

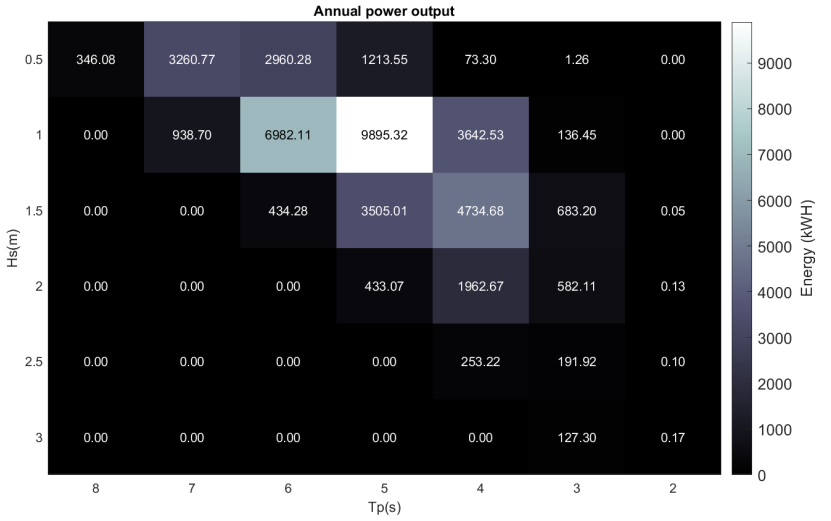

Figure 4.10: Annual power output, 5 WECs, worst case, d = 12R

Configuration 2

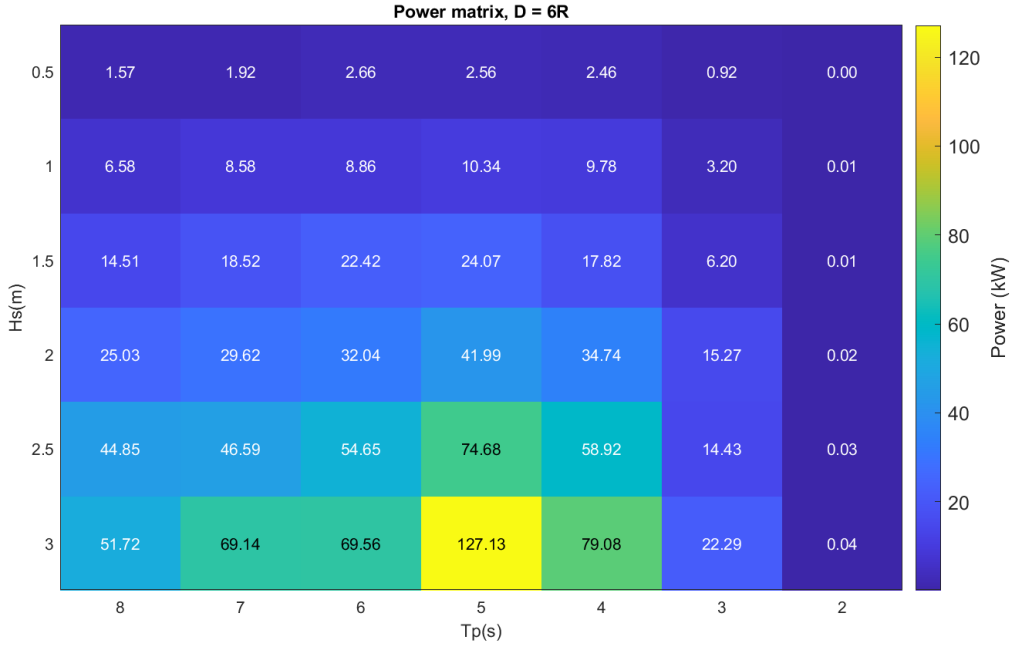

Figure 4.11: Power matrix, 5 WECs, best case, d = 6R, $d_{PTO} = 8KN/-s/m$

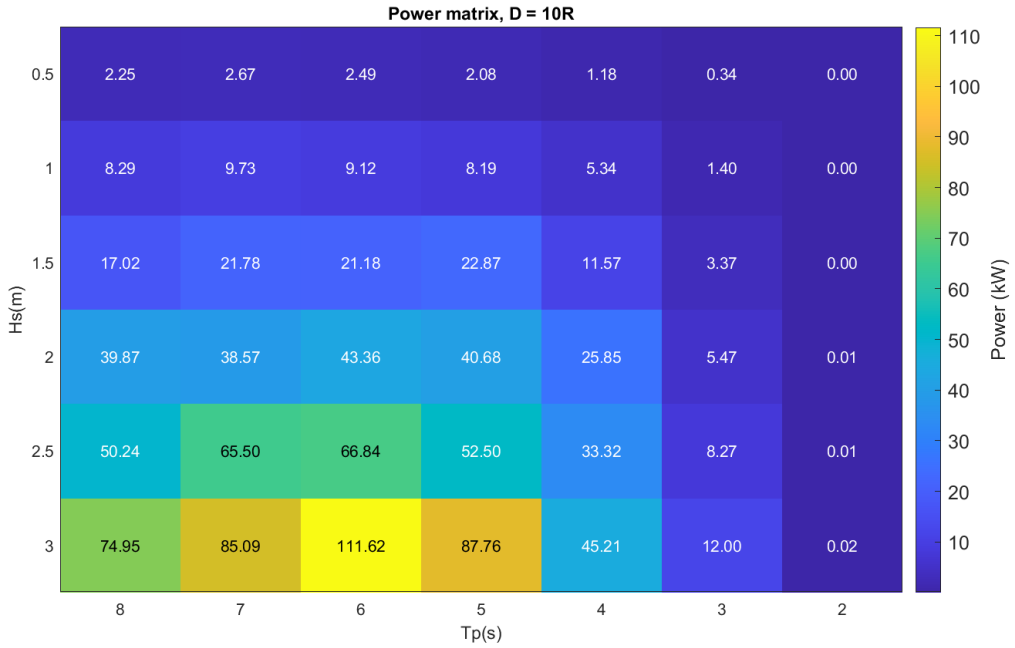

Figure 4.12: Power matrix, 5 WECs, worst case, d = 10R, $d_{PTO} = 8KN/-s/m$

The annual total power output are presented in figure 7.31 to figure 7.35 here respectively:

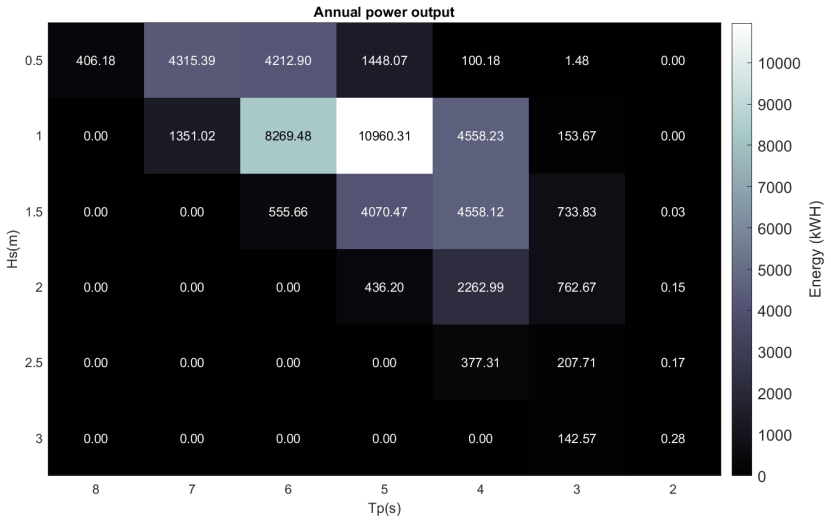

Figure 4.13: Annual power output, 5 WECs, best case, d = 6R

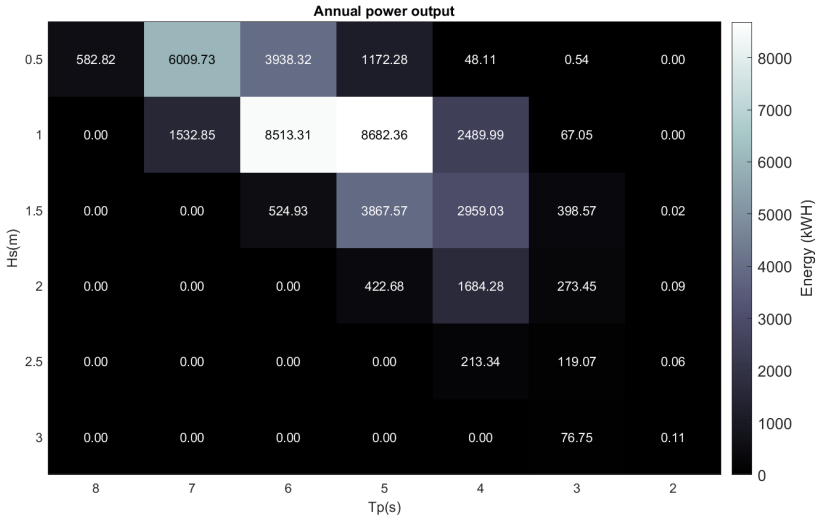

Figure 4.14: Annual power output, 5 WECs, worst case, d = 10R

4.2.2. Q-factor

Accordingly, the q-factor for the cases are presented in table 4.1:

Table 4.1: Summary of q-factor

d	16 R	12 R	10 R	9 R	8 R	7 R	6 R	5 R	4 R
Configuration 1	0.9992	0.9320	1.0262	1.0638	1.0699	1.1338	1.1113	1.0105	0.9773
Configuration 2	0.9987	0.9901	0.9588	1.0550	1.0942	1.0942	1.0976	1.1051	1.0627

4.2.3. Comment

From the result, it is generally observed that configuration 1 exhibits a higher q-factor. To provide a more detailed explanation to this, a visualization of the wave and geometries is plotted in ParaView as in figure 4.15 and 4.16, which highlights that the simulated dominant wave is coming from the direction with a noticeable wave angle. In this wave field, more WECs are likely to experience the incident waves perpendicularly to the wave incoming direction in configuration 1 so that to have more power produced, which shows similarity to the finding of Giassi et al.[25].

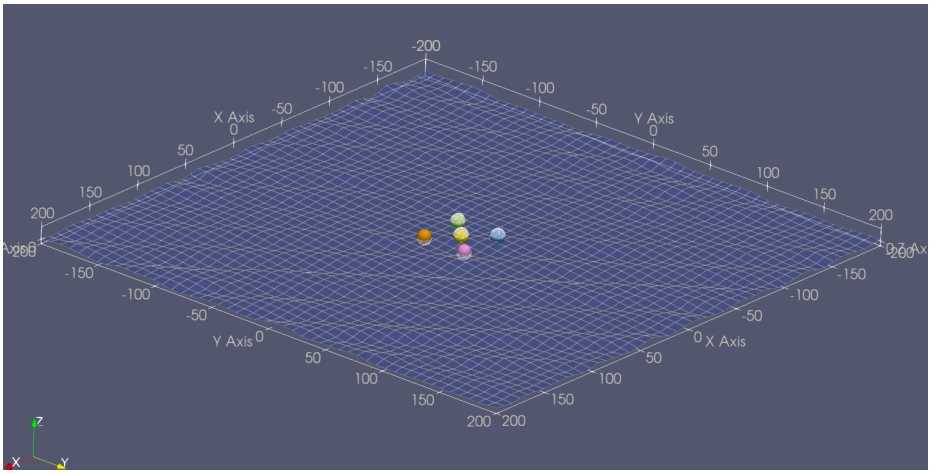

Figure 4.15: Visualization of wave field and geometry in ParaView, configuration 1

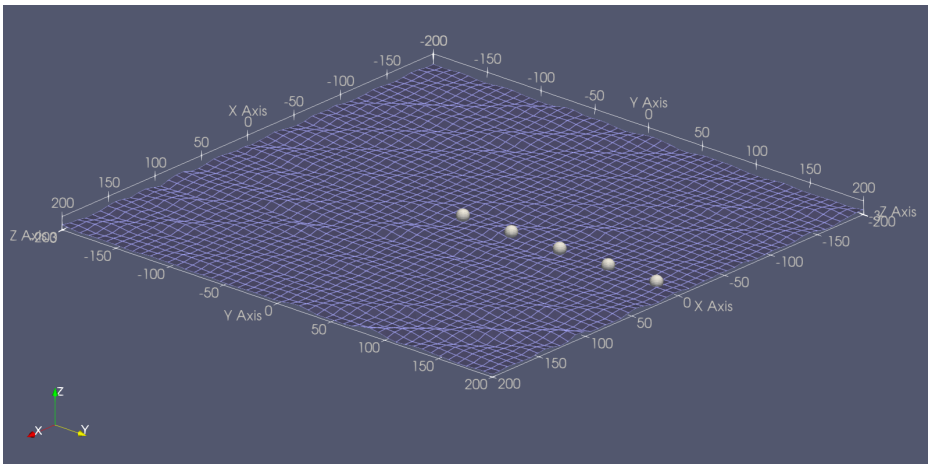

Figure 4.16: Visualization of wave field and geometry in ParaView, configuration 2

It is reasonable to observe an increasing q-factor when the WECs are placed closer to each other, ranging from $D = 16R$ to $D = 6R$. This is because, within a certain range, the proximity of the WECs leads to more hydrodynamic interactions, resulting in creating additional wave power. However, there is a limit to how closely the WECs can be spaced. When the spacing becomes too small, the incoming waves may be diffracted by the first WEC that encounters the wave. As a result, the wave energy reaching the WECs located behind the front one may be significantly reduced or even completely blocked. Consequently, there would be little to no energy available for the WECs positioned in the shadowed region, leading to a decrease in the overall power extraction and a decrease in the q-factor. Apart from that, when the WECs are placed too far away from each other, for example, when $D = 16R$, the q-factor tend to be close to one. The reason for this is the impacts from the other devices reduces when the distance get further. And when they are

placed sufficiently far from each other, the result will be the same as placing same number of isolated WECs.

5

Economical model

5.1. Model establishment

In this chapter, an economical model is developed intend to compute the CapEx, OpEx, serving the purpose of obtaining LCOE, which is commonly used as an assessment of a project's profitability. This model takes various input into account, with d as a variable in different cases.

5.1.1. Capital expense

CapEx(Capital Expenditure) is known as funds allocated for the purchase of devices. For WEC arrays, it may also include the CapEx for the electric system, installation and commissioning. CapEx for the device includes the expense on the buoy itself, the cost on PTO system, and some other materials. Moreover, CapEx on the electrical system basically includes the cost on the cables installed within the WEC devices farm and the cables connecting the WEC array to the onshore energy station. The length for inter-WEC cables is expressed as $l_{incable}$ while the length for the cable connected to the power station is expressed as$l_{excable}$ In the case of Babolsar site, $l_{excable}$ is 4.3 km[34]. If we assign C as a representation for cost, the cost for cables per meter can be expressed as $C_{incable}$ and $C_{excable}$ $[EUR/m]$, respectively. In addition, the CapEx for commissioning and decommissioning should also be calculated. The days spent on installation is noted as D. A barge–crane[54] proposed by M. A. Chatzigiannakou in 2018 is considered, which enables 5 devices associated with cables to be installed during a day. And total cost for hiring installation vessels $C_{installation}$ is summed up as 158706 EUR/day. The cost of decommissioning is assumed to be the same as commissioning here.

To summarize, the CapEx for the whole project can be expressed as:

$$\text{CapEx}_{WECs} = N \cdot C_{PA} + C_{incable} \cdot l_{incable} + C_{excable} \cdot l_{excable} + 2 \cdot C_{installation} \tag{5.1}$$

where N is the number of devices.

5.1.2. Operational expense

OpEx refers to the operational cost of the project, measured in [EUR/year]. It primarily involves the expenses on the daily operation and maintenance activities. A constant failure rate and a constant OpEx value are assumed for the devices. It should be noted that in reality, the OpEx tends to vary over time, especially during the start and final periods of a WEC's commissioning years[55]. However, this is not the point to be focused on in this study.

By noting a yearly repair cost as C_{repair}, and f as the failure rate of the WEC devices, the formula of computing OpEx can be written as[56]:

$$\text{OpEx} = f \cdot N \cdot (C_{repair} + 2 \cdot \frac{C_{installation}}{N}) \tag{5.2}$$

5.1.3. Levelized cost of energy

The Levelized Cost of Electricity (LCOE) known as the final objective in evaluating the profitability of the economic model, gives the average minimum price at which electricity must be sold to reach a break-even point over the entire commissioning lifespan of the project. Concerning parameters are: $E_{annual}(y)$ as annual power production at operating year y, r discount rate, Y as years of operation, as well as the aforementioned CapEx and OpEx. The value of LCOE is computed by equation5.3 [56]:

$$\mathrm{LCOE} = \frac{\mathrm{CapEx} + \sum_{y=1}^{Y} \frac{\mathrm{OpEx}}{(1+r)^y}}{\sum_{y=1}^{Y} \frac{\mathrm{E_{annual}}}{(1+r)^y}} \tag{5.3}$$

To simplify the model, the discount rate is also assumed to be constant over time.

5.2. Parameter input and results

The parameters that are taken into account for the model are summarized in table5.1. Note that at the same D, the length of the inner cables is assumed to be the same for configurations 1 and 2, which is calculated as in configuration 1, 4 cables connecting the WECs in the corner to the WEC in the centre.

Table 5.1: Summary of parameters in the economical model

Parameters	Unit	Value
C_{PA}	EUR/kg	4
N	-	5
$C_{incable}$	EUR/m	40
$C_{excable}$	EUR/m	75
$l_{incable}$	m	$2 \cdot \frac{1}{2}\sqrt{d^2+d^2}$
$l_{excable}$	m	4300
$C_{installation}$	EUR/day	158706
D	-	1
f	$/year$	0.25
C_{repair}	EUR	10000
r	%	8
Y	$year$	20

The results for economical model calculation are presented in table 5.2 and table 5.3.

Table 5.2: Summary of economical model results, configuration 1

d	16 R	12 R	10 R	9 R	8 R	7 R	6 R	5 R	4 R
E_{annual}[MWH]	9.077	8.471	9.328	9.669	9.725	10.31	10.10	9.185	8.882
CapEx[MEUR]	2.235	2.233	2.232	2.231	2.231	2.230	2.229	2.229	2.228
LCOE[kEUR/MWH]	35.20	37.69	34.22	33.00	32.81	30.95	31.57	34.72	35.89

Table 5.3: Summary of economical model results, configuration 2

d	16R	12R	10R	9R	8R	7R	6R	5R	4R
E_{annual}[MWH]	9.047	8.999	8.716	9.590	9.946	9.945	9.977	10.04	9.659
CapEx[MEUR]	2.235	2.233	2.232	2.231	2.231	2.230	2.229	2.229	2.228
LCOE[kEUR/MWH]	35.32	35.47	36.62	33.28	32.08	32.07	31.97	31.74	33.01

6

Multiple-objective optimization

In this chapter, the two indexes, q-factor and LCOE, which have been discussed before will be optimized to find an optimal solution for the variable spacing factor d. This will be done via utilizing NSGA-II (Nondominated sorting genetic algorithm), a multi-objective evolutionary algorithm[57] that solves a problem involving multiple goals effectively.

NSGA-II is an algorithm inspired by the natural selection theory proposed by Darwin, and the basic idea is in employing an evolutionary approach to guide the population towards the most favourable solution. It solves the disadvantages including nonelitism and computational complexity from the classic evolutionary algorithm, by employing a nondominated sorting approach. The sorting and converging speed are significantly accelerated by using elitism, which allows for keeping an unchanged best solution from the previous iteration for the current one[58]. The goal of this algorithm is to efficiently find the Pareto front, which is a curve that consists of the points implying a set of best solutions in a multi-objective problem. The solution set of this front is formed by all the non-dominated solutions, namely the solutions that are not dominated by other solutions[59].

6.1. Procedures followed

The algorithm is implemented by following these steps:

- Initialization of population: A population, also referred to as individuals, is initialized usually based on the range of the problem.
- Evaluation: Performing an evaluation for each individual in the population by obtaining the solutions from 2 objective functions set for q-factor and LCOE.
- Nondominated-sorting: Non-dominated sorting is applied to sort the individuals. Completely nondominated individuals are assigned to the first front set, and the population dominated by the first front individuals will be assigned to the second front. This goes on to classify all the individuals into different fronts based on their dominance relationship and dominance rank. This is done by comparing the values given by the individuals with the same objective.
- Crowding Distance Calculation: Crowding distance is a measurement of the distance between each individual and their neighbourhood. Computing the crowding distance is basically finding the euclidean distance between two individuals. And a large crowding distance indicates a population with more diversity.
- Selection: Selecting individuals for the next generation after they are being sorted and crowding distances are calculated. The nondomination front and crowding distance are compared by utilizing a crowd-comparison-operator.
- Offspring producing: Offspring of the current population are created by using genetic operators, including crossover operator and mutation operator. Now the new created generation forms the population together with the current generation.

- Repeat and output: The newly formed population is sorted again by nondomination method. As the population now also includes the best individuals from the first generation, elitism is guaranteed, which helps to maintain a stability of the solution. In this way, the algorithm will give the final population as the optimal solution and forms the Pareto-front after it ends. The Pareto-front graph represents the best solutions for q-factor and LCOE, also, a trade off between the two factors.

Figure 6.1 shows a visualization of the procedure that the algorithm follows.

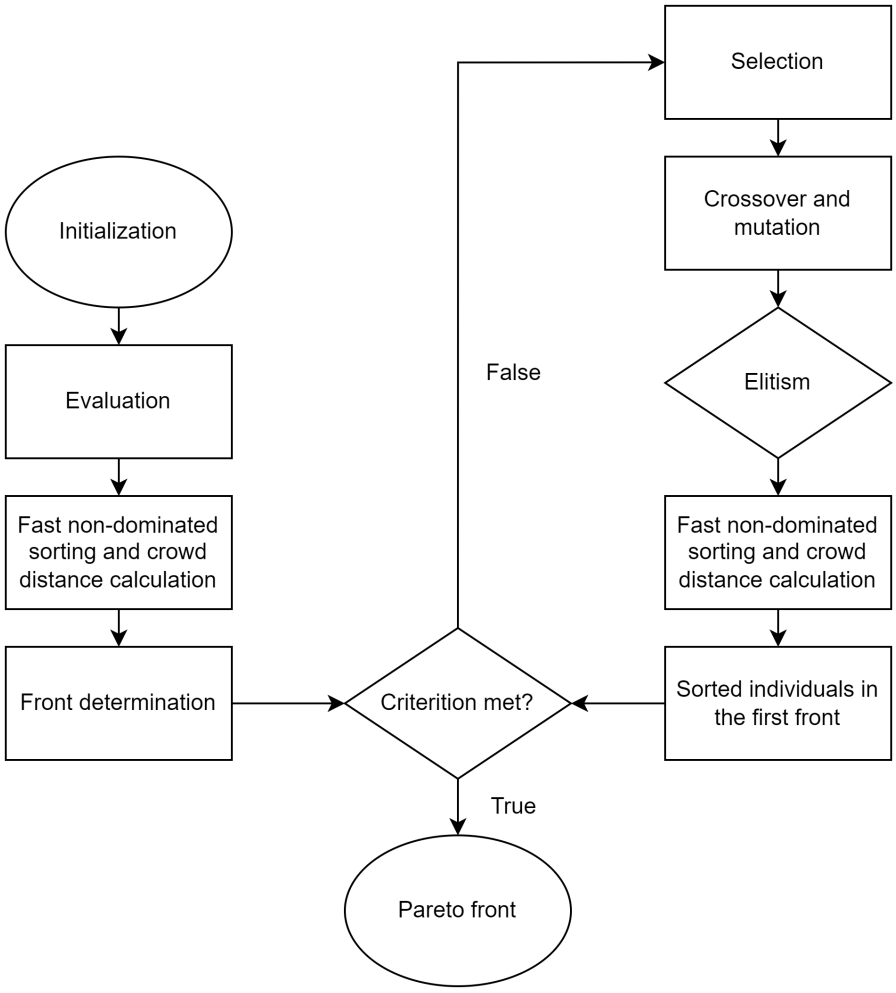

Figure 6.1: NSGA-II process

6.2. Algorithm implementing

To achieve the evaluation in the aforementioned procedure, the objective function for both index based on the variable d should be added to the algorithm[60]. Based on the cases for various values of d, a function of q-factor can be established by interpolation and curve fitting. Given the data obtained from the previous chapter, the function of q-factor in a relation with d can be written as:

$$\begin{aligned} q(d) = &-1.044 \cdot \sin\left(0.07384 \cdot d + 0.9314\right) - 0.08048 \cdot \sin(0.6359 \cdot d - 2.734) \\ &- 0.0309 \cdot \sin(1.995 \cdot d - 11.43), \text{ for configuration 1} \end{aligned} \tag{6.1}$$

$$q(d) = 1.544 \cdot sin(0.1666 \cdot d - 0.1259) + 0.555 \cdot sin(0.3188 \cdot d + 1.367), \text{ for configuration 2} \tag{6.2}$$

It is noted that, the optimization algorithm is always searching for a minimum solution of the objective function. Therefore, in order to get a maximum q-factor, the function should be multiplied by -1 before being implemented into the algorithm.

Same method can be used to obtain the function for LCOE. Also, the LCOE can be expressed as a function using q-factor as the variable in the algorithm by combining equation5.3 and 6.3.

$$E_{annual} = q(d) \cdot N \cdot P_0 \cdot \frac{365 \cdot 24}{1000} \tag{6.3}$$

6.3. Result

In the execution of the algorithm, an initial population of 40 individuals is created. Here, an individual means a random generation of the variable D within the range of 4 to 16 r. Consequently, the algorithm proceeds through 40 generations and gets a converged result. The final Pareto-front plot is shown in figure6.2, from which an optimal solution for q-factor and LCOE can be concluded. The solution set occurs in configuration 1 at $d = 6.63R$, with q-factor as 1.142 and LCOE as 30.7 kEUR/MWH. In this way, the annual energy generation of this WEC array will be 10.379 MWH.

Configuration 1

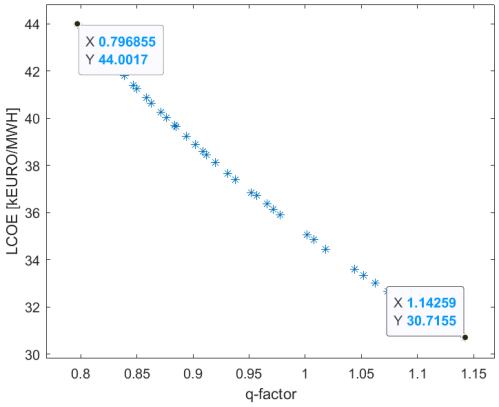

Figure 6.2: Pareto-front obtained by 40 generations

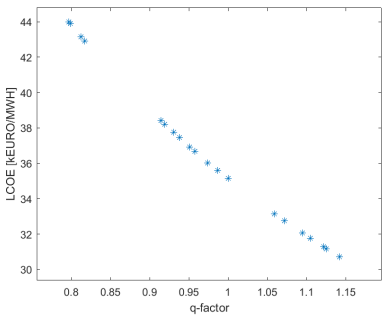

Figure 6.3: Generation = 5

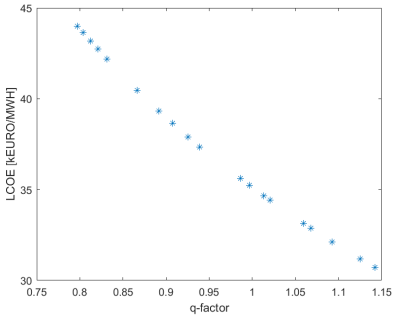

Figure 6.4: Generation = 20

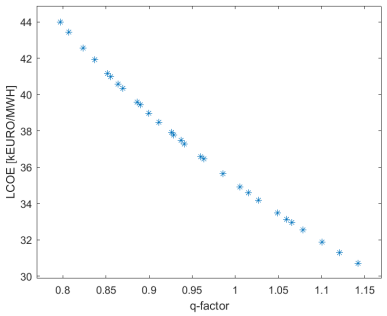

Figure 6.5: Generation = 30

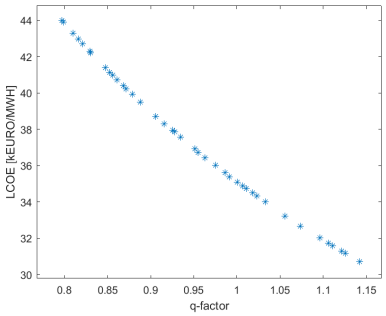

Figure 6.6: Generation = 50

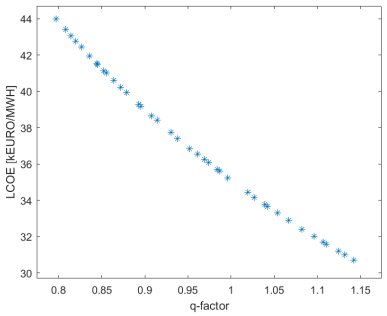

Figure 6.7: Generation = 80

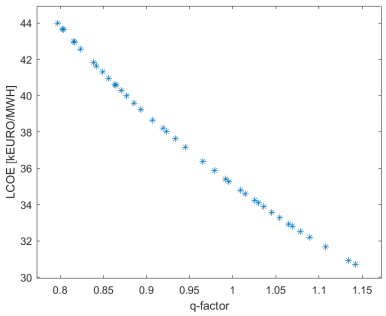

Figure 6.8: Generation = 100

Configuration 2

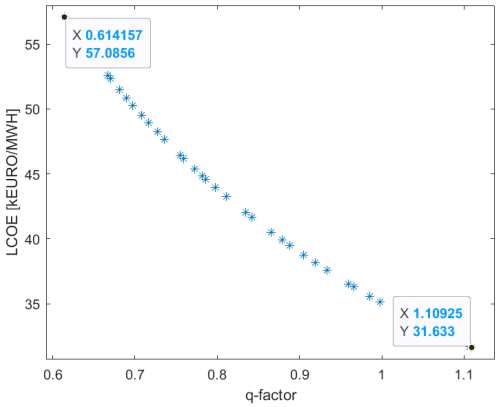

Figure 6.9: Pareto-front obtained by 40 generations

The parameters input and final results are summarized in table6.1 and table6.2:

Table 6.1: Summary of parameters and results in optimization, configuration 1

Population	-	40
Generation	-	40
q-factor	-	1.142
LCOE	kEUR/MWH	30.7
E_{annual}	MWH	10.379
d	m	33.15 (6.63r)

Table 6.2: Summary of parameters and results in optimization, configuration 2

Population	-	40
Generation	-	40
q-factor	-	1.109
LCOE	kEUR/MWH	31.6
E_{annual}	MWH	10.080
d	m	28.43

7

Conclusions and future work

7.1. Conclusions

By reviewing the research objectives proposed in the opening of the study, which are:

- Verifying hydrodynamic analysis in NEMOH associated with WEC-Sim on test model, and finalized the WEC model used in optimization
- Performing hydrodynamic analysis to find the wave power at the selected site
- Developing mathematical formulations for the optimization problems and forming the objective functions
- Optimization considering power production and economical goal by NSGA-II (Multi-objective evolutionary algorithm)

the conclusion can be drawn accordingly. In the assessment of capability comparison between NEMOH 2.8 and NEMOH 3.0, NEMOH 2.8 showed better efficiency when faced with a limited number of frequencies. However, the advantages of NEMOH 3.0, which are giving direct calculation of RAO and being more easily enabling multiple wave direction calculation, outweigh this disadvantage. Furthermore, the RAO results in NEMOH 3.0 was also verified through a manual calculation, which facilitated the manual power matrix production in the next research step.

Obstacles were encountered while first running WEC-Sim by using the hydrodynamic results from NEMOH 3.0. Nonetheless, the reason was then found by identifying the modifications in NEMOH 3.0's source codes in comparison with NEMOH 2.8. The problem of the inconsistency between NEMOH 3.0 and WEC-Sim was sorted successfully, and this allows for performing a multi-directional irregular wave simulation in WEC-Sim's BEMIO module with hydrodynamic data obtained from NEMOH 3.0.

Given the verified methodology, a point absorber model and 2 configurations of WEC array were established and finalized with the hydrodynamic analysis. By setting up irregular wave cases that matches the Babolsar site in Caspian Sea, a series of power matrices was acquired, with a variable of the spacing factor d. The annual power production was calculated by overlaying the wave scattering diagram with the power matrices. The assessment index for power producing ability for a WEC array, q-factor was obtained consequently. The results showed that when the WECs are placing sufficiently far from each other, the whole array's efficiency acts the same as placing the same number of isolated WECs. When the WECs are placed closer, the q-factor can be above 1. However, placing the WECs too close may be destructive to the total efficiency of the array, and the q-factor even can be less than 1.

Finally, an economical model was developed to assess the LCOE for the WEC array. As two final objectives to be optimized, q-factor and LCOE were given by two objective functions in order to go through the algorithm. By executing the NSGA-II multi-objective algorithm, a converged Pareto-front was found at the 40th generation with an initial population of 40. The optimal results were

found as: q-factor being 1.142 and LCOE being 30.7 kEUR/MWH with spacing index $d = 33.15m$. The annual power production was going to be 10.379 MWH.

7.2. Future work

In this study, layouts for a 5-point WEC array were selected, while focusing on the optimization of the spacing between the WECs primarily, the size of the point absorber was predetermined based on a review of relevant literature, which indicates a smaller and more compact WEC design holds greater promise for operating efficiently in low-energy sea conditions. Also, the draft-radius ratio was also pre-decided based on findings in the literature review.

These initial assumptions and decisions indicate that there is room for further improvement. Future studies could explore the optimization of WEC size in combination with layout optimization by conducting multi-objective optimization, for example, finding the optimal radius of the point absorber in the array, which leads to an interesting and profitable topic in low-energy seas.

Additionally, during the simulation in WEC-Sim, the mooring system of the WEC was omitted in modelling, and instead, a floating constraint was used to simulate the scenario. Although the power matrix results turn out to give a high degree of closeness to the ideal values calculated by analytical methods and mooring lines should not have a significant impact on hydrodynamic performance of the WECs, it is important to acknowledge that inaccuracies may still exist since the model does not fully represent the conditions in reality.

In future studies, it would be an improvement to use a mooring line configuration while modelling the WECs, which represent real-world scenarios better. The credibility and reliability of the simulation results can be further enhanced in this way.

Last but not least, the approach for optimization separates the hydrodynamic analysis part and the algorithm execution part. This requires an approximate equation to be established by using the data obtained in the hydrodynamic calculation.

In future studies, the hydrodynamic calculation process could be incorporated into each iteration of the algorithm to achieve a more consistent methodology and a better approximation to reality.

Appendix

7.2.1. Plotting results in NEMOH 2.8

```
tic
CA = readmatrix("...");
CM = readmatrix("...");
[numRows,numCols] = size(CA);
omega = CA(7:7:numRows , 1);
A = [0.1];
w = vertcat(A,omega);

    % CA damping
Ca_11 = CA(1:7:numRows , 1); % surge
Ca_22 = CA(2:7:numRows , 2); % sway
Ca_33 = CA(3:7:numRows , 3); % heave
Ca_44 = CA(4:7:numRows , 4); % roll
Ca_55 = CA(5:7:numRows , 5); % pitch
Ca_66 = CA(6:7:numRows , 6); % yaw

    % CM added mass
Cm_11 = CM(1:7:numRows , 1); % surge
Cm_22 = CM(2:7:numRows , 2); % sway
Cm_33 = CM(3:7:numRows , 3); % heave
Cm_44 = CM(4:7:numRows , 4); % roll
Cm_55 = CM(5:7:numRows , 5); % pitch
Cm_66 = CM(6:7:numRows , 6); % yaw

    subplot(3,2,1);
hold on
plot(w , Ca_11,'–bs',w, Cm_11,'–gs',...
'MarkerSize',5,...
'MarkerEdgeColor','b',...
'MarkerFaceColor',[0.5,0.5,0.5]);
legend('Added mass coefficient 3.0','Damping coefficient 3.0','Damping coefficient 2.8','Added mass
coefficient 2.8','Location','southeast')
title('Surge')
xlabel('Wave frequency [rad/s]')
ylabel('Added Mass Coefficient for Surge Motion [-]')

    subplot(3,2,3);
hold on
plot(w , Ca_33,'–bs',w, Cm_33,'–gs',...
'MarkerSize',5,...
'MarkerEdgeColor','b',... 'MarkerFaceColor',[0.5,0.5,0.5]);
legend('Added mass coefficient 3.0','Damping coefficient 3.0','Damping coefficient 2.8','Added mass
coefficient 2.8','Location','southeast')
title('Heave')
xlabel('Wave frequency [rad/s]')
ylabel('Added Mass Coefficient for Heave Motion [-]')

    subplot(3,2,5);
hold on
plot(w , Ca_55,'–bs',w, Cm_55,'–gs',...
'MarkerSize',5,...
```

```
‘MarkerEdgeColor’,‘b’,...
‘MarkerFaceColor’,[0.5,0.5,0.5]);
legend(‘Added mass coefficient 3.0’,‘Damping coefficient 3.0’,‘Damping coefficient 2.8’,‘Added mass
coefficient 2.8’,‘Location’,‘southeast’)
title(‘Pitch’)
xlabel(‘Wave frequency [rad/s]’)
ylabel(‘Added Mass Coefficient for Pitch Motion [-]’)

    % Plot FN
Fe = readmatrix“...”);
[numRowsFe,numColsFe] = size(Fe);

    Fe_1 = Fe(1:numRowsFe , 2); % surge
Fe_3 = Fe(1:numRowsFe , 4); % heave
Fe_5 = Fe(1:numRowsFe , 6); % pitch

    subplot(3,2,2);
hold on
plot(w , Fe_1,‘–bs’,...
‘MarkerSize’,3,...
‘MarkerEdgeColor’,‘b’,...
‘MarkerFaceColor’,[0.5,0.5,0.5]);
title(‘Surge’)
legend(‘Excitation Force nemoh 2.8’,‘Excitation Force nemoh 3.0’,‘Location’,‘southeast’)
xlabel(‘Wave frequency [rad/s]’)
ylabel(‘Force Surge [N]’)

    subplot(3,2,4);
hold on
Fh = plot(w , Fe_3,‘–bs’,...
‘MarkerSize’,5,...
‘MarkerEdgeColor’,‘b’,...
‘MarkerFaceColor’,[0.5,0.5,0.5]);
Fh.Color = [Fh.Color 0.5];
title(‘Heave’)
legend(‘Excitation Force nemoh 2.8’,‘Excitation Force nemoh 3.0’,‘Location’,‘southeast’)
xlabel(‘Wave frequency [rad/s]’)
ylabel(‘Force Heave [N]’)

    subplot(3,2,6);
hold on
plot(w , Fe_5,‘–bs’,...
‘MarkerSize’,5,...
‘MarkerEdgeColor’,‘b’,...
‘MarkerFaceColor’,[0.5,0.5,0.5]);
title(‘Pitch’)
legend(‘Excitation Force nemoh 2.8’,‘Excitation Force nemoh 3.0’,‘Location’,‘southeast’)
xlabel(‘Wave frequency [rad/s]’)
ylabel(‘Force Pitch [N]’)
toc
```

7.2.2. Hydrodynamic results from NEMOH 2.8 and 3.0

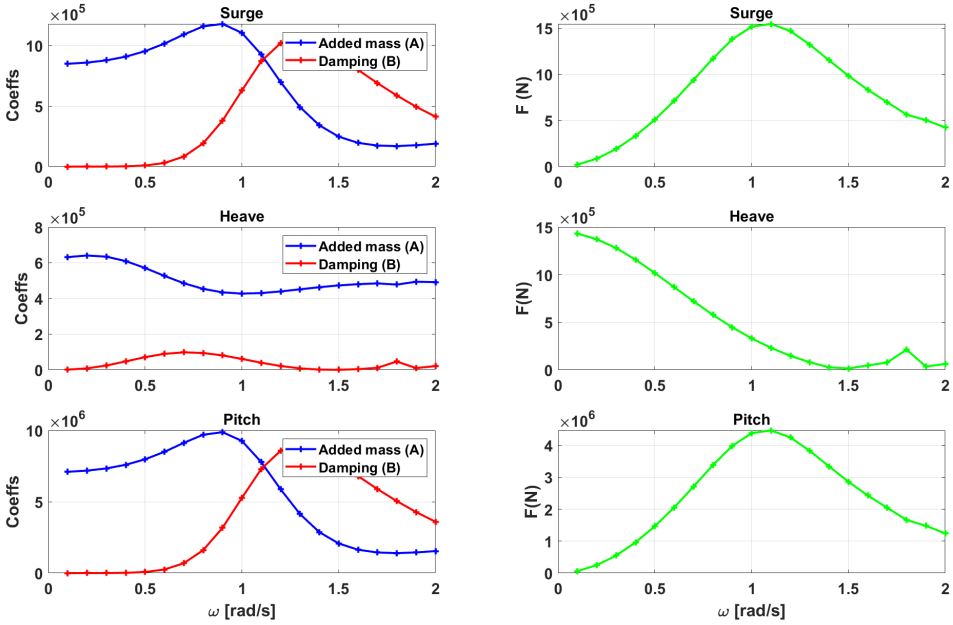

Figure 7.1: Hydrodynamic characteristics computed in NEMOH 3.0

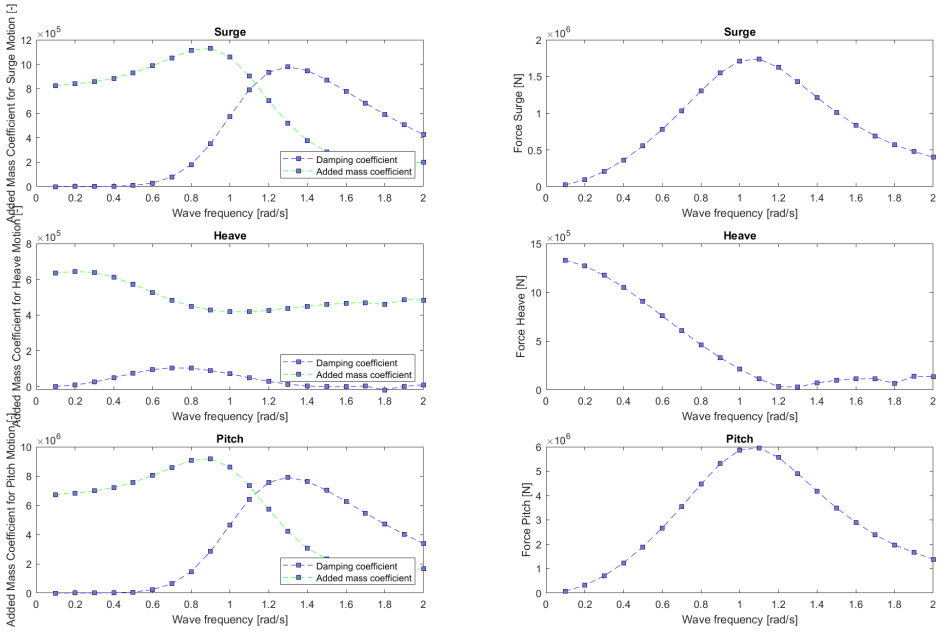

Figure 7.2: Hydrodynamic characteristics computed in NEMOH 3.0

7.2.3. Modification on NEMOH 3.0 code

filename =“...”;
fileID = fopen(filename,‘r’);

% Read the entire file into a character array
fileContents = fileread(filename);
% Replace all occurrences of “diffraction force” with “excitation force”
newContents = strrep(fileContents, ‘Excitation force’, ‘Diffraction force’);
% Close the file
fclose(fileID);
% Open the file for writing
fileID = fopen(filename,‘w’);
% Write the updated contents to the file
fprintf(fileID, ‘%s’, newContents);
% Close the file
fclose(fileID);

7.2.4. wecSimInputFile.m for d = 16 r as an example

%% Simulation Data
simu = simulationClass(); % Initialize Simulation Class
simu.simMechanicsFile = ‘fiveWECssixteen.slx’; % Specify Simulink Model File
simu.mode = ‘normal’; % Specify Simulation Mode(‘normal’,‘accelerator’,‘rapid-accelerator’)
simu.explorer = ‘on’; % Turn SimMechanics Explorer (on/off)
simu.startTime = 0; % Simulation Start Time [s]
simu.rampTime = 900; % Wave Ramp Time [s]
simu.endTime = 900; % Simulation End Time [s]
simu.solver = ‘ode4’; % simu.solver = ‘ode4’ for fixed step & simu.solver =‘ode45’ for variable step
simu.dt = 0.1; % Simulation Time-Step [s]
simu.cicEndTime = 10; % Specify CI Time [s]
waves = waveClass(‘irregular’);
waves.height = [0.5 1 1.5 2 2.5 3]; waves.period = [2 3 4 5 6 7 8]; % Initialize Wave Class and Specify Type
waves.spectrumType = ‘JS’; % Specify Spectrum Type
waves.direction = [0,10,40]; % Wave Directionality [deg]
waves.spread = [0.1,0.2,0.7]; % Wave Directional Spreading [%]
%% Body Data body(1) = bodyClass(‘hydroData/5WECs16R.h5’); % Initialize bodyClass
body(1).geometryFile = ‘geometry/PA1.stl’; % Geometry File
body(1).mass = “equilibrium”; % User-Defined mass [kg]
body(1).inertia = [1294566.5655 1294566.5655 1294566.5655]; % Moment of Inertia [kg-m2]
...
%% PTO and Constraint Parameters % translational constraint(1)= constraintClass(‘Constraint1’);
% Initialize ConstraintClass for Constraint1
constraint(1).location = [0 0 0]; % Constraint Location [m]
...
% translational PTO pto(1) = ptoClass(‘PTO’); % Initialize ptoClass for PTO1
pto(1).stiffness = 0; % PTO Stiffness Coeff [Nm/rad]
pto(1).damping = 8000; % PTO Damping Coeff [Nsm/rad]
pto(1).location = [0 0 0]; % PTO Location [m]

7.2.5. userDefinedFunctionsMCR.m script

%Store Data
mcr.power_average(imcr) = power_abs_average;
mcr.pto_damping(imcr) = pto(1).damping;
% Close previous results
close all
% Scripts for last MCR case

```
if imcr == length(mcr.cases)
%% Load/Store Results
H = mcr.cases(:,1);
T = mcr.cases(:,2);
gamma = 3.3;
c = mcr.pto_damping';
P = abs(mcr.power_average');
all_height = mcr.cases(:, 1);
num_period = sum(all_height == 2);
num_height = (max(all_height)*2);
p_a = mcr.power_average;
new_matrix = reshape(p_a, num_period, num_height)';
new_matrix = flip(new_matrix,2);
figure
mat1 = new_matrix/1000;
mat = mat1;
save('powermatrix.mat','mat1');
%save power matrix data imagesc(mat); % Create a colored plot of the matrix values
colormap parula
textStrings = num2str(mat(:),'%0.2f');
textStrings = strtrim(cellstr(textStrings));
[x, y] = meshgrid(1 : num_period, 1 : num_height);
hStrings = text(x(:),y(:),textStrings(:),...
'HorizontalAlignment','center');
midValue = mean(get(gca,'CLim'));
textColors = repmat(mat(:) < midValue,1,3);
set(hStrings,'Color',num2cell(textColors,2));
c_bar = colorbar;
c_bar.FontSize = 12;
c_bar.Label.String = 'Power (kW)';
set(gca,'XTick',1:num_period,...
'XTickLabel','8','7','6','5','4','3','2',...
'YTick',1:num_height,...
'YTickLabel','0.5','1','1.5','2','2.5','3',...
'TickLength',[0 0]);
xlabel('Tp(s)')
ylabel('Hs(m)')
title(['Power Matrix for Damping = 8000 [N/m/s]'])
fig = gcf;
fig.Units = 'inches';
fig.Position = [1 1 16 10];
file_path = pwd;
file_name = 'PowerMatrix16.png';
saveas(gcf, fullfile(file_path, file_name)); % save figure to current direction
end
```

7.2.6. Power matrices for the WEC array

Configuration 1

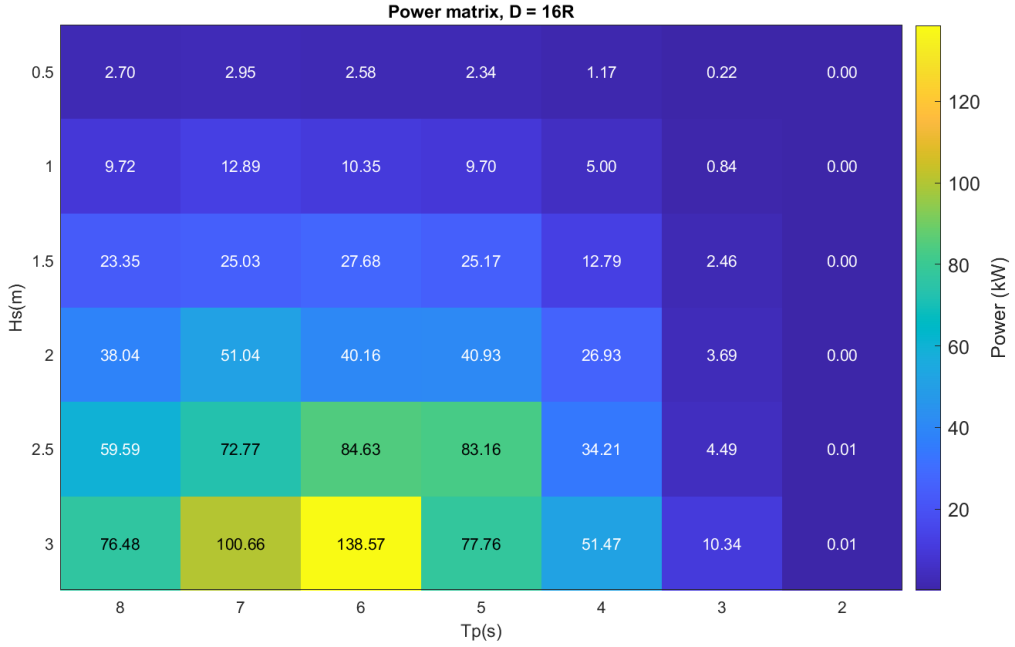

Figure 7.3: Power matrix, 5 WECs, d = 16R, $d_{PTO} = 8KN/-s/m$

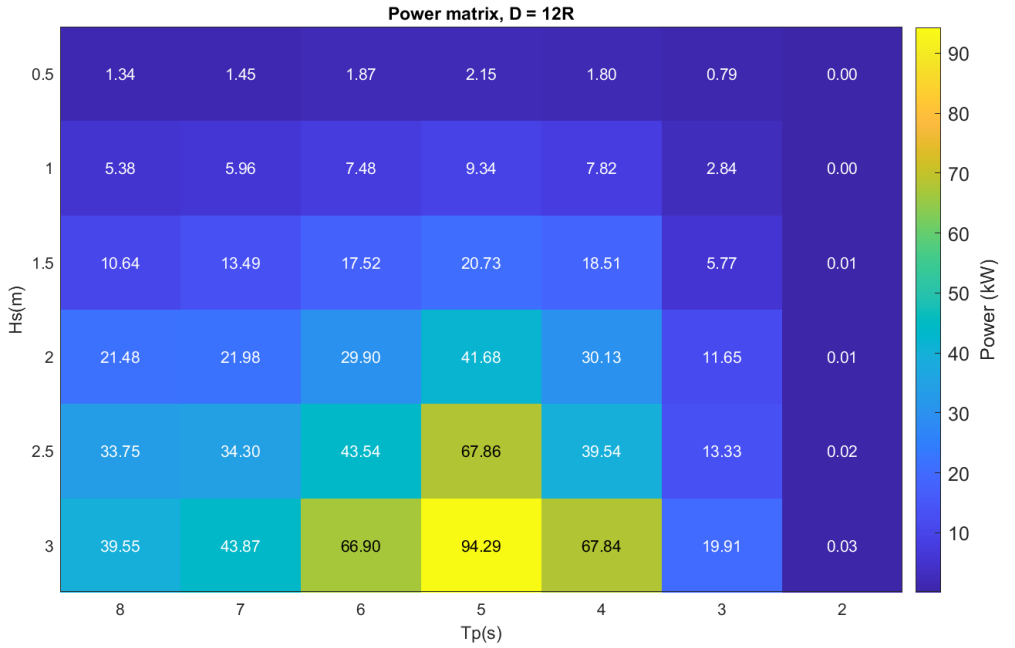

Figure 7.4: Power matrix, 5 WECs, d = 12R, $d_{PTO} = 8KN/-s/m$

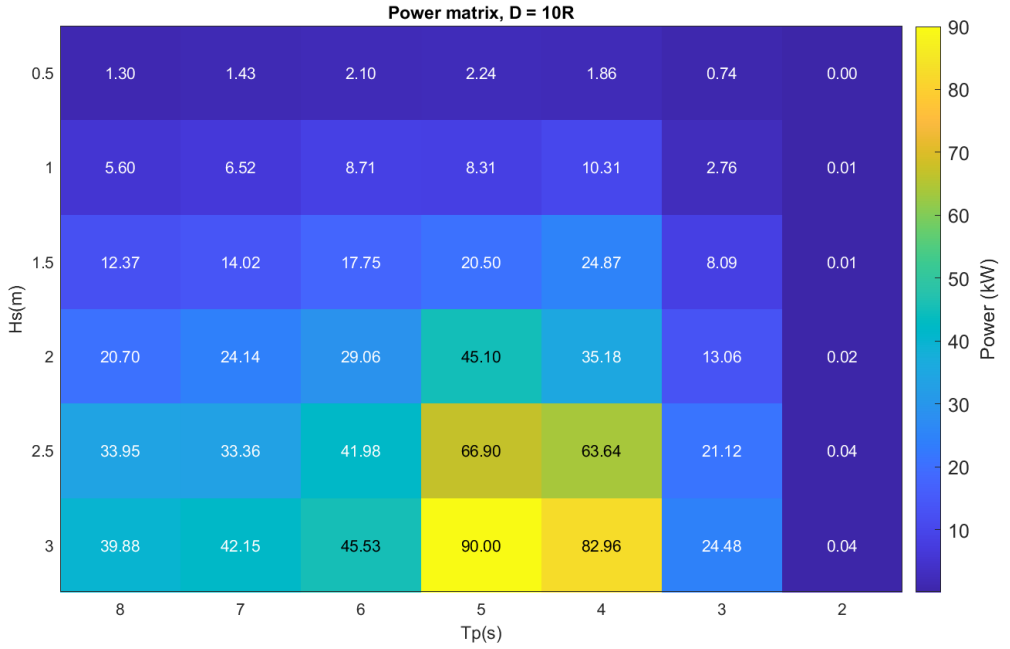

Figure 7.5: Power matrix, 5 WECs, d = 10R, $d_{PTO} = 8KN/-s/m$

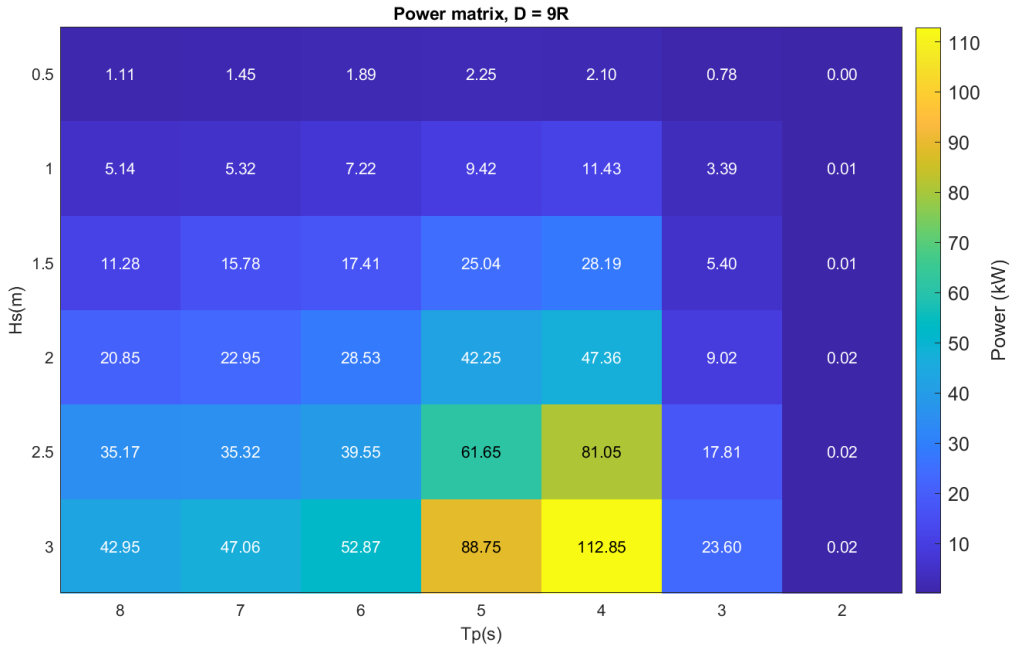

Figure 7.6: Power matrix, 5 WECs, d = 9R, $d_{PTO} = 8KN/-s/m$

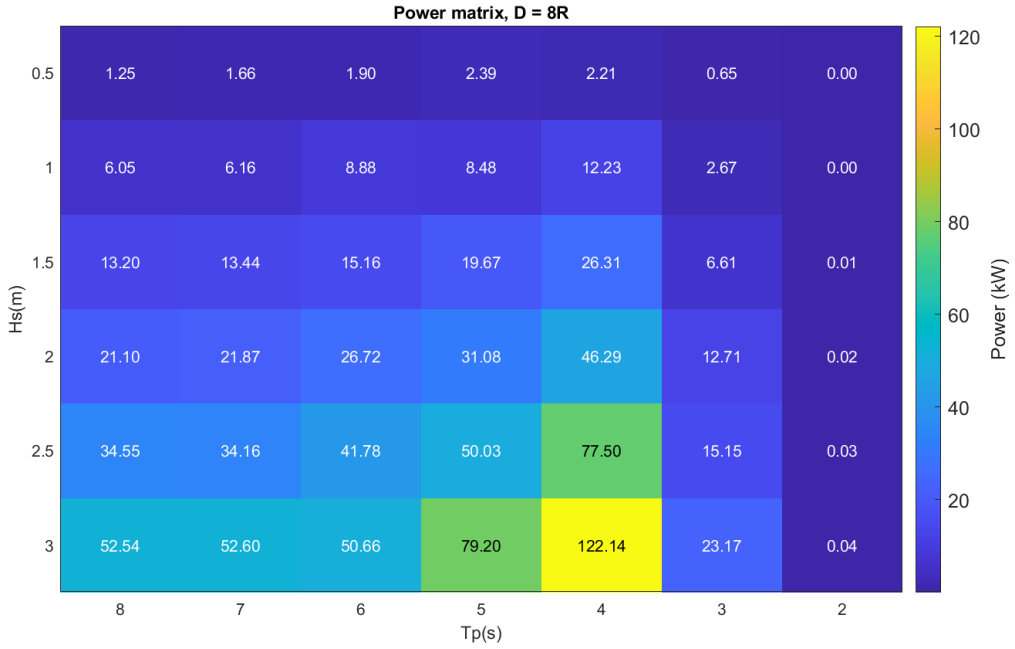

Figure 7.7: Power matrix, 5 WECs, d = 8R, $d_{PTO} = 8KN/-s/m$

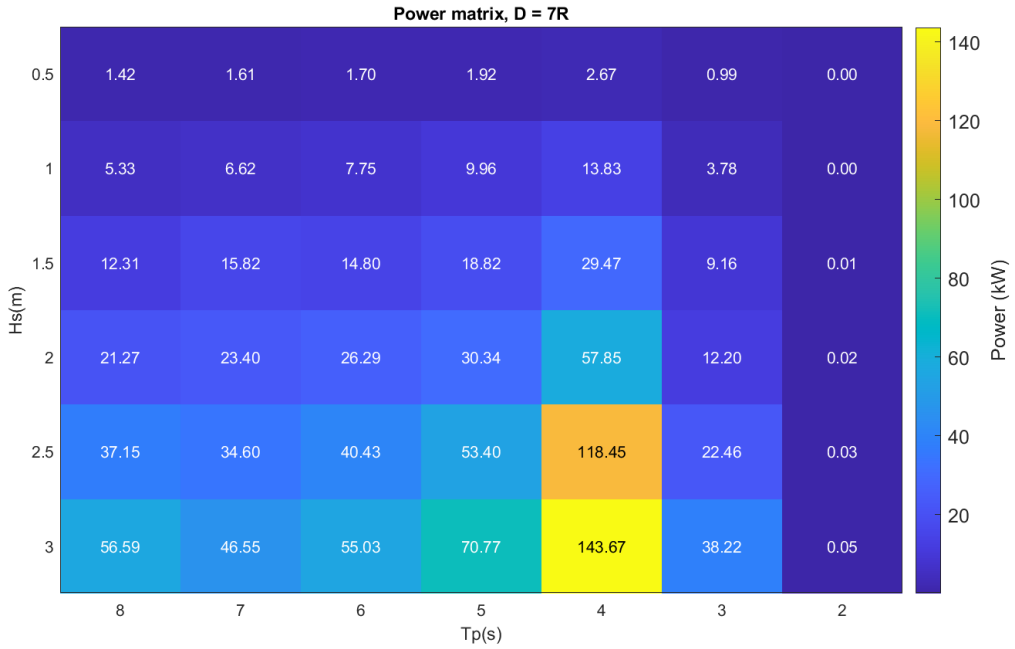

Figure 7.8: Power matrix, 5 WECs, d = 7R, $d_{PTO} = 8KN/-s/m$

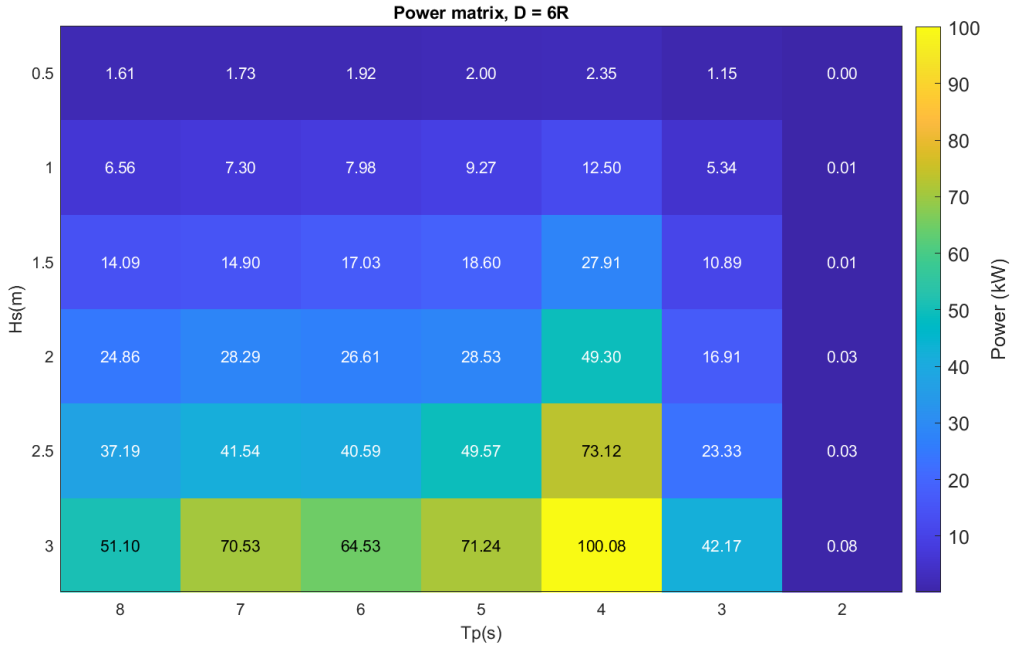

Figure 7.9: Power matrix, 5 WECs, d = 6R, $d_{PTO} = 8KN/-s/m$

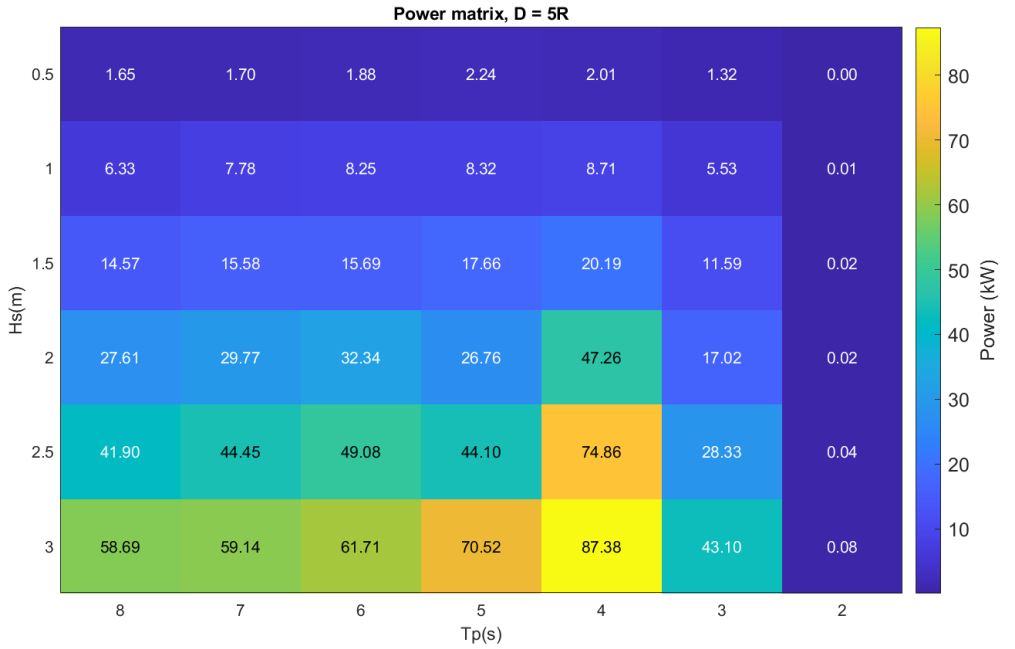

Figure 7.10: Power matrix, 5 WECs, d = 5R, $d_{PTO} = 8KN/-s/m$

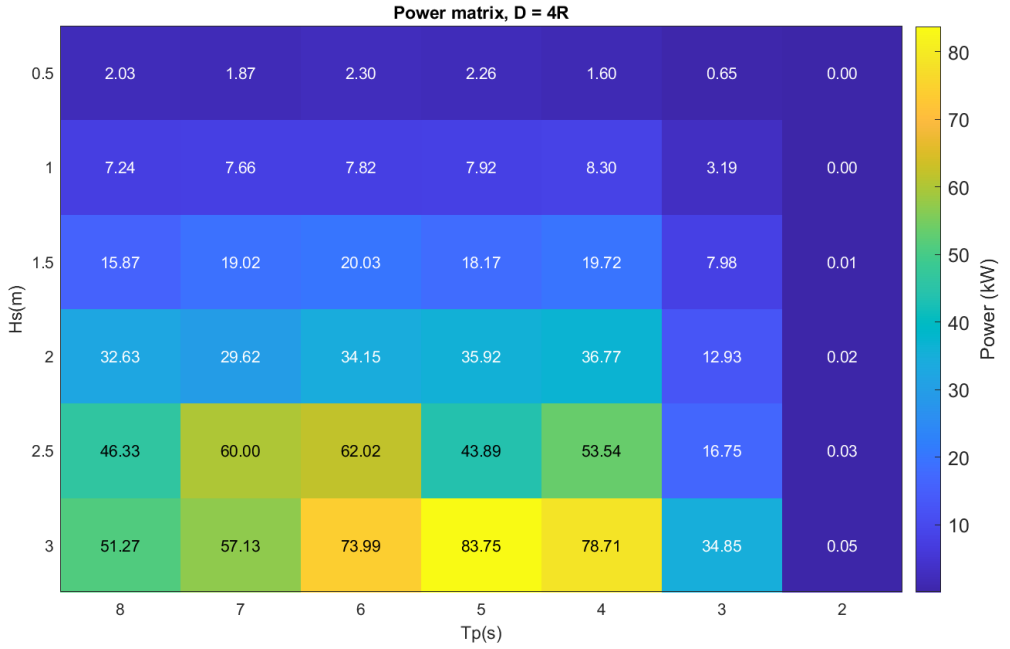

Figure 7.11: Power matrix, 5 WECs, d = 4R, $d_{PTO} = 8KN/-s/m$

Configuration 2

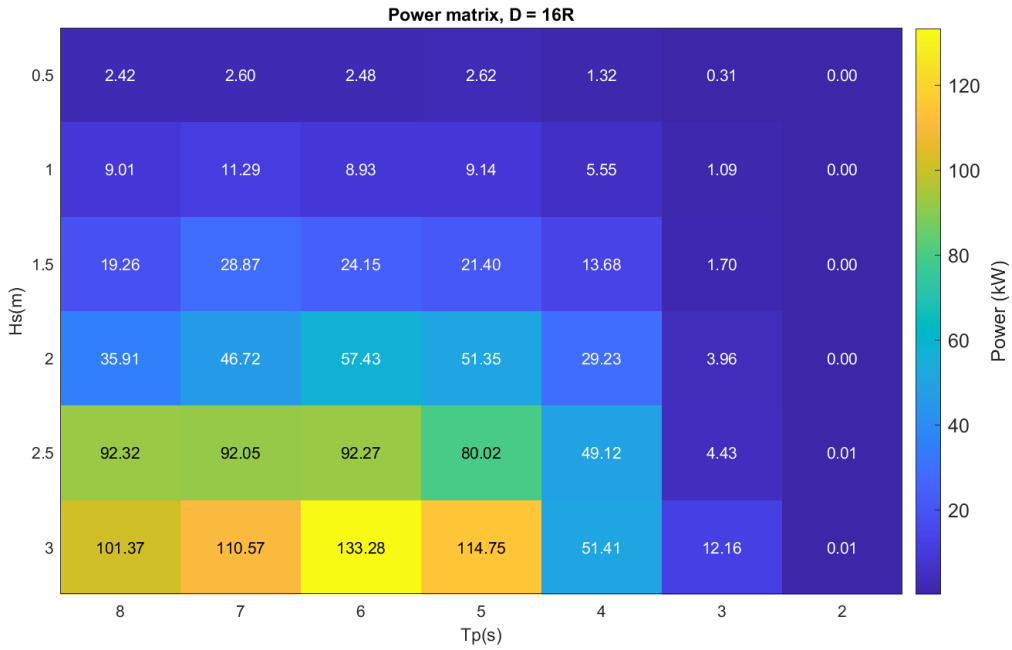

Figure 7.12: Power matrix, 5 WECs, d = 16R, $d_{PTO} = 8KN/-s/m$

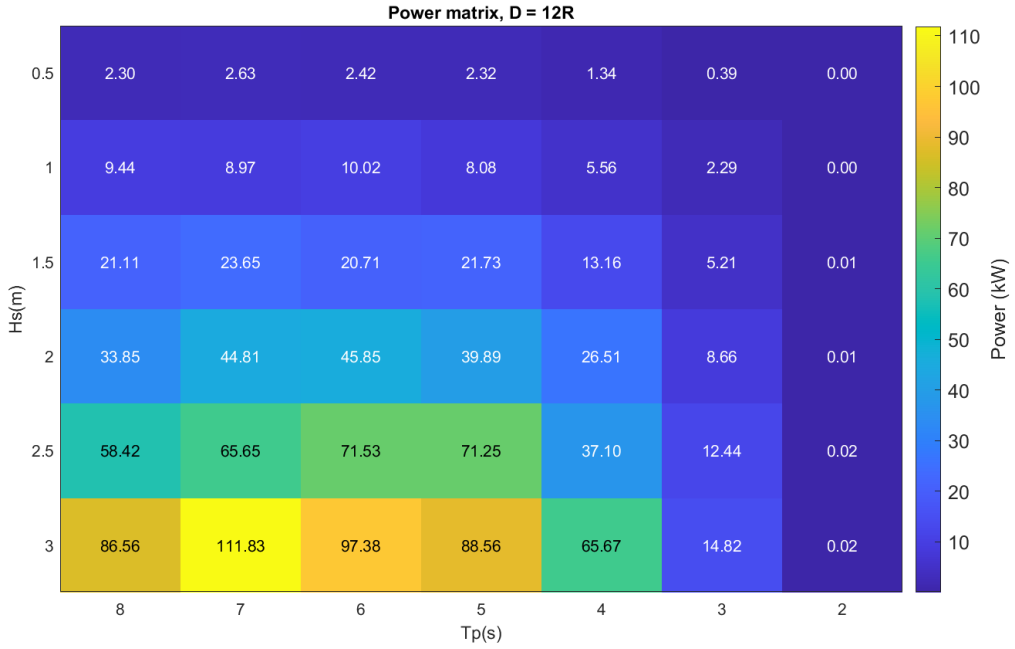

Figure 7.13: Power matrix, 5 WECs, d = 12R, $d_{PTO} = 8KN/-s/m$

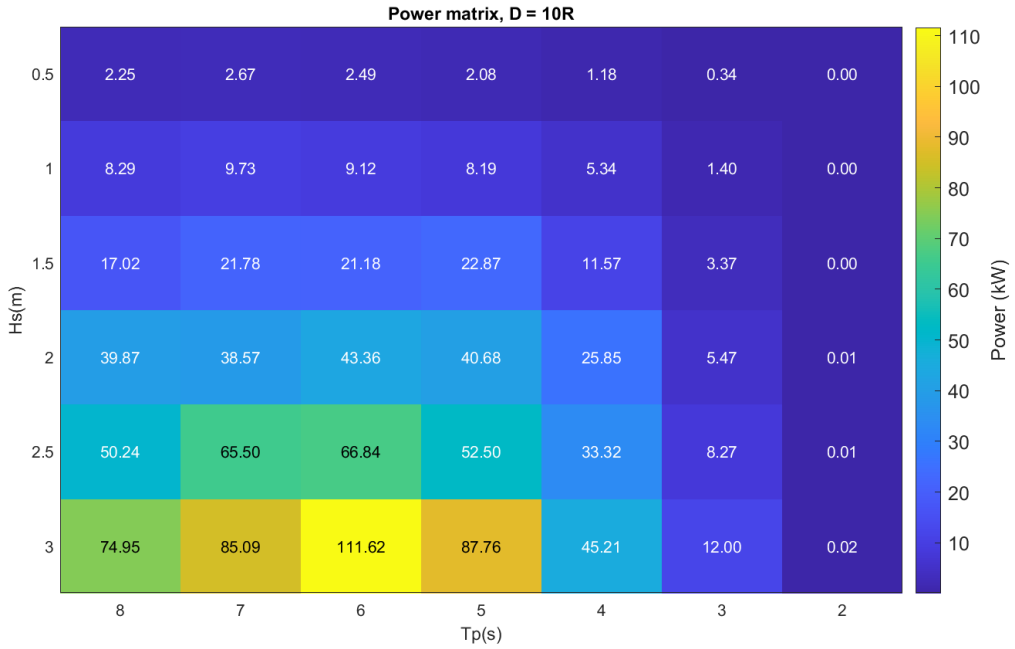

Figure 7.14: Power matrix, 5 WECs, d = 10R, $d_{PTO} = 8KN/-s/m$

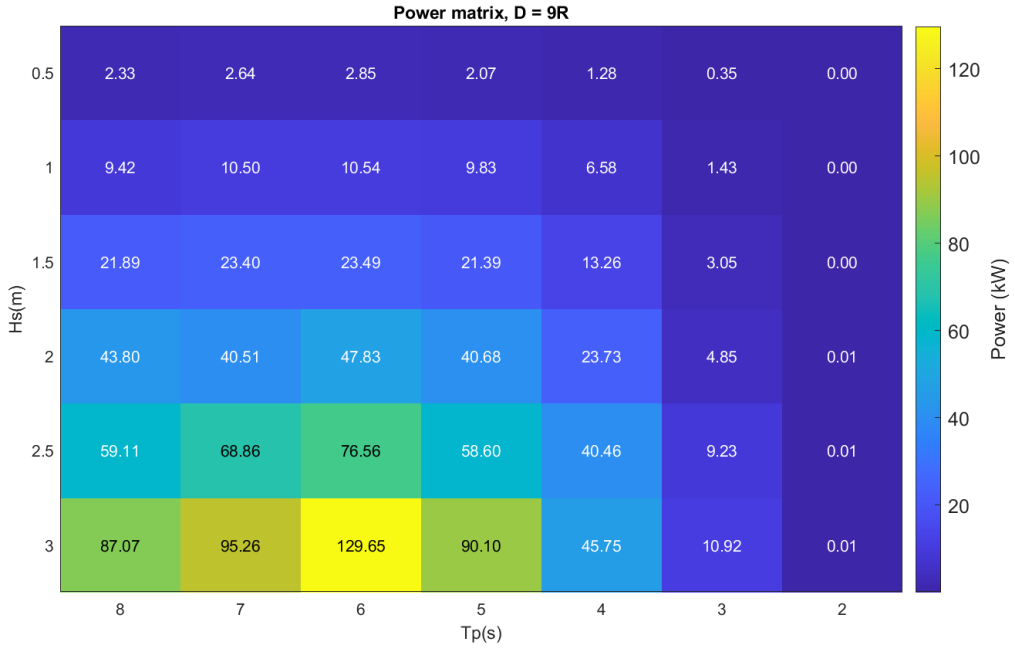

Figure 7.15: Power matrix, 5 WECs, d = 9R, $d_{PTO} = 8KN/-s/m$

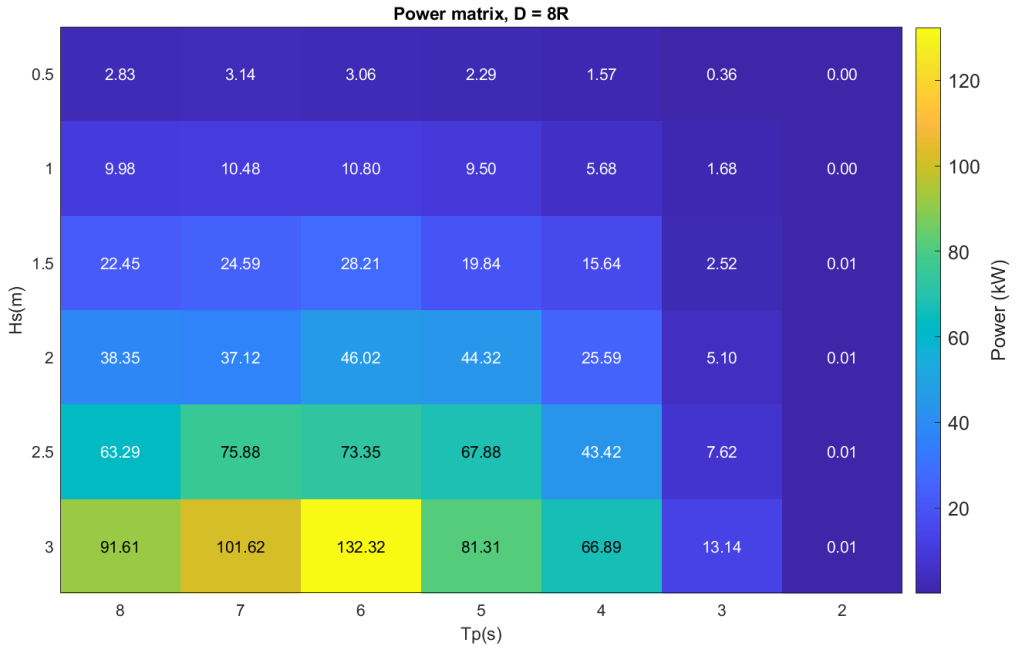

Figure 7.16: Power matrix, 5 WECs, d = 8R, $d_{PTO} = 8KN/-s/m$

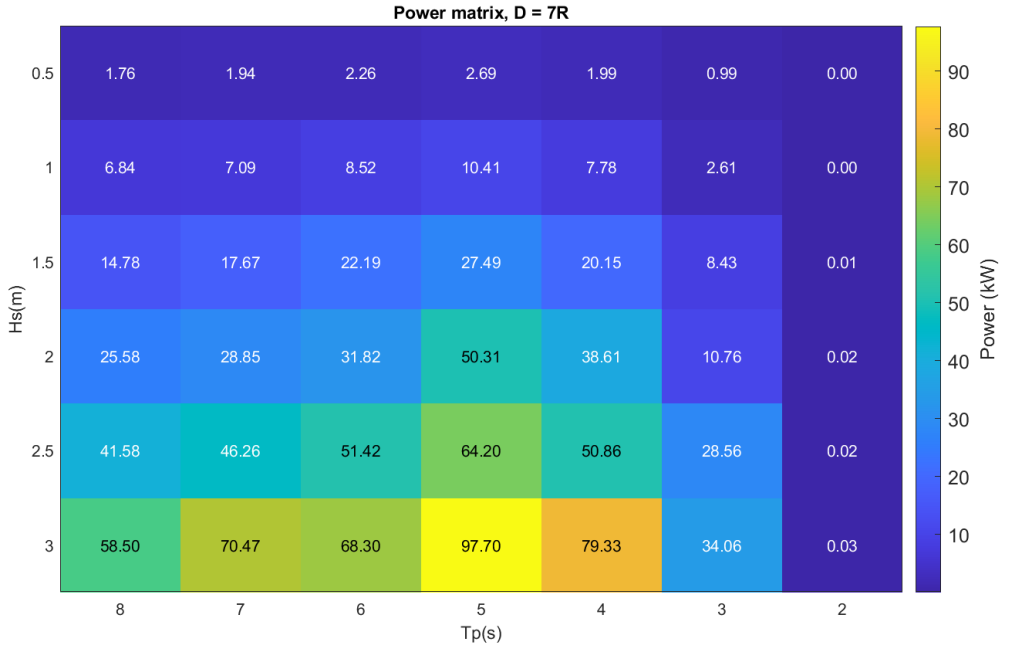

Figure 7.17: Power matrix, 5 WECs, d = 7R, $d_{PTO} = 8KN/-s/m$

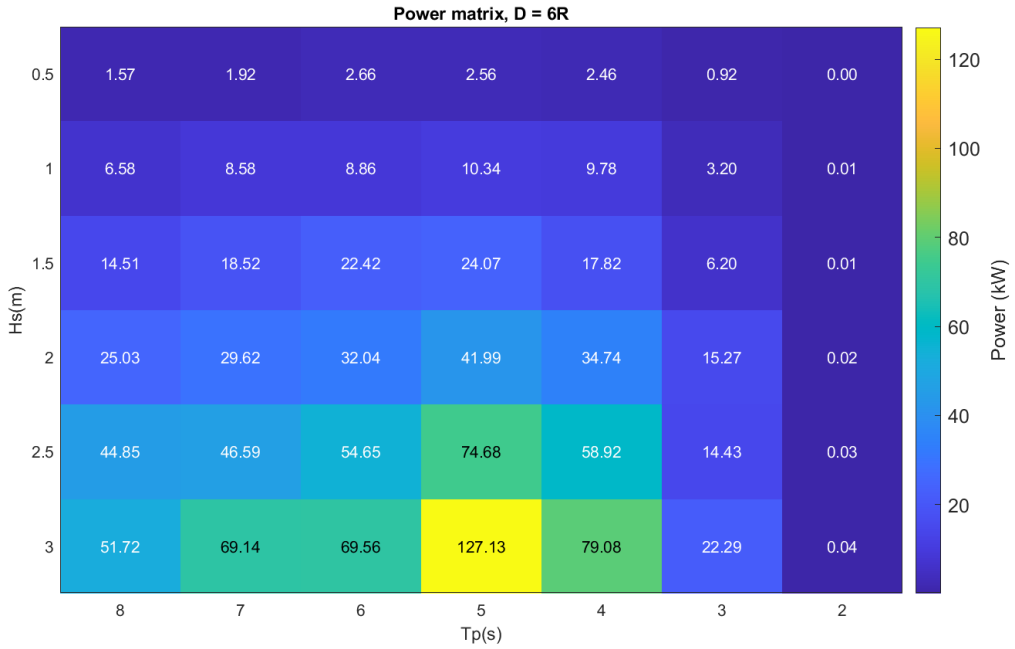

Figure 7.18: Power matrix, 5 WECs, d = 6R, $d_{PTO} = 8KN/-s/m$

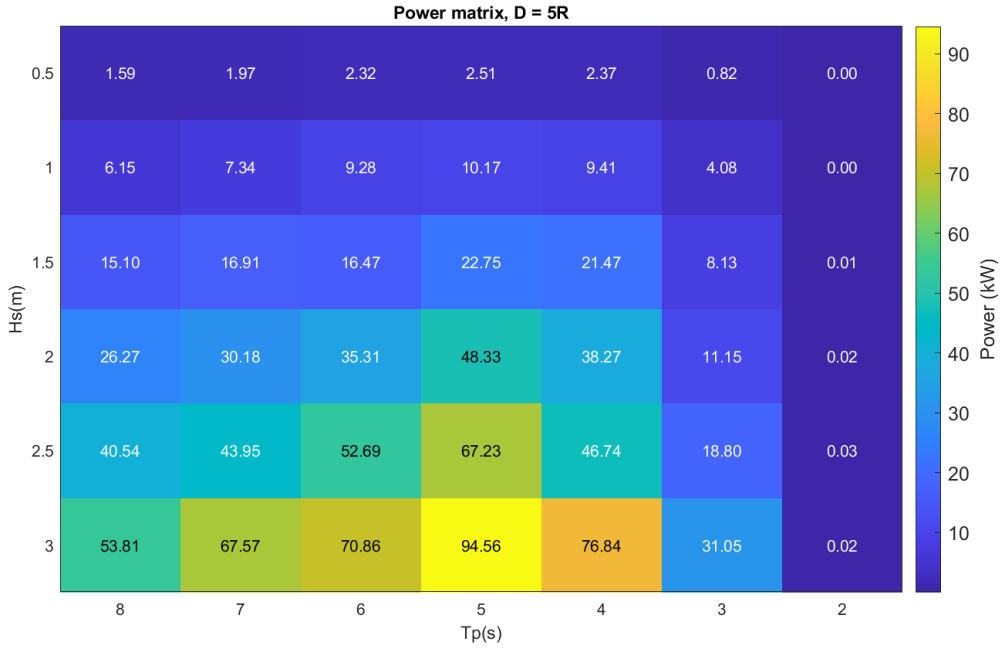

Figure 7.19: Power matrix, 5 WECs, d = 5R, $d_{PTO} = 8KN/-s/m$

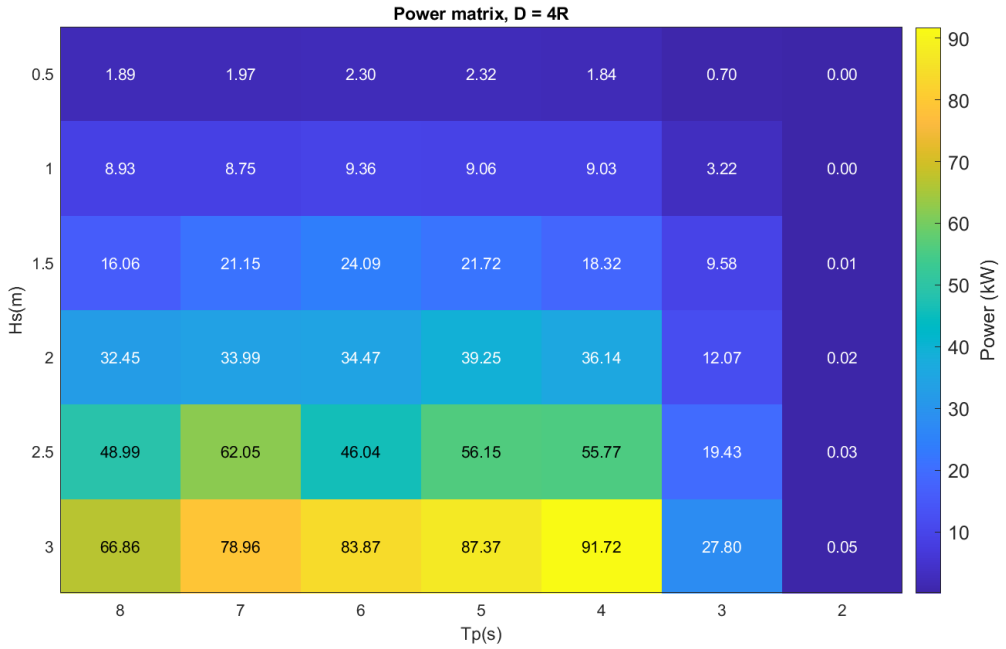

Figure 7.20: Power matrix, 5 WECs, d = 4R, $d_{PTO} = 8KN/-s/m$

7.2.7. Annual power output

Configuration 1

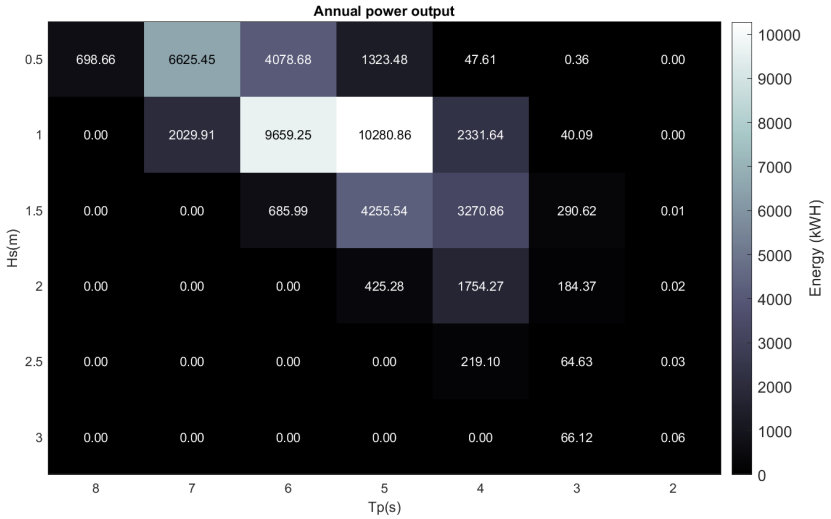

Figure 7.21: Annual power output, d = 16R

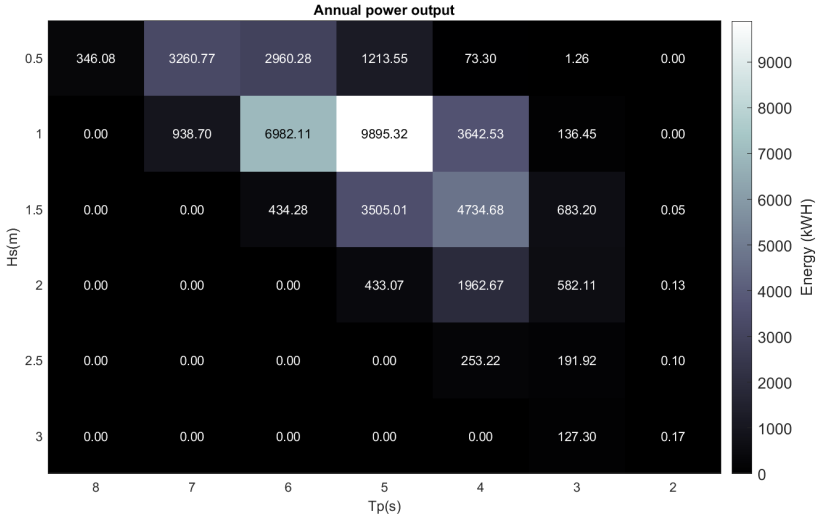

Figure 7.22: Annual power output, d = 12R

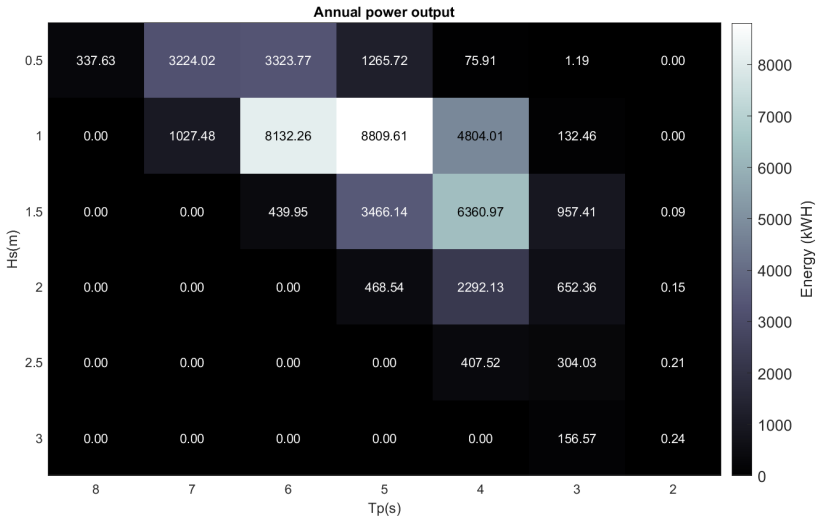

Figure 7.23: Annual power output, d = 10R

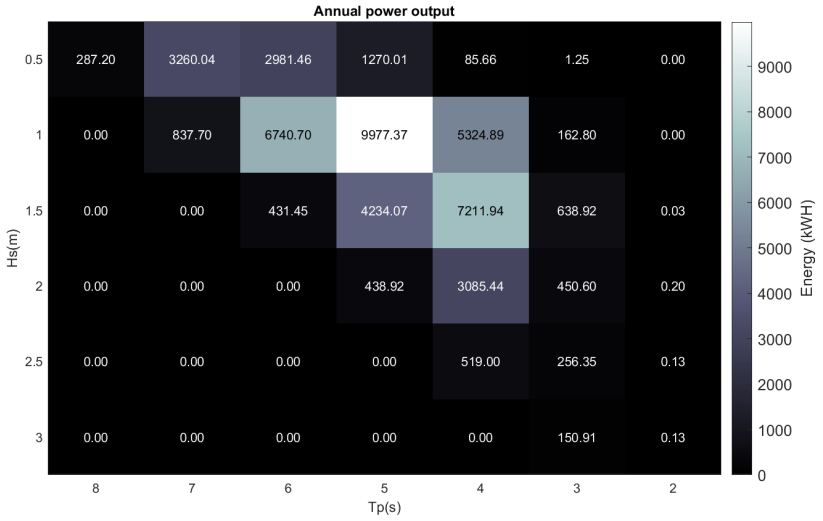

Figure 7.24: Annual power output, d = 9R

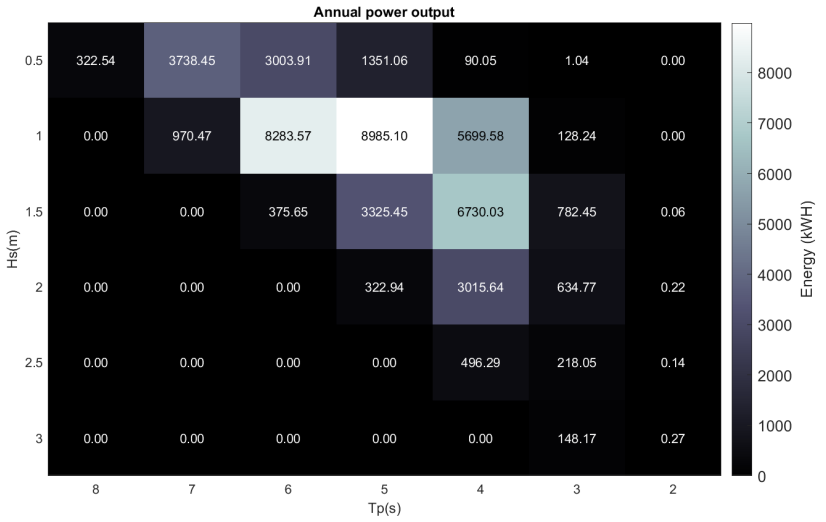

Figure 7.25: Annual power output, d = 8R

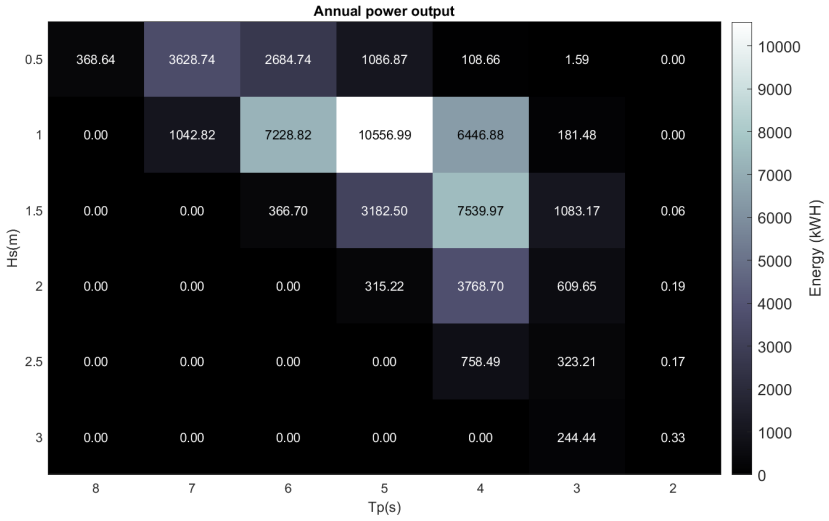

Figure 7.26: Annual power output, d = 7R

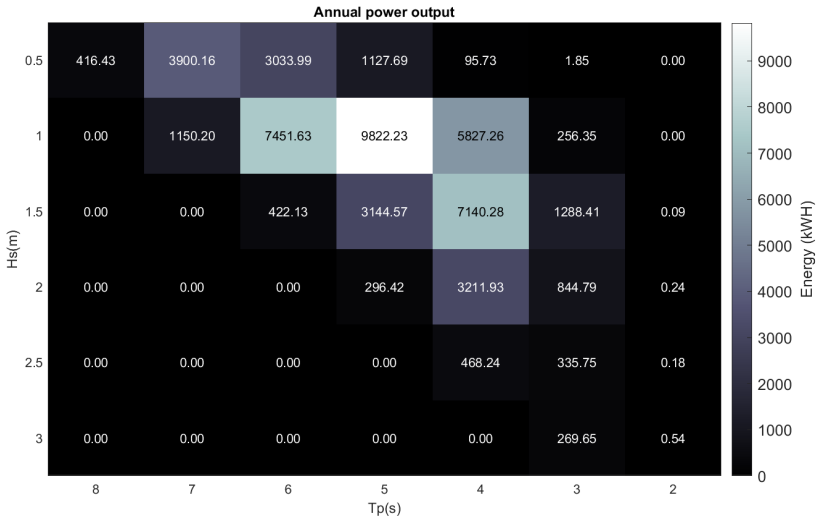

Figure 7.27: Annual power output, d = 6R

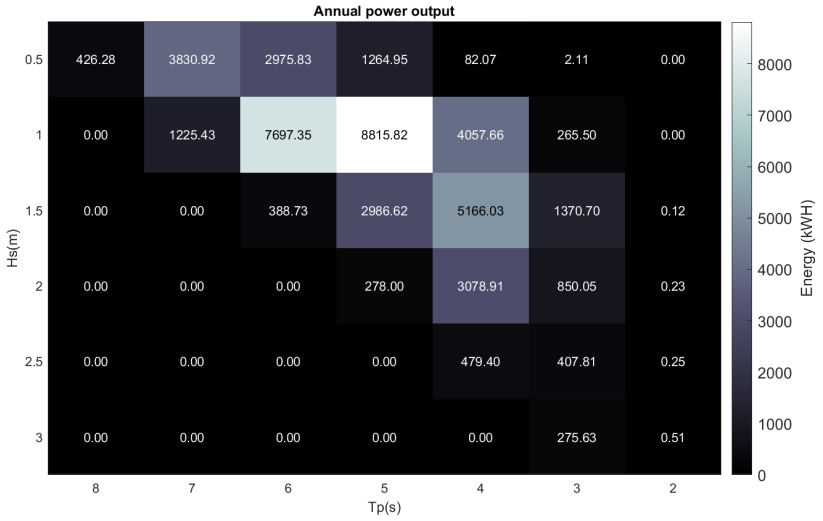

Figure 7.28: Annual power output, d = 5R

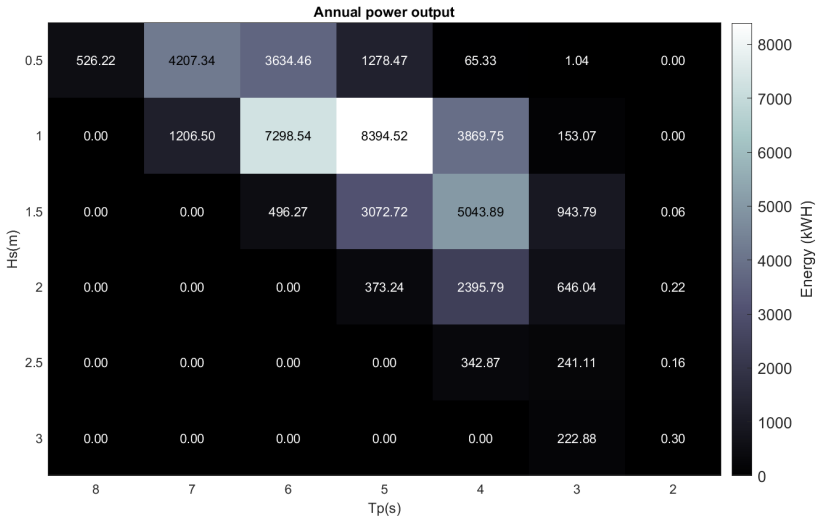

Figure 7.29: Annual power production, d = 4R

Configuration 2

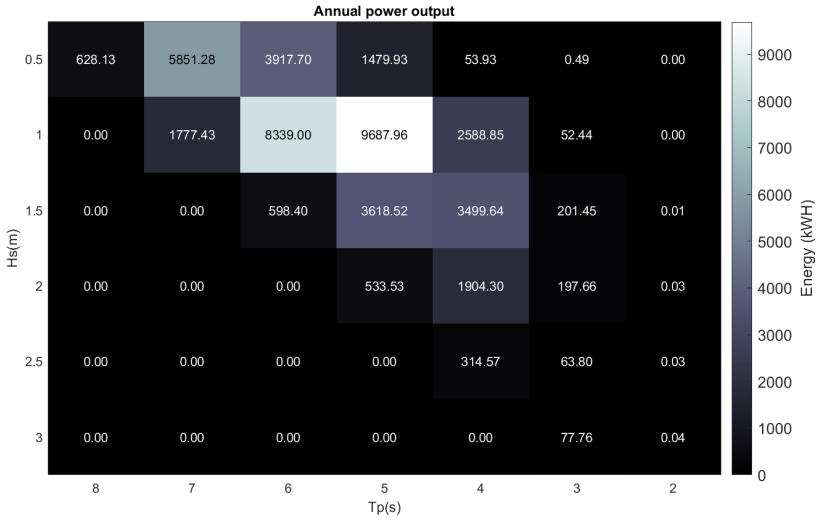

Figure 7.30: Annual power output, d = 16R

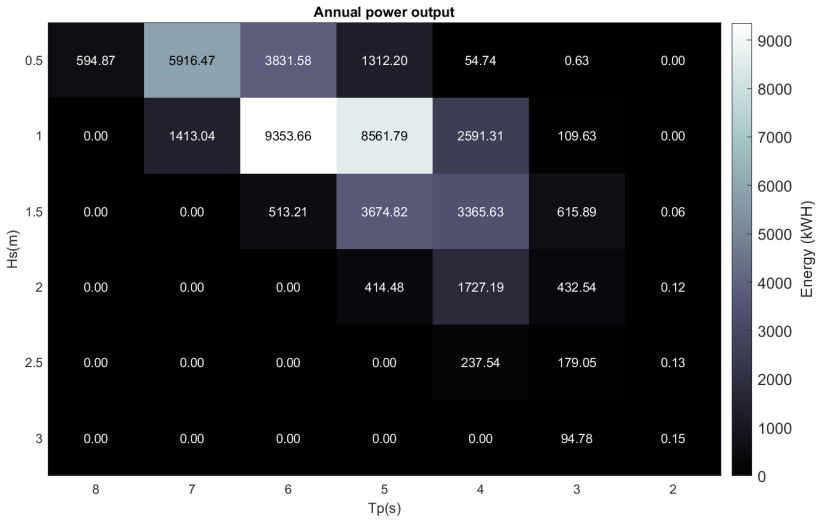

Figure 7.31: Annual power output, d = 12R

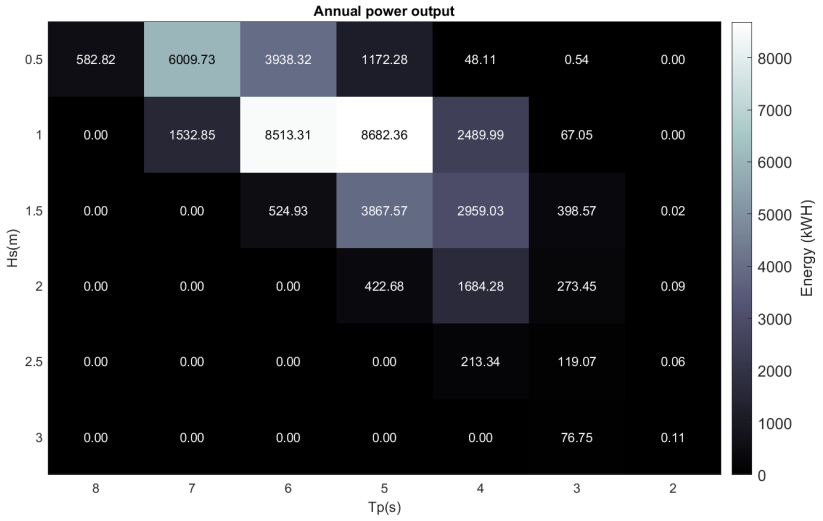

Figure 7.32: Annual power output, d = 10R

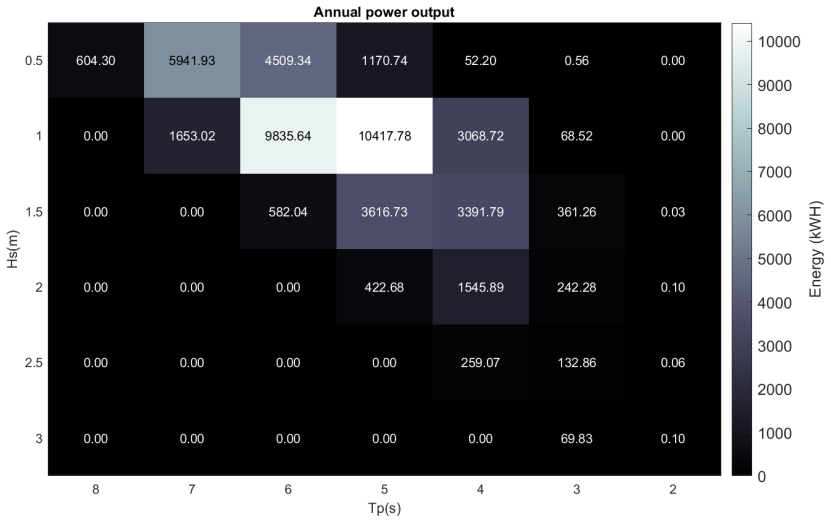

Figure 7.33: Annual power output, d = 9R

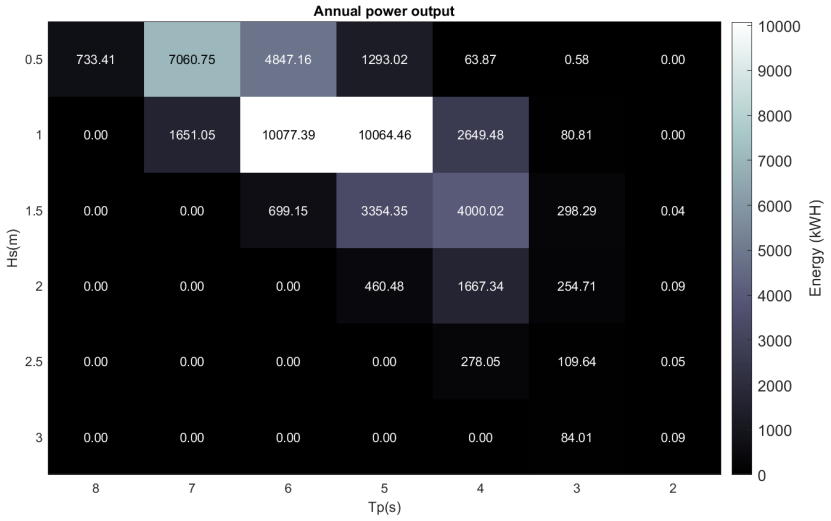

Figure 7.34: Annual power output, d = 8R

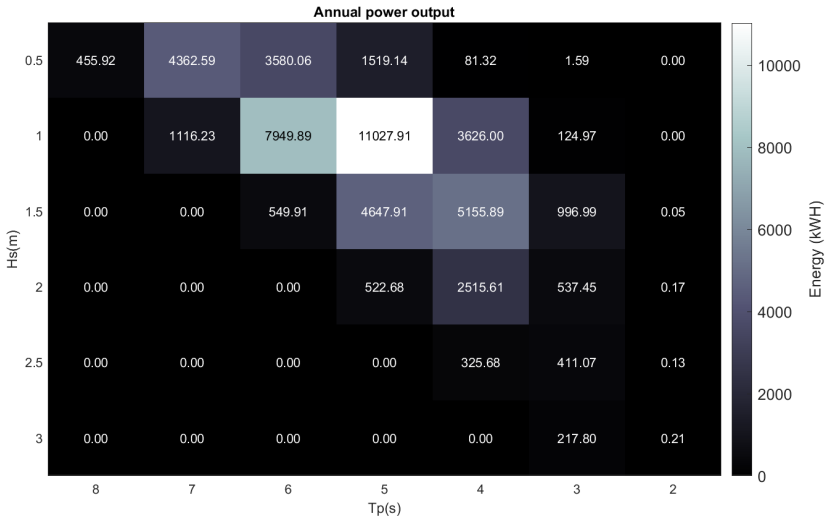

Figure 7.35: Annual power output, d = 7R

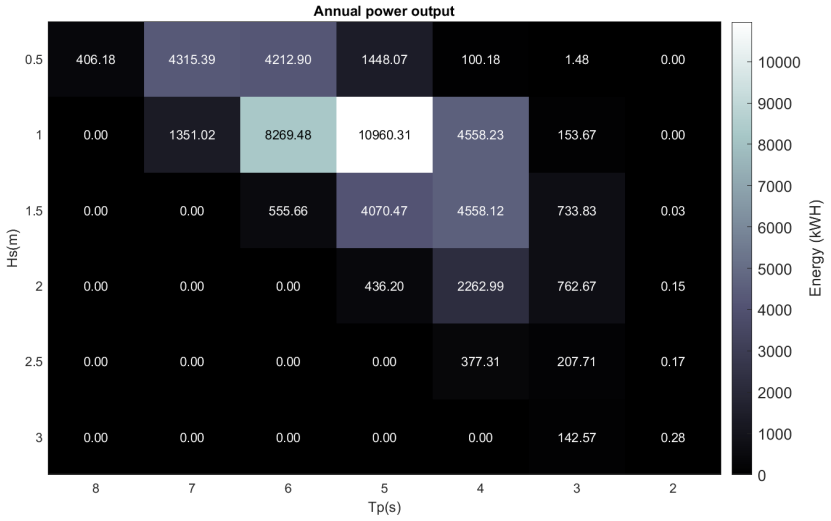

Figure 7.36: Annual power output, d = 6R

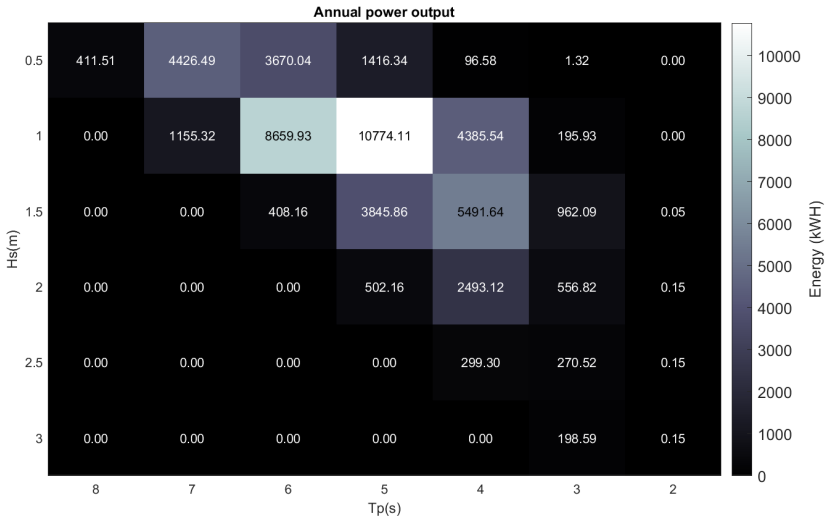

Figure 7.37: Annual power output, d = 5R

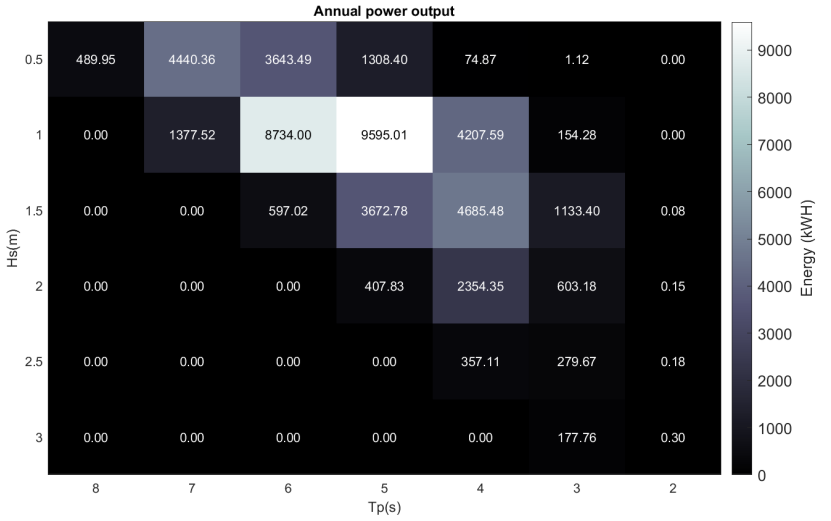

Figure 7.38: Annual power production, d = 4R

Bibliography

[1] Charles D Smith. *Palestine and the Arab-Israeli Conflict. New York: Bedford/St.* 2004.

[2] Peter Scheijgrond. *Worldwide potential energy from water*. Jan. 2022. URL: https://www.bluespring.blue/post/worldwide-potential-energy-from-water.

[3] Greentumble. *Advantages and disadvantages of wave energy*. Feb. 2020. URL: https://greentumble.com/advantages-and-disadvantages-of-wave-power.

[4] Daniel Clemente, P Rosa-Santos, and F Taveira-Pinto. "On the potential synergies and applications of wave energy converters: A review". In: *Renewable and Sustainable Energy Reviews* 135 (2021), p. 110162.

[5] Ioannis Kougias et al. "A methodology for optimization of the complementarity between small-hydropower plants and solar PV systems". In: *Renewable Energy* 87 (2016), pp. 1023–1030.

[6] Alessia Viola et al. "Environmental impact assessment (EIA) of wave energy converter (WEC)". In: *OCEANS 2015-Genova*. IEEE. 2015, pp. 1–4.

[7] Pasquale Filianoti and Sergio M. Camporeale. "A linearized model for estimating the performance of submerged resonant wave energy converters". In: *Renewable Energy* 33.4 (2008), pp. 631–641. ISSN: 0960-1481. DOI: https://doi.org/10.1016/j.renene.2007.03.018. URL: https://www.sciencedirect.com/science/article/pii/S0960148107001012.

[8] Prashant Kumar et al. "Design of a point absorber wave energy converter for an Indian coast". In: *Journal of Physics: Conference Series*. Vol. 2217. 1. IOP Publishing. 2022, p. 012076.

[9] Amir Rahimi et al. "Numerical and experimental study of the hydrodynamic coefficients and power absorption of a two-body point absorber wave energy converter". In: *Renewable Energy* 201 (2022), pp. 181–193.

[10] Kaveh Soleimani and Mohammad Javad Ketabdari. "Performance analysis of a tuned point absorber using SPH calm water and wave tank simulations". In: *Journal of Ocean Engineering and Science* (2022).

[11] Francesco Aristodemo et al. "Solitary wave-induced forces on horizontal circular cylinders: Laboratory experiments and SPH simulations". In: *Coastal Engineering* 129 (2017), pp. 17–35.

[12] Shahab Yeylaghi et al. "Sph modeling of hydrodynamic loads on a point absorber wave energy converter hull". In: *Proceedings of the 11th European Wave and Tidal Energy Conference, Nantes, France*. Vol. 1. 2015.

[13] Kelley Ruehl et al. "Preliminary verification and validation of WEC-Sim, an open-source wave energy converter design tool". In: *International conference on offshore mechanics and arctic engineering*. Vol. 45547. American Society of Mechanical Engineers. 2014, V09BT09A040.

[14] Michael Lawson et al. "Implementing nonlinear buoyancy and excitation forces in the wec-sim wave energy converter modeling tool". In: *International Conference on Offshore Mechanics and Arctic Engineering*. Vol. 45547. American Society of Mechanical Engineers. 2014, V09BT09A043.

[15] Markel Penalba, Thomas Kelly, and John Ringwood. "Using NEMOH for modelling wave energy converters: A comparative study with WAMIT". In: (2017).

[16] Austin S Berrier. "Design Optimization of a Structurally Flexible Wave Energy Converter with a Direct Search Algorithm". In: (2021).

[17] Yingyi Liu. "HAMS: A frequency-domain preprocessor for wave-structure interactions—Theory, development, and application". In: *Journal of Marine Science and Engineering* 7.3 (2019), p. 81.

[18] Wanan Sheng et al. “Hydrodynamic studies of floating structures: Comparison of wave-structure interaction modelling”. In: *Ocean Engineering* 249 (2022), p. 110878.

[19] Phanindra Thummala, ÜMRAN TEZCAN ÜN, and AHMET ÇELİK. “Investigating the Advantages and Limitations of Modeling Physical Mass Transfer of CO2 on Flat Plate by One Fluid Formulation in OpenFOAM”. In: *PERIODICA POLYTECHNICA-CHEMICAL ENGINEERING* 64.1 (2020).

[20] Matthias Steinmetz and Ewald Mueller. “On the capabilities and limits of smoothed particle hydrodynamics”. In: *Astronomy and Astrophysics (ISSN 0004-6361), vol. 268, no. 1, p. 391-410.* 268 (1993), pp. 391–410.

[21] Pál Schmitt et al. “Development and validation of a procedure for numerical vibration analysis of an oscillating wave surge converter”. In: *European Journal of Mechanics-B/Fluids* 58 (2016), pp. 9–19.

[22] Marcio Michiharu Tsukamoto, Kazuo Nishimoto, and Takayuki Asanuma. “Development of particle method representing floating bodies with highly non-linear waves”. In: *18th International Congress of Mechanical Engineering, COBEM.* 2005.

[23] Matthieu Ancellin and Frédéric Dias. “Capytaine: a Python-based linear potential flow solver”. In: *Journal of Open Source Software* 4.36 (2019), p. 1341.

[24] Marianna Giassi, Valeria Castellucci, and Malin Göteman. “Economical layout optimization of wave energy parks clustered in electrical subsystems”. In: *Applied Ocean Research* 101 (2020), p. 102274.

[25] Marianna Giassi and Malin Göteman. “Layout design of wave energy parks by a genetic algorithm”. In: *Ocean Engineering* 154 (2018), pp. 252–261.

[26] Hong-Wei Fang, Yu-Zhu Feng, and Guo-Ping Li. “Optimization of wave energy converter arrays by an improved differential evolution algorithm”. In: *Energies* 11.12 (2018), p. 3522.

[27] Zhenqing Liu, Yize Wang, and Xugang Hua. “Proposal of a novel analytical wake model and array optimization of oscillating wave surge converter using differential evolution algorithm”. In: *Ocean Engineering* 219 (2021), p. 108380.

[28] Junhua Wu et al. “Fast and effective optimisation of arrays of submerged wave energy converters”. In: *Proceedings of the Genetic and Evolutionary Computation Conference 2016.* 2016, pp. 1045–1052.

[29] M Mohsen Moarefdoost, Lawrence V Snyder, and Basel Alnajjab. “Layouts for ocean wave energy farms: Models, properties, and optimization”. In: *Omega* 66 (2017), pp. 185–194.

[30] BFM Child and Vengatesan Venugopal. “Optimal configurations of wave energy device arrays”. In: *Ocean Engineering* 37.16 (2010), pp. 1402–1417.

[31] Dripta Sarkar et al. “Prediction and optimization of wave energy converter arrays using a machine learning approach”. In: *Renewable Energy* 97 (2016), pp. 504–517.

[32] Bo Yang et al. “Wave energy converter array layout optimization: A critical and comprehensive overview”. In: *Renewable and Sustainable Energy Reviews* 167 (2022), p. 112668.

[33] Spyros Foteinis. “Wave energy converters in low energy seas: Current state and opportunities”. In: *Renewable and Sustainable Energy Reviews* 162 (2022), p. 112448.

[34] Rezvan Alamian et al. “Wave energy potential along the southern coast of the Caspian Sea”. In: *International journal of marine energy* 19 (2017), pp. 221–234.

[35] Anna Pavlova et al. “Storm Surges and Extreme Wind Waves in the Caspian Sea in the Present and Future Climate”. In: *Civil Engineering Journal* 8.11 (2022), pp. 2353–2377.

[36] Zaure Bayanovna Rakisheva et al. “Studying the change of average waves of the Caspian Sea using the altimetry data”. In: *Journal of Mathematics, Mechanics and Computer Science* 101.1 (2019), pp. 59–75.

[37] M Majidi Nezhad, D Groppi, and G Piras. "Nearshore wave energy assessment of Iranian coastlines". In: *World Congress on Civil, Structural, and Environmental Engineering*. Vol. 4. 1. 2018, pp. 1–6.

[38] Rezvan Alamian et al. "Evaluation of technologies for harvesting wave energy in Caspian Sea". In: *Renewable and sustainable energy reviews* 32 (2014), pp. 468–476.

[39] George Lavidas. "Energy and socio-economic benefits from the development of wave energy in Greece". In: *Renewable Energy* 132 (2019), pp. 1290–1300. ISSN: 0960-1481. DOI: https://doi.org/10.1016/j.renene.2018.09.007. URL: https://www.sciencedirect.com/science/article/pii/S096014811831070X.

[40] Raphael Stuhlmeier and Dali Xu. "WEC design based on refined mean annual energy production for the Israeli Mediterranean coast". In: *Journal of Waterway, Port, Coastal, and Ocean Engineering* 144.4 (2018), p. 06018002.

[41] JPL McGuinness and G Thomas. "Optimal arrangements of elementary arrays of wave-power devices". In: *Proceedings of the 11th European Wave and Tidal Energy Conference*. 2015.

[42] M Rahman and DD Bhatta. "Evaluation of added mass and damping coefficient of an oscillating circular cylinder". In: *Applied Mathematical Modelling* 17.2 (1993), pp. 70–79.

[43] Robert F Steidel Jr. *An introduction to mechanical vibrations. JohnWiley& Sons*. 1989.

[44] JK Chen et al. "Time domain TEBEM method of ship motion in waves with forward speed by using impulse response function formulation". In: *Ocean Engineering* 227 (2021), p. 108617.

[45] Klaus Hasselmann et al. "Measurements of wind-wave growth and swell decay during the Joint North Sea Wave Project (JONSWAP)." In: *Ergaenzungsheft zur Deutschen Hydrographischen Zeitschrift, Reihe A* (1973).

[46] Arthur Pecher and Jens Peter Kofoed. *Handbook of ocean wave energy*. Springer Nature, 2017.

[47] Johannes Falnes and Adi Kurniawan. *Ocean waves and oscillating systems: linear interactions including wave-energy extraction*. Vol. 8. Cambridge university press, 2020.

[48] Aurélien Babarit et al. "Numerical benchmarking study of a selection of wave energy converters". In: *Renewable energy* 41 (2012), pp. 44–63.

[49] Apr. 2023. URL: https://www.aesc.nl/cad/spaceclaim/?gad=1&gclid=Cj0KCQjwnf-kBhCnARIsAFlg491F78_nmyUbYJM6QUdbEH24QpiDeeQjH4I7HZMAYbR0RDXjBrFGyNsaAiLiEALw_wcB.

[50] BEMRosetta. *Bemrosetta/Bemrosetta: Hydrodynamic coefficients viewer and converter for Boundary Element Method Solver formats*. URL: https://github.com/BEMRosetta/BEMRosetta.

[51] Kelley Ruehl et al. *WEC-Sim/WEC-Sim: WEC-Sim v5.0.1*. 2022. DOI: 10.5281/ZENODO.7121186. URL: https://zenodo.org/record/7121186.

[52] Weixing Chen et al. "Design of the wave energy converter array to achieve constructive effects". In: *Ocean Engineering* 124 (2016), pp. 13–20.

[53] Delft High Performance Computing Centre (DHPC). *DelftBlue Supercomputer (Phase 1)*. https://www.tudelft.nl/dhpc/ark:/44463/DelftBluePhase1. 2022.

[54] Maria Angeliki Chatzigiannakou et al. "Offshore deployments of wave energy converters by Uppsala University, Sweden". In: *Marine Systems & Ocean Technology* 14 (2019), pp. 67–74.

[55] Adrián D de Andrés, Henry Jeffrey, and Raúl Guanche. "Finding locations for wave energy development as a function of reliability metrics". In: *11th European Wave and Tidal Energy Conference (EWTEC), Nantes, France*. Vol. 2015. 2015.

[56] URL: https://climate.ec.europa.eu/system/files/2020-05/20200605_annex_b_en.pdf.

[57] Kalyanmoy Deb et al. "A fast and elitist multiobjective genetic algorithm: NSGA-II". In: *IEEE transactions on evolutionary computation* 6.2 (2002), pp. 182–197.

[58] Viviane De Buck et al. “Multi-objective optimisation of chemical processes via improved genetic algorithms: A novel trade-off and termination criterion”. In: *Computer Aided Chemical Engineering*. Vol. 46. Elsevier, 2019, pp. 613–618.

[59] Caitong Yue et al. “Differential evolution using improved crowding distance for multimodal multiobjective optimization”. In: *Swarm and Evolutionary Computation* 62 (2021), p. 100849.

[60] Aravind Seshadri. *NSGA - II: A multi-objective optimization algorithm (MATLAB Central File Exchange)*. Tech. rep. Jan. 2009. URL: `https://www.mathworks.com/matlabcentral/fileexchange/10429-nsga-ii-a-multi-objective-optimization-algorithm`.

8

Acknowledgements

I would like to express my sincere appreciation to Professor George Lavidas for his exceptional patience and invaluable guidance throughout this research. I consider myself fortunate to have been entrusted with this insightful topic proposed by him. I have learned a lot when working with him, as he generously shared his knowledge and expertise, allowing me to grasp the significance and value of this topic and find it even more interesting.

I am also deeply grateful to my daily supervisor, Vaibhav Raghavan, for his immense support while I encountered challenges in first using hydrodynamic software, as well as facing difficulties during the whole research process. His willingness to share his experience helped me a lot in troubleshooting and learning new skills.

Lastly, I cannot overlook the support and encouragement I received from my father, my girlfriend, my friends, Lefteris, Penny, Mona, and Xusheng and all the other friends I made in the Netherlands. They have been keeping me good company, which is really helpful to keep my motivation high.

All their contributions and support have played a valuable role in the completion of my thesis journey, therefore, I am sincerely grateful.